

Slip Fronts at Frictional Interfaces: A Numerical and Theoretical Study

THÈSE N° 6492 (2014)

PRÉSENTÉE LE 12 DÉCEMBRE 2014

À LA FACULTÉ DE L'ENVIRONNEMENT NATUREL, ARCHITECTURAL ET CONSTRUIT
LABORATOIRE DE SIMULATION EN MÉCANIQUE DES SOLIDES
PROGRAMME DOCTORAL EN MÉCANIQUE

ÉCOLE POLYTECHNIQUE FÉDÉRALE DE LAUSANNE

POUR L'OBTENTION DU GRADE DE DOCTEUR ÈS SCIENCES

PAR

David Simon KAMMER

acceptée sur proposition du jury:

Prof. F. Gallaire, président du jury
Prof. J.-F. Molinari, directeur de thèse
Prof. W. Curtin, rapporteur
Prof. J. Fineberg, rapporteur
Dr J. Scheibert, rapporteur



ÉCOLE POLYTECHNIQUE
FÉDÉRALE DE LAUSANNE

Suisse
2014

To Angy & Lily

Acknowledgements

This thesis is the result of four years of research conducted within the Computational Solid Mechanics Laboratory (LSMS) at Ecole Polytechnique Fédérale de Lausanne (EPFL). During this time, I had the pleasure of working with very talented and motivated people who have inspired me on many occasions. I would like to thank all of them for their support and the enjoyable moments we spent together.

First and foremost, I would like to express my deepest gratitude to my advisor Professor Jean-François Molinari. He has not only given me the opportunity of pursuing a PhD on a very interesting subject, but also the freedom to follow my instinct and applying my own style to explore my research topic. He has always been an encouraging advisor who knew how and when to challenge me and my ideas in order to get the best out of my research. I was more than fortunate to have an advisor who understood my strengths and compensated my weaknesses. I am particularly grateful to the members of my thesis committee, Professor François Gallaire, Professor William Curtin, Professor Jay Fineberg, and Doctor Julien Scheibert, for their time and the interesting discussion on various aspects of my work.

The research conducted for this thesis was financed by the European Research Council through the project ERCstg UFO-240332. I am very thankful for this support and the opportunities it provided me.

I would like to thank my colleagues with whom I have collaborated closely at the LSMS. Doctor Peter Spijker introduced me to the world of research when he was my master thesis advisor. He supported me with precious advice on technical as well as writing-related issues. I was very fortunate that early on during my PhD, Doctor Vladislav Yastrebov joined the LSMS. With his enthusiasm and deep knowledge of mechanics, he has been an inspiration to me during all these years. At a crucial point, I benefited from Doctor Guillaume Ancaux's insights on numerical techniques, which provided the basis for much of my research. I was also very fortunate to work with Doctor Mathilde Radiguet, who impressed me regularly with her masterful approach to research. She made "doing research" look so easy to me. I could not have had a better collaborator for the second part of my PhD. I also benefited from collaborating with Fabian Barras on a problem of fracture involving friction, which widened my knowledge on the propagation of discontinuities. During the last months of my PhD I was fortunate to work with Doctor Daniel Pino Muñoz. His open-minded approach is a model for me and has been very helpful on the finishing straight of my work. I have enjoyed all of these collaborations very much, not only from a research point of view but also on a personal level. Peter, Vlad, Guillaume, Mathilde, Fabian and Daniel have all become good friends to me.

Acknowledgements

My research also gave me the opportunity of collaborating with exceptional experts of the fields of computational mechanics and interface dynamics. Professor Philippe Geubelle from the University of Illinois at Urbana-Champaign, who I met during his sabbatical year at EPFL, was a particularly valuable source of knowledge for me. Our collaboration through the master project of Fabian Barras taught me a lot about the spectral boundary integral method and the dynamics of weak interfaces. I was also very fortunate to collaborate with Professor Pablo Ampuero from the California Institute of Technology. He was the basis for me to see frictional sliding through the eyes of fracture mechanics theory and I am always impressed by his deep knowledge of frictional interfaces. I am grateful to both for their hospitality during my visits as well as their contributions to my research.

I would like to thank Doctor Nicolas Richart for all the support I received regarding coding practice and the efficient usage of Linux computers. In moments of desperation, he helped at impossible hours and sometimes from far away to get me back on track. On uncountable occasions, I have benefited from advice of my long-standing office mate, Doctor Till Junge, to whom I am especially thankful. He was not only a great source of outside opinions for my work, but also a friend with whom I shared highly appreciated chats about life and the world outside. It would have been so much tougher without the help and friendship of Nicolas and Till.

I am grateful to Birgitte Seem, the administrative assistant at the LSMS, who has been helpful on so many occasions. Organizing trips to conferences and visits overseas has always been so easy. I also would like to thank all the current and past members of the LSMS. Being part of this multicultural and multilingual team was great fun and very enriching. I very much enjoyed our coffee breaks, lunches, lab dinners, and lab outings.

A special thank you to Ulugbek Kamilov and Raphaël Thiébaud for their friendship during all these years. I have been very lucky having you both pursuing a PhD at EPFL during the same time as myself. Your friendship and support have been a source of motivation and inspiration for me, for which I am particularly grateful. I look up to you as friends and models.

Ein herzliches Dankschön an meine Eltern, Nicole und Martin. Eure Unterstützung ist und war schon immer unerschöpflich. Ihr steht mir seit Langem mit Rat und Tat zur Seite und habt mir damit den weiten Weg bis hierhin geebnet. Ich bin auch meiner Schwester, Nina, sehr dankbar. Du bist von jeher mein Freund und immer zur Stelle wenn nötig.

La personne pour laquelle je me sens le plus reconnaissant est mon épouse, Angélique. Tu as été un support incroyable pendant toutes ces années. Tu as accepté et respecté mon absence physique et psychique, et tu t'es occupée de tout pour me permettre de me consacrer entièrement à ma thèse. Sans toi, je n'y serais pas arrivé. Mais plus important que tout, tu m'as fait le plus beau cadeau possible: notre fille, Liliane, qui ensoleille notre vie depuis son premier jour avec une force incroyable. Urakoze cyane!

Lausanne, November 13, 2014

David Kammer

Résumé

Bien que le frottement affecte notre quotidien de multiples façons, ce phénomène constitue toujours un des grands mystères de la physique. Le frottement est véritablement un phénomène multi-échelle combinant une grande variété de processus actifs à différentes échelles de longueur et de temps. Récemment, la recherche des origines du frottement a accordé une attention importante aux propriétés micro et nanoscopiques de l'interface au détriment des aspects structuraux du frottement agissant aux échelles méso et macroscopiques. Cette thèse ambitionne de démontrer que ces aspects sont cependant essentiels dans la description du comportement macroscopique des interfaces de frottement, et poursuit ainsi l'objectif d'améliorer la connaissance actuelle de la propagation des fronts de glissement le long de ces interfaces.

La mécanique des interfaces de frottement est étudiée à l'aide de simulations éléments finis dynamiques en modélisant des systèmes reproduisant les conditions expérimentales. En fonction de la nature du phénomène étudié, les simulations sont effectuées en deux ou trois dimensions. De plus, des modèles théoriques basés sur la mécanique de la rupture sont développés et appliqués pour confirmer les observations numériques. Ces modèles permettent de mieux comprendre les mécanismes gouvernant la propagation des fronts de glissement et révèlent l'influence des différents paramètres du système, du matériau, et de l'interface.

Les résultats présentés dans cette thèse montrent que les modèles numériques appliqués reproduisent quantitativement les observations expérimentales reportées dans la littérature. Les aspects étudiés du glissement d'interface de frottement comprennent, entre autres, la vitesse de propagation, la position d'arrêt, et l'effet des hétérogénéités à l'interface. Au-delà de confirmer les observations expérimentales, les modèles numériques et théoriques révèlent de nouvelles propriétés de la propagation et de l'arrêt des fronts de glissement. Ils montrent, par exemple, que la vitesse du front de glissement dépend de la direction de propagation et que la position d'arrêt des précurseurs peut être prédite par la théorie de la mécanique linéaire élastique de la rupture. En outre, la simulation de fronts de glissement le long d'interfaces hétérogènes démontre une interaction entre les échelles de longueur du front de glissement et de la configuration hétérogène.

Mots-clefs :

fronts de glissement, interfaces de frottement, précurseurs, vitesse de propagation, position d'arrêt, interfaces hétérogènes, mécanique linéaire élastique de la rupture, simulations éléments finis dynamiques

Abstract

Even though friction affects everyday life in many ways, it is still one of the biggest mysteries of physics. Friction is a truly multi-scale phenomenon with a large variety of processes acting at various length and time scales. In recent years, much attention was paid to the micro- and nano-scale properties of frictional interfaces in order to uncover the origins of friction. The structural aspects of friction at the meso- to macro-scales have, however, often been neglected. This thesis aims at demonstrating that these aspects are key to the frictional response of macroscopic systems and pursues therefore the objective of improving today's knowledge of the rupture-like propagation of slip fronts at frictional interfaces.

The mechanics of frictional interfaces is studied with state-of-the-art dynamic finite-element simulations of systems mimicking experimental set-ups. Two and three-dimensional simulations are conducted according to the nature of the studied phenomena. In addition, theoretical models based on fracture mechanics theory are developed and applied to confirm the numerical observations. These models provide insights on the underlying mechanisms of the slip front propagation and reveal the influence of various system, material, and interface parameters.

The results presented in this thesis show that the applied numerical models reproduce quantitatively well experimental observations as reported in literature. The studied aspects of frictional slip include, among others, the propagation speed, the arrest position, and the effect of interface heterogeneity. Beyond confirming experimental observations, the simulations and theoretical models further reveal new features of the propagation and arrest of slip fronts. They show, for instance, that the speed of slip fronts depends on the propagation direction and that the arrest position of slip precursors is predictable with linear elastic fracture mechanics theory. Furthermore, simulations of slip fronts at heterogeneous interfaces uncover an interaction between the length scales of the slip front and the heterogeneous pattern.

Keywords:

slip fronts, frictional interfaces, precursors, propagation speed, arrest position, heterogeneous interfaces, linear elastic fracture mechanics, dynamic finite-element simulations

Contents

Acknowledgements	v
Abstract (Français/English)	vii
List of Figures	xvi
List of Symbols	xvii
1 Introduction	1
1.1 Context	1
1.2 Challenges	3
1.3 Objectives	4
1.4 Approach	5
1.5 Outline of Chapters	6
2 State of the Art	9
2.1 Macro-Scale Observations in Friction Experiments	9
2.2 Local Interface Phenomena of Friction	13
2.2.1 Fracture Mechanics Applied to Frictional Shear Cracks	13
2.2.2 Propagation of Slip Fronts	15
2.2.3 Evolution of Local Frictional Strength	18
2.3 Numerical Models of Frictional Slip	20
2.3.1 Numerical Methods	20
2.3.2 Simulations of Frictional Slip Problems	21
2.3.3 Propagation Speed of Slip Fronts	22
2.3.4 Precursors – the Arrest of Slip Fronts	23
2.3.5 Slip Front Propagation through Interface Heterogeneities	23
3 Theoretical and Numerical Framework	25
3.1 Continuum Solid Mechanics	25
3.1.1 Kinematic Equations	25
3.1.2 Stress Measure	27
3.1.3 Conservation Equations / Balance Principle	27
3.1.4 Constitutive Material Laws	28
3.2 Fundamentals of Contact Mechanics with Friction	31

Contents

3.2.1	Contact Conditions	32
3.2.2	Friction Conditions	33
3.2.3	Friction Laws	33
3.3	Basis of Linear Elastic Fracture Mechanics	35
3.4	The Finite-Element Method	38
3.4.1	Problem Statement	39
3.4.2	Weak Formulation	39
3.4.3	Space Discretization	40
3.4.4	Time Discretization	41
3.4.5	Static Solution	43
3.4.6	Numerical Damping	43
3.5	The Traction-At-Split-Node Method	43
3.5.1	Weak Formulation	44
3.5.2	Node-to-Node Discretization	45
3.5.3	Time Discretization	45
4	A Critical Length Scale in Regularized Friction	47
4.1	Ill-posedness of the Classical Coulomb Friction Law	48
4.2	Simulation Set-up	49
4.3	Influence of Friction Regularization on Slip	52
4.3.1	Mesh Refinement Analysis	52
4.3.2	Length Scale Convergence	54
4.4	Filter Analogy of Frictional Regularization	56
4.5	Physical Interpretation	58
4.6	Conclusion	60
5	Criteria for the Slip Front Speed	63
5.1	Slip Fronts Propagating at Various Speeds	64
5.2	Model Set-up	64
5.3	Results & Discussion	66
5.4	Conclusion	72
6	Predicting the Propagation Distance of Frictional Slip	75
6.1	The Propagation of Slip Precursors	76
6.2	Models	77
6.2.1	Numerical Model	79
6.2.2	Theoretical LEFM Model	80
6.3	Results and Discussion	85
6.3.1	Numerical Simulations	85
6.3.2	Comparison of LEFM Model with Experimental Data	86
6.3.3	Test of Model Assumptions	88
6.3.4	LEFM Prediction for Symmetric Set-up	89
6.4	Conclusion	91

7 Heterogeneous Interface	93
7.1 Slip Front Propagation through Interface Heterogeneities	94
7.2 Simulation Set-up	97
7.3 Homogeneous Reference Cases	99
7.4 Heterogeneous Interface: Dynamic Simulation Results	101
7.4.1 Two Distinct Propagation Mechanisms	101
7.4.2 Length Scale Interactions	104
7.4.3 Energy Dissipation	109
7.5 Conclusion	111
8 Concluding Remarks	113
8.1 Summary	113
8.2 Outlook	115
A Details to the Study of Regularized Friction	119
A.1 Description of the Nucleation Procedure	119
A.2 Regularization: Derivation of the Analytical Solution	120
Bibliography	123
Curriculum Vitae	139

List of Figures

1.1	Simplified schematic illustration of the multi-scale nature of friction.	4
2.1	Illustration of da Vinci's set-up for friction experiments	10
2.2	Experimental results of rate-dependent and time-dependent friction coefficient, and schematic behavior of rate- and state-dependent friction.	11
2.3	Schematic illustration of stick-slip motion of a spring-mass system.	12
2.4	Schematic illustration of a sharp crack tip and a cohesive zone crack tip.	14
2.5	Illustration of crack-like and pulse-like interface ruptures.	16
2.6	Illustration of arrest of a sequence of slip fronts.	18
2.7	Evolution of friction force to a sudden jump in the normal force.	19
3.1	Lagrangian description of a continuum body.	26
3.2	One-dimensional representation of constitutive material laws.	28
3.3	Schematic illustration of viscoelastic response to a strain jump.	30
3.4	Representation of contact conditions.	32
3.5	Representation of friction laws.	34
3.6	Three rupture modes: normal, in-plane shear, and out-of-plane shear fracture.	36
3.7	Schematic illustration of finite-element mesh.	40
4.1	Simulation set-up to study regularized friction.	50
4.2	Example of slip front propagation at a deformable-rigid frictional interface.	51
4.3	Illustration of mesh convergence for a regularized frictional interface rupture.	53
4.4	Illustration of convergence with respect to the characteristic length of the friction regularization.	55
4.5	Frequency analysis of the simplified Prakash-Clifton friction law.	57
4.6	Illustration of the zone of influence of the Prakash-Clifton friction regularization.	60
5.1	Two-dimensional set-up to study the slip front speed.	65
5.2	Comparison of numerical and experimental results for the rupture speed of frictional slip fronts.	67
5.3	Velocity field in the bulk of three slip events (one spontaneously initiated and two artificially triggered).	68
5.4	Normalized rupture speed with respect to the static interface traction ratio for three slip events.	69

List of Figures

5.5	Illustration of the dynamic evolution of interfacial stresses.	70
5.6	Normalized rupture speed with respect to the dynamic interface traction ratio for three slip events.	71
5.7	Normalized rupture speed with respect to a dynamic criterion based on a heuristic surface energy density for three slip events.	72
6.1	Set-up of side-driven system with static stress states of the interface for normal and shear load.	78
6.2	Shear tractions, fracture toughness and stress intensity factor for an interface before and after the propagation of a slip front.	81
6.3	The evolution of the stress intensity factor is shown during the period between two precursors.	84
6.4	Numerical results presenting global force ratio and local slip regions with respect to time.	85
6.5	Comparison of the LEFM model, with dynamic simulation, and experimental data.	86
6.6	Analysis of the influence of different interface and material parameters on the precursors load-length prediction of the LEFM model.	87
6.7	Precursor load-length relation for various simplified LEFM models.	89
6.8	Precursor load-length relation prediction for symmetric set-up with comparison to reference system.	90
7.1	Three-dimensional set-up for simulations with heterogeneous interfaces.	96
7.2	Configuration of heterogeneous interface.	97
7.3	Sub-Rayleigh slip front at a homogeneous interface.	99
7.4	Slip front transitioning from sub-Rayleigh to inter-sonic propagation due to a modified fracture energy of the interface.	101
7.5	Interface snapshots of slip area at two different heterogeneous interfaces.	102
7.6	Propagation speed at heterogeneous interface.	104
7.7	Interface snapshots of slip area, slip distance, frictional strength, and shear traction during the transition from the homogeneous to the heterogeneous area.	105
7.8	Propagation speed for heterogeneous system with different material and interface properties.	108
7.9	Energy dissipation at various interfaces with homogeneous and heterogeneous frictional properties.	110
7.10	Frictional energy dissipation as a function of the characteristic length of the heterogeneity pattern.	111
A.1	Visualization of imposed artificial interface pressure causing slip initiation.	120

List of Symbols

A	crack area	L	length
A^s	amplitude of frictional strength oscillation	\mathbf{M}	mass matrix
A^{es}	amplitude of effective fric. strength oscillation	N_I	shape function (for node I)
\mathbf{B}	boundary matrix	\mathbf{P}	first Piola-Kirchhoff stress tensor
\mathbf{C}	damping matrix	R	resistance curve
C_c	contact contribution to weak form	S	seismic ratio
E	Young's modulus	S_0	reference domain boundary
E_∞	static Young's modulus	S_0^t	traction domain boundary
E_v	viscous Young's modulus	S_0^u	displacement domain boundary
E_0	instantaneous Young's modulus	S_0^{c1}, S_0^{c2}	contact domain boundaries
\mathbf{E}	Green-Lagrange strain tensor	T	dynamic contribution to process zone size
\mathbf{F}	deformation gradient tensor	\mathcal{U}	trial domain
F_N	normal force	\mathcal{U}_0	test domain
F_s	shear force	U	strain energy
F_f	friction force	\tilde{U}	heuristic energy density
F_{sf}	static friction force	\tilde{U}_s	rupture tip energy density
F_{kf}	kinetic friction force	\tilde{U}_r	yield energy density
G	shear modulus	V	volume
G_∞	static shear modulus	V_0	reference volume
G_v	viscous shear modulus	W	width, wavelength of heterogeneous strips
\mathbf{G}	contact disp. constraint matrix	W_f	work against friction
H	height	W_s	work required to create a new interface
\mathbf{H}	displacement gradient tensor		
\mathbf{I}	identity matrix		
J	Jacobian of deformation gradient	a	crack (half) length
K	bulk modulus	a_0	initial crack (half) length
K_∞	static bulk modulus	a_{ell}, b_{ell}	ellipse minor/major half diagonal
\mathbf{K}	stiffness matrix	\mathbf{b}	body force
K_s	spring stiffness	c_d	dilatational wave speed
K_I, K_{II}	stress intensity factor (mode I, II)	c_R	Rayleigh wave speed
K_{Ic}	fracture toughness (mode II)	c_s	shear wave speed

List of Symbols

d_c	char. slip-weakening length	t_0	reference time
d_{pc}	char. Prakash-Clifton (PC) length	Δt	time step
d_{crit}	critical char. PC length	\hat{t}	most recent stick time
d_{ph}	physical char. PC length	t_v	char. viscous relaxation time
d_m	measured char. PC length	t_{pc}	char. Prakash-Clifton time
f	frequency	u	displacement field
f_{crit}	critical frequency	Δu	relative disp. field (slip)
f_m	measured critical frequency	\mathbf{u}	displacement field, nodal displacement vector, trial function
\mathbf{f}^{int}	internal nodal force vector		
\mathbf{f}^{ext}	external nodal force vector		
f_{ij}	dimensionless function for LEFM	$\delta \mathbf{u}$	test function of disp. field
g_{ij}	dimensionless function for LEFM	\mathbf{u}^i	initial displacement field
\mathbf{g}	gap vector	$\bar{\mathbf{u}}$	imposed boundary displacement
\mathbf{g}_0	reference gap vector	\bar{u}_y	imposed boundary disp. value
g_N	length of normal gap	$\ddot{\mathbf{u}}$	material acceleration field, nodal acceleration vector
\mathbf{g}_T	tangential gap vector		
$\dot{\mathbf{g}}$	gap rate	$\delta \ddot{\mathbf{u}}$	nodal accel. increment vector
$\dot{\mathbf{g}}_T$	tangential gap rate	\mathbf{v}^i	initial velocity field
\mathbf{g}^a	adapted gap vector	v_{pc}	char. Prakash-Clifton velocity
g_N^a	adapted normal gap length	v_{ell}	ellipse inclination in space-time
\mathbf{g}_T^a	adapted tangential gap vector	\bar{v}_x	displacement loading rate
δg_N^a	test function of normal gap	v_r	rupture speed
$\delta \mathbf{g}_T^a$	test function of tangential gap	w_{pz}	process zone size
\mathbf{g}_t	previous stick gap vector	w_p	pusher width
h_p	pusher height	x	cartesian coordinate, current point
l	precursor length		
l_a, l_b	limits of process zone	x_0	reference point
l_n	nucleation length	\mathbf{x}_0	reference position
l^*	length scale for dynamic stresses	\mathbf{x}	current position
\mathbf{n}	boundary normal vector	\tilde{x}_0	pair point for contact point
n_d	node density of interface	$\tilde{\mathbf{x}}_0$	position of pair point
n_{npe}	number of nodes per element	y	cartesian coordinate
\bar{p}	normal traction load	z	cartesian coordinate
\bar{p}_a	artificial (fluid) pressure		
r	polar coordinate		
\mathbf{r}	contact reaction/force vector	Γ	energy release rate
r_N	normal contact reaction	Γ_c	critical energy release rate, fracture energy
\mathbf{r}_T	tangential contact reaction		
r_F	frictional strength	Λ	Lagrange multiplier (LM) vector
$\bar{\mathbf{t}}$	boundary traction vector	Λ_N	normal Lagrange multiplier
\bar{t}	shear traction load	Λ_T	tangential Lagrange multiplier
t	time	$\delta \Lambda_N$	test function of normal LM
		$\delta \Lambda_T$	test function of tangential LM

Π	potential energy	ρ_0	density in ref. configuration
Ω	current domain	$\boldsymbol{\sigma}$	Cauchy stress tensor
Ω_0	reference domain	σ	normal stress
		σ_u	normal stress when $\tau = \tau_u$
α	exp. rate-weakening parameter	σ_N	normal stress due to normal load
β	Newmark integration parameter	σ_s	normal stress due to shear load
γ	Newmark integration parameter	σ_r	normal stress after r ruptures
δ	slip	σ_{st}	static normal stress
$\dot{\delta}$	slip rate	σ_{dy}	dynamic normal stress
$\boldsymbol{\varepsilon}$	infinitesimal strain tensor	σ_{ij}	component of Cauchy stress tensor
$\dot{\boldsymbol{\varepsilon}}$	strain rate tensor	τ	shear stress
ζ	non-dimensional parameter for length scale interaction	τ_u	yield shear stress
ζ_a	approximation of non-dimensional parameter	τ_0	ambient shear stress
		τ_f	kinetic friction shear stress
η	viscosity	$\Delta\tau_{pz}$	process zone shear stress difference
θ	polar coordinate	τ_N	shear stress due to normal load
λ	Lamé's first parameter	τ_s	shear stress due to shear load
λ_v	viscous Lamé's first parameter	τ_r	shear stress after r ruptures
λ_∞	static Lamé's first parameter	τ_{st}	static shear stress
μ	friction coefficient	τ_{dy}	dynamic shear stress
μ_s	static friction coefficient	τ^s	frictional strength
μ_k	kinetic friction coefficient	τ^{es}	effective frictional strength
μ_M	macroscopic friction coefficient	ϕ	friction weakening rate
ν	Poisson's ratio	χ	position mapping
ρ	density	ω	angular frequency

1 Introduction

1.1 Context

Friction is the resistance that solids encounter when they slide over each other.¹ As such, friction affects our lives in many ways every single day. It is present between the tire and the road when we drive with our cars. At classical concerts, we listen to violin music that originates from vibrations caused by friction between the strings and the bow. And when we wait in a cold winter night outside, we rub our hands so that friction provides us with a little bit of heat.

Apart from these everyday examples, friction also plays an important role in the manufacture industry. Being present at the interface of gears and other moving parts in machines, friction is sometimes needed in order to enable the apparatus to fulfil its purpose. Other times, friction reduces the production efficiency or causes wear on machine components. It therefore has an important economical impact, which was first estimated by Jost (1966) stating that the UK could save up to 1% of its gross national product if friction was better understood. Persson (1994) later estimated that developed countries lose about 5% of their gross national products due to friction and wear.

Another friction-related problem of great importance to humanity is earthquakes and their unpredictability. At the origin of many earthquakes is relative motion between tectonic plates, which leads to an energy build-up in the crust of the Earth. Once the frictional strength of the tectonic interface is reached, the energy is released in form of seismic waves. The variability in intensity, speed and potential of destructibility is enormous and the prediction of earthquakes is still out of reach but needed to reduce their deadliness and economic impact.

Considering the relevance of friction for a wide variety of applications, it is not surprising that our society looks back at a long history of research on this phenomenon. Centuries ago, Leonardo da Vinci (1452-1519) discovered the first basic friction laws by showing that the frictional resistance is proportional to the normal load and independent of the apparent area

¹Friction also occurs at lubricated interfaces, where the solids are separated by a fluid. This phenomenon is, however, beyond the scope of this thesis and attention is here limited to unlubricated friction.

Chapter 1. Introduction

of contact. These observations were later verified and published by Amontons (1699) and Coulomb (1785) introducing also the coefficient of friction $\mu = F_F/F_N$, which is the proportionality between the frictional force F_F and the normal load F_N . Moreover, Coulomb discovered that static friction, the force needed to start sliding, is generally higher than kinetic friction, which acts during sliding.

The so-called second Amontons-Coulomb friction law, which states that the friction force is independent of the apparent contact area, seems counter-intuitive to most people and constituted therefore for a long time a puzzle to many scholars. It was already mid-twentieth century, when Holm (1938) as well as Bowden and Tabor (1942b) revealed that, due to surface roughness, the real contact area is considerably smaller than the apparent contact area and that it is the real contact area that is proportional to the normal load. These theoretical findings were later confirmed by Dieterich and Kilgore (1994) with direct observations using transparent samples, where areas of contact were visualized by transmitted light.

The most popular parameter of friction, the static friction coefficient, has for a long time been, and is often in engineering still regarded as a material and/or interface property, for which one can find experimental values given in textbook tables (Blau, 2009). However, a more realistic view of friction exists today but is still far from being established. Some evidences of inaccuracy of the classical friction theory were provided by Rabinowicz (1992) showing that for a given experimental set-up, the static friction coefficient of a gold-on-gold interface varies from 0.32 up to 0.80. Fluctuations of the same order were also observed by Ben-David and Fineberg (2011) when the loading conditions of a given acrylic-glass interface were changed.

These large variations in the friction coefficient are clear indicators that the mechanics of sliding and its related forces is more complicated than assumed so far. Rubinstein et al. (2004) observed by real-time visualization of the real contact area of an acrylic-glass interface that the onset of dynamic friction features local slip fronts. These rupture-like events propagate over the entire or parts of the interface and might be key to the understanding of frictional sliding. A similar mechanism of dynamic shear-crack propagation is at the origin of many earthquakes and has been studied for decades (Scholz, 2002).

A better understanding of these local dynamic phenomena is therefore needed to achieve profound knowledge of fundamental earthquake mechanisms and to possibly predict, in the future, imminent earthquakes. But mastering the dynamics of friction is also required to strengthen the manufacturing industry by improving today's technology and reducing friction-related losses. However, studying local phenomena of friction and the onset of sliding presents a variety of challenges, which are outlined in the following section, and requires therefore a number of different scientific approaches including numerical simulations and theoretical mechanics, which are the two pillars of this thesis.

1.2 Challenges

The study of friction has long been limited to macroscopic experiments where, in a simplified description, a block of a given material was subjected to a normal load and pulled by a cord. The needed pulling force was measured and analyzed with respect to the material property, the normal load, the contact area and the sliding speed. Detailed information about what happens at the interface could not be accessed because the object of interest – the interface – is hidden behind the bulk material of the samples. Only few qualitative observations could be deduced from *post-mortem* examinations of the sliding interfaces.

This main challenge for the investigation of local phenomena in frictional sliding has been partially overcome by different visualization techniques (Kragelskii, 1965; Dieterich and Kilgore, 1994; Rubinstein et al., 2004; Yamaguchi et al., 2011). All these approaches rely on the transparency of the bulk material, some kind of light source and a camera. Knowing that the interface transmits light only at points of contact and scatters it everywhere else, the real contact area can be recorded and visualized by the camera through a light intensity measurement. By tracking the real contact area of an interface during a friction experiment, it was, for instance, possible to confirm the proportionality between the normal load and the real contact area (Dieterich and Kilgore, 1994), and to study the propagation speed of local slip events (Rubinstein et al., 2004; Ben-David et al., 2010). Nevertheless, these measurement techniques are limited to few transparent materials and constrain a systematic study of frictional slip.

Overcoming the challenges of studying frictional slip experimentally requires additional insights from computational research. Numerical simulations provide direct access to information at the interface. Contact pressure, frictional tractions, state variables, slip velocity and any other observable phenomenon can be computed or measured numerically at the interface without the limitation of bulk transparency. Furthermore, simulations give flexibility of changing easily the geometry or the material properties of the set-up. This also provides the possibility of simplification and thus enables the investigation of the influence of different aspects, such as material or interface properties. Another asset of numerical simulations is high resolution in time and space, which is important for fast phenomena such as slip events with propagation durations of the order of micro-seconds or shorter.

Even though numerical modeling presents an essential opportunity to support experimenters in studying the mechanics of local slip and the dynamics of friction phenomena, they also bear challenges. Knowing that friction is a truly multi-scale phenomenon with various processes acting at all length scale, as shown schematically in Figure 1.1, it is impossible with today's computational resources to include all types of interactions at all scales into one single numerical model. It is, therefore, crucial to “design” an accurate representation including all necessary processes at the essential scales for the studied problem in order to produce meaningful results that lead to significant insights. At the meso- to macro-scale, which is the objective of this thesis, the solid samples need to be modeled as a continuum, which is classically done using the finite-element method. The simulation of the mechanics of the

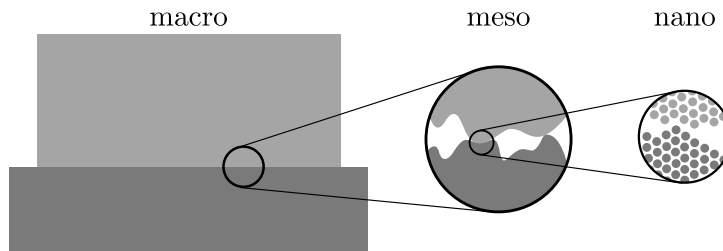


Figure 1.1: Simplified schematic illustration of the multi-scale nature of friction. Various processes at different length scales contribute to the macroscopic friction force.

interface – the discontinuity in the continuum – requires, however, a modern and advanced contact and friction model. For the purpose of studying dynamic slip events, it is important that the applied method is precise in terms of energy conservation/dissipation and minimizes numerical errors.

Asides from pure technical aspects, additional challenges arise from Coulomb’s friction law, which is, in mathematical terms, ill-posed under certain conditions at interfaces between solids of different material properties (Renardy, 1992; Adams, 1995). The exact implications of this ill-posedness for variations of this basic friction law and different interface stress states are still not well understood but may impact numerical results considerably. Bulk viscoelasticity and friction law regularization (Cochard and Rice, 2000) appear to have a stabilizing effect but change the physical basis of the modeled system. The absence of profound knowledge about the conditions under which the ill-posedness of Coulomb’s friction law occurs and how a friction regularization affects the numerical results, requires a careful development of the model.

Finally, it is a fundamental problem to set up a model that is sufficient but not too complex.² A lack of complexity could lead to incomplete or even wrong discoveries, and too sophisticated models might represent an obstacle to gaining profound knowledge about the studied system. More particularly for simulations of friction, it is essential to apply appropriate constitutive equations for the interface as well as the bulk materials, and to create a precise model with accurate geometry and boundary conditions.

1.3 Objectives

The main objective of this thesis is to improve our knowledge of the mechanics of local slip at frictional interfaces by conducting numerical simulations. It is therefore a study of the rupture-like propagation of slip fronts and aims at a better understanding of the link between meso- and macro-scale phenomena of friction. In particular, this work focuses on different aspects of slip front propagation, including:

²Or to say it with Albert Einstein’s words: “Everything must be made as simple as possible. But not simpler.”

- **Local frictional strength:** Studying meso-scale friction laws that are regularized with respect to changes in the contact pressure and analyzing the effect of the underlying characteristic length scale on the propagation of slip fronts.
- **Propagation speed:** Studying the behavior of slip fronts at interfaces with non-uniform stress distributions and describing the propagation speed as a function of the interface stress state.
- **Slip arrest:** Analyzing the spontaneous arrest of slip fronts at positions far from the edges of the interface and examining the influence of the macroscopic set-up on the arrest position.
- **Interface heterogeneities:** Illustrating the propagation of slip fronts at interfaces with heterogeneous patterns and studying the effects of the interaction between the characteristic length scales of the slip front and the heterogeneous configuration.

Considering that friction is a multi-scale phenomenon, it is important to emphasize that the studied aspects concern the mechanics of meso- to macro-scale friction at unlubricated dry interfaces. Friction mechanisms occurring at smaller scales, as for instance the mechanics of asperities or atomistic friction, are out of scope for this work. However, their contributions are integrated into meso-scale friction laws applied at the interface.

1.4 Approach

Given the objective of modeling meso- and macro-scale aspects of frictional sliding, a continuum approach is most suited to represent well the length and time scales of the studied system and phenomena. The finite-element method, which is applied for the simulations conducted for this thesis, is a well-established modeling technique that incorporates correctly the continuum nature of the solid bodies. Furthermore, the finite-element method allows the integration of additional tools necessary to represent the interface discontinuity. The in-house developed finite-element research code named Akantu (Richart and Molinari, 2014; LSMS-EPFL, 2014) is used and extended according to the needs for fulfilling the objectives.

The goal of this work is to study fast dynamic phenomena of frictional sliding, which occur over short time periods. Explicit time integration schemes with a lumped mass matrix are a well-suited approach to study such problems efficiently. In addition, we employ occasionally static methods to compute initial conditions for dynamic simulations.

The propagation of slip fronts is modeled with a cohesive-type approach similar to modeling techniques of crack propagation. The applied traction-at-split-node method uses meso-scale laws for interface tractions. This combines cohesive forces within the process zone (where the interface breaks) and friction forces in the slip region. The discontinuity at the interface is handled by splitting nodes into two nodes and by applying cohesive and friction tractions at the node level. This method is particularly efficient and minimizes numerical noise, but

requires small displacement discontinuities at the interface. This small-slip condition is satisfied for problems studied in this work.

In addition to numerical simulations, we apply theoretical approaches to analyze the phenomena of frictional slip. This should not only emphasize the validity of the numerical results, but also provide a tool to a better understanding of the mechanics of the observed behavior. It also indicates the influence of different material and interface properties. The applied approach is based on an analogy of friction and fracture. It thus benefits from the existing knowledge of fracture mechanics and strengthens the notion of slip fronts being a fracture mechanics phenomenon.

1.5 Outline of Chapters

This thesis is organized in eight chapters, which are here briefly summarized:

- **Chapter 2 – State of the Art:** A summary of previous work about unlubricated dry friction. It first presents main results from large-scale experiments, showing that macroscopic friction is, under different conditions, slip-, rate- and/or state-dependent. Further, this chapter presents fundamental results of fracture mechanics applied to shear cracks, summarizes various phenomena occurring during the propagation of slip fronts, and explains current knowledge about behavior of local frictional strength. This chapter also summarizes important results of numerical simulations related to frictional slip propagation.
- **Chapter 3 – Theoretical and Numerical Framework:** A description of applied theories and numerical methods. This chapter provides the basics of continuum mechanics, contact mechanics with friction, and linear elastic fracture mechanics. It also describes the fundamental theory about the finite-element method and the traction-at-split-node method.
- **Chapter 4 – A Critical Length Scale in Regularized Friction:** An analysis of the effect of friction regularization on a local slip event. This chapter first confirms mesh convergence for a given slip event at a regularized deformable-rigid interface without any numerical damping in the bulk. It further shows that there is a critical length scale below which the friction regularization does not affect the propagation of the slip front. This indicates that slip regions with characteristic regularization lengths below the critical length propagate as if the interface was governed by Coulomb's friction. A domain of influence, which is defined in this chapter, determines the property of the slip event needed to achieve experimental observation of the characteristic length and shows that the amount of energy in the high-frequency domain of the slip event is the critical factor.
- **Chapter 5 – Criteria for the Slip Front Speed:** A study of different criteria describing the propagation speed of slip fronts at frictional interfaces. This chapter first demonstrates

that a numerical model reproduces recent experimental observations showing that the rupture speed is closely related to the shear to normal stress ratio at the interface. It further highlights that slip fronts propagating in opposite directions do not present the same rupture speed for a given stress ratio. In order to improve the description of the slip front speed, two dynamic criteria are proposed and analyzed. While a simple dynamic stress criteria shows a smaller but still non-negligible difference with respect to the front direction, a dynamic energy-based approach provides a unique stress-speed relation.

- **Chapter 6 – Predicting the Propagation Distance of Frictional Slip:** An analysis of the mechanics of arresting slip fronts. This chapter presents numerical and theoretical models to simulate the propagation of slip precursors, which arrest naturally before reaching the edge. The main theoretical model considers slip fronts as interface ruptures and uses linear elastic fracture mechanics to predict the propagation distance. The comparison with experimental data and the analysis of the influence of different interface and material parameters show that the fracture mechanics based model provides a good quantitative prediction of slip arrest. This observation offers evidence to recognize frictional slip as a fracture phenomenon.
- **Chapter 7 – Heterogeneous Interface:** A study of the propagation of slip fronts at frictional interfaces with an organized heterogeneous pattern. This chapter presents the results of three-dimensional numerical simulations of slip fronts at an interface with a striped heterogeneous area. The strips are alternatively characterized by higher and lower fracture energy leading in homogeneous systems to sub-Rayleigh and inter-sonic propagation, respectively. The simulations show that two distinct propagation mechanisms exist and appear depending on the wavelength of strip configuration. A non-dimensional parameter linking the characteristic length scale of the slip front and the heterogeneous pattern is proposed and shown to determine well the propagation mechanism occurring in a given system.
- **Chapter 8 – Concluding Remarks:** A summary of the conclusions of the various studies on the propagation of slip fronts at frictional interfaces. In addition, an outlook for potential future research on frictional slip in complex systems is provided.

2 State of the Art

Being of great importance to our society, friction has been studied for centuries. With time our knowledge about this complex phenomenon as well as our tools to study it have improved considerably. Nevertheless, there are still uncountable mysteries about the origins of friction.

This thesis addresses the dynamics of meso-scale friction phenomena, such as the propagation of local slip regions along interfaces with non-uniform stress states, and the link between the mechanics of meso-scale friction and the macro-scale response of solid body systems with interfaces. The objective of this chapter is to summarize the current state of knowledge about meso- and macro-scale friction with a particular focus on previous numerical results. As such, this chapter reports on

- the experimental observations of macroscopic friction,
- the mechanics of frictional interfaces at the meso-scale, and
- the numerical simulations of the propagation of local slip regions.

This chapter is limited to physical and mechanical aspects of frictional slip, and does not explain experimental nor numerical techniques in details. The theoretical and numerical framework of simulation tools applied in this thesis are described in details in Chapter 3.

2.1 Macro-Scale Observations in Friction Experiments

Most macro-scale friction experiments consist of two solids that are brought into contact. While a normal load is kept constant, the shear load is slowly increased until the two solids are sliding over each other. By measuring the maximal value of the shear load, the experimenter finds the static frictional strength of the interface. First friction experiments of this kind were conducted by Leonardo da Vinci with a set-up as schematically shown in Figure 2.1. A test object is placed on a flat surface and loaded by a weight. Using gravity acting on a free weight,

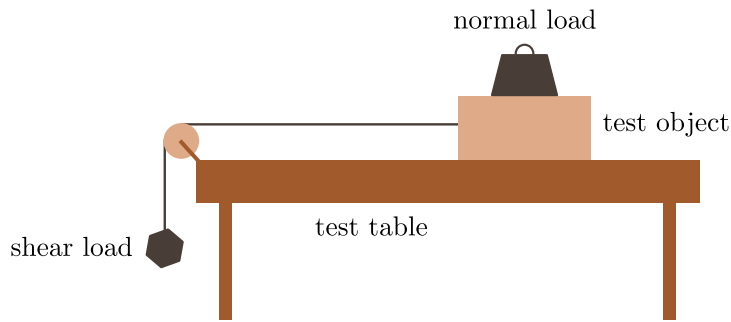


Figure 2.1: Illustration of da Vinci's set-up for friction experiments. A test object is placed on a test table and loaded by a weight. A shear load is applied to the test object by a free weight via a coil at the edge of the table. The frictional strength of the interface is determined by the weight which sets the test object in motion.

he applied a shear load to the test specimen via a coil. The shear load leading to sliding was then interpreted as the frictional strength of the tested interface.

Later, similar experiments by Amontons (1699) and Coulomb (1785) led to the definition of the well-known coefficient of friction μ , which corresponds to the ratio of the friction force to normal load. This is usually expressed as the so-called Coulomb friction law or Amontons' first law as

$$F_F = \mu F_N, \quad (2.1)$$

where F_F is the friction force and F_N the normal load. Furthermore, these experiments showed that the friction force is independent of the apparent contact area. This counter-intuitive discovery was later shown to be caused by the micro-roughness of interfaces resulting in real contact areas that are much smaller than the apparent contact area (Holm, 1938; Bowden and Tabor, 1942a; Dieterich and Kilgore, 1994). Often the ratio of the real to apparent contact area is below 1%.

Other macro-scale experiments showed that the friction force is generally not constant and that various parameters influence it. Slip rate is one of the most prominent friction parameters. Depending on the order of the slip rate, its acceleration can result in an increase or decrease of the friction force. First experimental evidence of rate-dependent friction was reported by Burwell and Rabinowicz (1953). An example of typical experimental results of rate-dependent friction is shown in Figure 2.2(a). Slip distance has also been shown to affect the friction force (Rabinowicz, 1956). Interfaces following a slip-weakening friction process often present a characteristic length which describes the slip distance needed to decrease frictional strength from the static to the dynamic value.

Another parameter affecting the friction force was found to be the waiting time between two consecutive slip periods. A logarithmic time-dependence of the static friction coefficient

2.1. Macro-Scale Observations in Friction Experiments

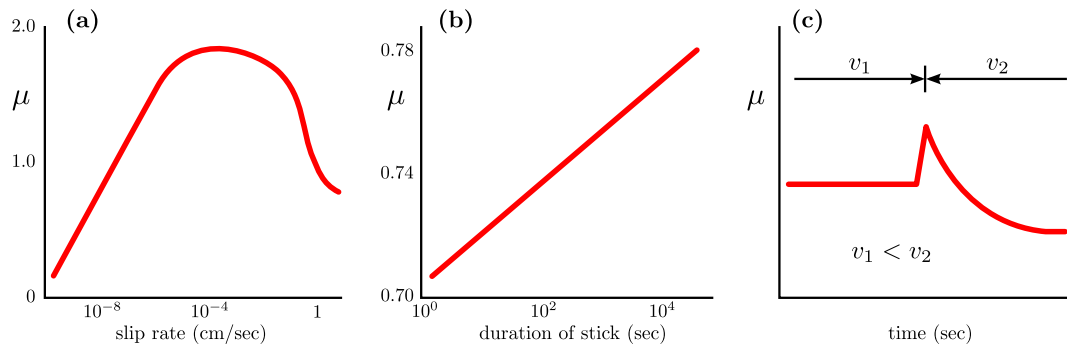


Figure 2.2: **(a)** General trend of experimental results of a steel-indium interface showing rate-dependent macroscopic coefficient of friction. Figure adapted from Burwell and Rabinowicz (1953). **(b)** Trend of experimental data for waiting time-dependent coefficient of static friction of a sandstone interface under 18.7 MPa normal load as reported by Dieterich (1972). **(c)** Schematic rate- and state-dependent reaction of the coefficient of friction for a sudden change in the loading rate.

was observed in experiments at various rock interfaces with a gouge zone (Dieterich, 1972) as well as at metallic interfaces (Rabinowicz, 1965). In some cases, the reference value of the static friction coefficient corresponds to the kinetic friction coefficient for waiting times approaching zero (Dieterich, 1972).

Experiments with sudden changes of the loading rate showed that the friction force adapts to the new rate over a characteristic slip distance (Dieterich, 1978, 1979). As shown in Figure 2.2(c), an instantaneous jump of the loading rate results in a quasi-immediate change of the friction force followed by a phase of transition to a new steady state. Considering that the real contact area consists of a collection of micro-contacts, sliding results in continuous renewing of the micro-contact population. This leads to two competing processes, which are contact zones that become stronger with time (the time-dependent effect) and contact zones that are replaced by weaker zones (the velocity-dependent effect). This approach led to a variety of more advanced friction laws, often referred to as rate- and state-dependent friction laws (Dieterich, 1978, 1979; Ruina, 1983; Rice and Ruina, 1983). They describe the behavior shown in Figure 2.2(c) with a rate and a state variable, where the latter usually depends on the past slip rates.

Typical rate- and state-dependent friction laws predict variations of the friction coefficient of the order of 10% because the experiments on which these laws are based used slow loading rates ($10^{-5} - 10^{-1}$ mm/s). However, slip rates occurring in dynamic systems, such as in tectonic faults during an earthquake, can reach much higher values (up to 1 m/s). Experiments have shown that at these rates the frictional strength of an interface can drop to considerably lower values than predicted by rate- and state-dependent friction laws. The experiments of Di Toro et al. (2004) suggest that the frictional resistance of quartz rock interfaces may reach zero for seismic slip rates. Reches and Lockner (2010) observe in their experiments at

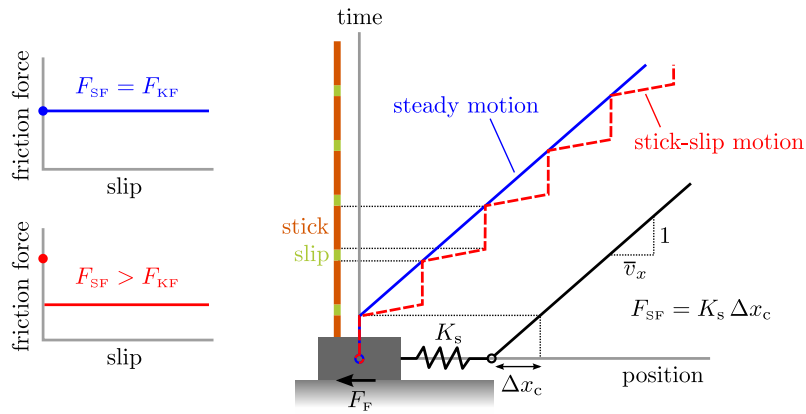


Figure 2.3: Schematic illustration of stick-slip motion of a spring-mass system. The spring of stiffness K_s is pulled with constant speed \bar{v}_x . The solid black line indicates the spring position. The block starts to move when the spring force reaches the static friction force $F_{SF} = K_s \Delta x_c$. If the friction force F_F is governed by Coulomb's law without weakening, $F_{SF} = F_{KF}$, the block enters steady motion (solid blue line indicates the position). However, if the friction force weakens with slip, $F_{SF} > F_{KF}$, (for simplicity instantaneous weakening is assumed), the block accelerates beyond \bar{v}_x and enters a stick-slip regime (dashed red line indicates the position).

a granite interface a reduction of the frictional strength of a factor two to three for slip rates at 10 – 60 mm/s. Similar observations were made by Goldsby and Tullis (2011) on quartzite interfaces.

The weakening process of frictional strength during sliding (independent of whether it is slip-, rate- or state-dependent) is at the roots of a macroscopic friction phenomenon called stick-slip motion (Scholz, 2002). It is the repetition of periods of interfacial slip followed by periods of stick. In a simple system consisting of a block lying on a surface and being pulled by a spring, motion is steady if the weakening rate of the friction force is lower than the spring stiffness. However, if this is not the case, then the block enters a stick-slip regime because the driving force of the spring is stronger than the resisting friction force, which leads to the acceleration of the block. Once motion unloaded the spring, the decelerating friction force causes the block to stop. After arrest, the spring is loaded until the next slip period. An illustrative example of stick-slip motion is presented in Figure 2.3. Depending on the loading velocity and the spring stiffness, the transition from steady motion to stick-slip was shown to be either creep-like or inertial (Baumberger et al., 1994; Heslot et al., 1994).

Even though macroscopic friction presents systematic behavior, such as rate- or waiting time-dependence, it also produces large variability. The measured static friction force for a given pair of solids can vary up to a factor two, as shown by Rabinowicz (1992). Under low normal loads, he observed static friction coefficients of a gold-on-gold interface ranging from 0.32 up to 0.8. Similar experimental measurements were, more recently, reported by Ben-David and Fineberg (2011). These large variations in the macroscopic friction force suggest that

the underlying mechanism is complex and that the local phenomena at the interface play an important part in the global response of the system. Therefore, a substantial effort was made to study the local mechanics of interfaces.

2.2 Local Interface Phenomena of Friction

In addition to studying the macroscopic response of a system containing a frictional interface, it seems obvious that the important friction mechanisms occur locally at the interface. It is therefore no surprise that the mechanics of interfaces is a subject of great importance. However, it is also obvious that observing the interface is challenging because of its hidden position behind the bulk of the solids in contact. Different approaches have been used in the past to gain knowledge about the mechanics of interfaces. This section summarizes the main results related to the description of frictional shear cracks with fundamental concepts of fracture mechanics, the observation of the propagation and various phenomena occurring during the propagation of slip fronts including the analysis of the local frictional strength and its development during sticking and sliding.

2.2.1 Fracture Mechanics Applied to Frictional Shear Cracks

It has been known for a long time that earthquakes are essentially periods of slip between tectonic plates. It was also understood that earthquakes initiate at a given point, called the hypocenter, and propagate along the interface. Combining these two points, one can (rather easily) conclude that earthquakes are shear cracks at a frictional interface. Even though this reasoning was first made in the context of earthquake mechanics, it is just as valid for any slip front propagating at any frictional interface, including man-made interfaces.

From fracture mechanics, it is known that the presence of a crack in an elastic solid results in stress singularities at the tip of the crack, which is physically not possible for real materials. As suggested by Barenblatt (1959), a possibility for eliminating these singularities are cohesive forces acting across the crack in a limited (cohesive) zone around the tip. One can think of these forces as the resistance that needs to be overcome to increase the crack size by creating new surfaces. Various slip-dependent cohesive laws were proposed by Ida (1972) and shown to remove the crack tip singularity. A popular cohesive force description is the linear slip-weakening law, which has since been used in many earthquake-related simulations (Andrews, 1976b; Day, 1982b; Madariaga and Olsen, 2000). The concept of fracture mechanics was also applied to the growth of slip surfaces in over-consolidated clays (Palmer and Rice, 1973).

Linear elastic fracture mechanics with a cohesive zone approach, as used for frictional shear cracks, is a solid tool to describe the propagation of slip fronts at frictional interfaces. Andrews (1976a,b) showed on an antiplane and on a plane-strain shear crack that energy considerations based on fracture mechanics enable the possibility of identifying a critical crack length beyond which the rupture will propagate.

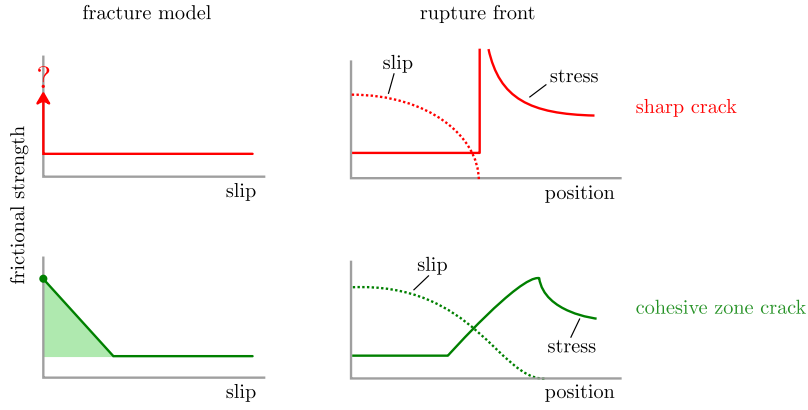


Figure 2.4: Schematic illustration of a sharp crack tip (top sub-figures with red lines) and a cohesive zone crack tip (bottom sub-figures with green lines). The left column illustrates the fracture models, and the right column the slip and stress of a rupture tip propagating to the right side. The static strength of the sharp crack is infinite (red question mark) which leads to a stress singularity in front of the rupture tip. The cohesive zone crack tip is smoothed in space because the stress drop occurs over a finite length. The fracture energy of the cohesive model is indicated by the green area. Figure adapted from Andrews (1976a).

An illustrative example, which was studied by Andrews (1976b), consists of a plane-strain shear crack obeying a rupture model in which the interface stress decreases gradually with increasing slip. The initial stress level τ_0 satisfies $\tau_u > \tau_0 > \tau_f$, where τ_u is the yield stress and τ_f is the kinetic friction stress of the interface. A static crack of length $2a$ is created by slowly decreasing τ from τ_0 to τ_f . As a result, the displacement field u (and slip Δu) adapts to the new stress state. The virtual work done during this process corresponds to the strain energy and can be computed by

$$U = -\frac{1}{2}(\tau_0 + \tau_f) \int \Delta u \, dx, \quad (2.2)$$

where x is the position along the crack. The work done against friction corresponds to

$$W_f = \tau_f \int \Delta u \, dx. \quad (2.3)$$

The net work is therefore given by

$$U + W_f = -\frac{1}{2}(\tau_0 - \tau_f) \int \Delta u \, dx. \quad (2.4)$$

If the crack length is increased by an increment da , the energy available to create new surfaces and hence to extend the crack is

$$-dU - dW_f = \Gamma(\tau_0 - \tau_f) \, da, \quad (2.5)$$

where Γ , often referred to as the energy release rate, is a function of the stress drop $\tau_0 - \tau_f$. Its

form depends on the displacement field of the crack and varies for different set-ups. Crack growth occurs if, for a length increment da , the available energy Γ exceeds the fracture energy Γ_c . Assuming a slip-weakening (cohesive) friction law with characteristic length d_c , the fracture energy is given by

$$\Gamma_c = \frac{1}{2} (\tau_u - \tau_f) d_c, \quad (2.6)$$

and corresponds to the green area in the cohesive model shown in Figure 2.4. Note that the energy below τ_f is not part of the fracture energy because the work done against friction was already taken into account through W_f . As an alternative, one could include the friction work into the fracture energy but would need to reduce the available energy and Equation (2.5) would change to $-dU = \Gamma(\tau_0) da$.

Energy concepts from fracture mechanics were also used by Freund (1979) to study the energy flux to the tip of a dynamic shear crack. For the general case¹, the crack tip of an in-plane shear rupture propagating below the Rayleigh wave speed absorbs energy, which is used to break the interface bonds. However, if the crack propagates between the Rayleigh and the shear wave speeds, the tip was shown to radiate energy. This is physically not acceptable, which leads to the conclusion that an in-plane shear crack cannot propagate at this speed. Out-of-plane shear cracks do not present this energetic behavior and are therefore capable of propagating at speeds between the Rayleigh and the shear wave speed. In-plane shear ruptures propagating at super-shear speeds is, however, possible, as was first demonstrated with numerical simulations by Andrews (1976b). Fracture mechanics concepts are also valid for the description of such super-shear cracks and show that a sharp crack can propagate at $\sqrt{2}c_s$ and a cohesive zone crack at any speed between the shear and dilatational wave speeds (Freund, 1979; Broberg, 1989). More details about experimental observations and numerical simulations of super-shear ruptures are given in Sections 2.2.2 and 2.3.3, respectively.

So far, applying fracture mechanics approaches to the propagation of slip regions along frictional interfaces was mainly based on theoretical considerations. Only recently, experimental confirmation was provided by Svetlizky and Fineberg (2014) through the measurement of various strain fields around a dynamic slip front. Near-tip strain fields of the linear elastic fracture mechanics theory were shown to describe most strain components well around a sub-Rayleigh slip front.

2.2.2 Propagation of Slip Fronts

The propagation of slip or frictional shear cracks presents various phenomena. It can propagate as a crack-like or pulse-like rupture (see Figure 2.5), at sub-Rayleigh or super-shear (or intersonic) speeds, spontaneously arrest or reach the end of the interface, and propagate through an interface heterogeneity or around it.

¹In the general case the stress intensity factor is not equal to zero. For more details about the stress intensity factor see Section 3.3

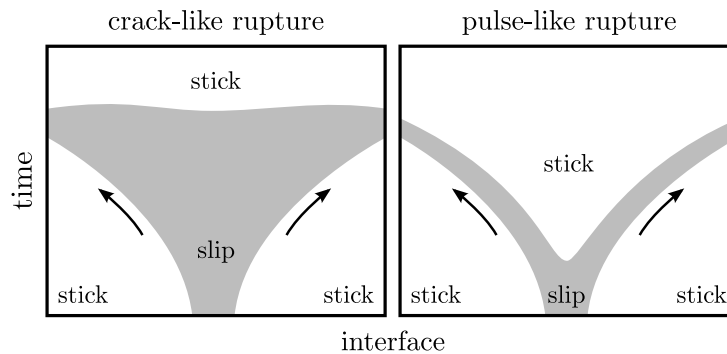


Figure 2.5: Illustration of crack-like and pulse-like interface ruptures. An initial crack at the center of the interface propagates (in the direction of the arrows) until reaching the edges. In a crack-like rupture, the area behind the propagating front is slipping until the crack does not extend anymore. A pulse-like rupture propagates with a closing tip behind the rupture front and the center region sticks already when the ruptures are still propagating.

For a long time, ruptures were generally thought of as crack-like, where slip occurs everywhere behind the rupture tip until propagation stops. An alternative rupture type was proposed by Heaton (1990) who discovered by studying ground motion data from earthquakes that the duration of slip at a given point of the interface is short compared to the overall duration of the earthquake. He suggested that one possible explanation is the propagation of a narrow self-healing slip pulse. This pulse-like type of rupture was also considered to be a possible cause to the absence of massive heat production at faults during earthquakes as observed by Lachenbruch and Sass (1980).

Experimentally, such pulse-like ruptures were observed along gel-glass interfaces (Baumberger et al., 2002, 2003), single-material homalite (Lykotrafitis et al., 2006) and poly(methyl-methacrylate) (PMMA) interfaces (Lu et al., 2007). Whether an interface rupture is of crack-like or pulse-like type was experimentally and numerically shown to depend systematically on the shear pre-stress (Lu et al., 2010). Lower shear loads lead to pulse-like propagation of slip zones and crack-like ruptures occur at higher shear pre-stress levels.

Another shear rupture type was discovered by Schallamach (1971) in his friction experiments with a rubber slider on a hard flat surface. He observed waves of detachment that propagate at high speed along the interface. These waves, which are often referred to as the Schallamach wave, seem to be produced by buckling due to tangential compressive stresses.

Further, Weertman (1980) showed that at bi-material interfaces, where the interface separates two solids of different materials, a special type of rupture can occur. If the interface is governed by Coulomb's friction law, dynamic changes in normal compressive stresses due to the system asymmetry lead to unstable slip and the propagation of a pulse-like rupture. This type of rupture cannot exist at single-material interfaces because the normal stress change does not occur. The existence of this self-sustained pulse at bi-material interfaces was experimentally

confirmed by Anooshehpour and Brune (1999) and Xia et al. (2005). Given that such systems are asymmetric, the propagation and its speed varies for different directions of propagation. In the experiments of Xia et al. (2005), ruptures propagating in the slip direction of the softer material always travel at the generalized Rayleigh wave speed, whereas in the opposite direction sub-shear or super-shear ruptures occur.

The propagation of super-shear ruptures was already earlier observed at bi-material interfaces. Lambros and Rosakis (1995) showed with impact experiments on PMMA-steel interfaces that cracks transitioning to intersonic speeds are shear dominated. This finding was also analytically confirmed (Liu et al., 1995).

As mentioned in Section 2.2.1, numerical and theoretical studies predicted that intersonic ruptures can also occur at homogeneous single-material interfaces. Experiments with interfaces between two thin homalite plates initiated by impact (Rosakis et al., 1999; Samudrala et al., 2002) or by exploding wire-triggering (Xia et al., 2004) presented evidences for intersonic ruptures at single-material interfaces. A wide variety of rupture speeds, including super-shear and so-called slow fronts, which propagate an order of magnitude slower than the shear wave speed, were also observed for slip fronts at a frictional interface between two PMMA blocks of different thickness (Rubinstein et al., 2004).

Slowly propagating fronts were also systematically observed by Nielsen et al. (2010) during the initial acceleration phase of spontaneously (without triggering) initiated slip fronts at an interface under combined shear and normal load. This quasi-static stable rupture later accelerates to sub-Rayleigh and intersonic speed. Other experiments showed that slow fronts occur where the shear to normal stress ratio is low at the interface (Ben-David et al., 2010). Fast ruptures, however, are related to relatively high shear stresses.

Most experiments considered so far consist of shear cracks or slip fronts propagating along an interface until they reach the edge. However, depending on the system and the loading, it is possible that a rupture naturally arrests beforehand. In friction experiments with a concentrated shear load located close to the interface, rupture arrests were observed for slip fronts that propagate before global sliding occurs (Rubinstein et al., 2007, 2008; Maegawa et al., 2010). The concentrated load facilitates initiation of slip before the entire system contains enough energy to support the propagation of the front to the end of the interface. A schematic illustration of arresting slip fronts as observed by Rubinstein et al. (2007) is shown in Figure 2.6.

The interfaces along which slip fronts propagate are usually not perfectly homogeneous. In many cases, heterogeneities exist for various reasons and affect the propagation of the front. When a rupture reaches an interface heterogeneity, three-dimensional effects play an important role. While a stronger region of the interface might resist longer against the rupture, the neighboring weak zones help the front to advance around it, which eventually leads to slip within the strong heterogeneity. Such effects have only very recently been studied in friction experiments showing that barriers can stop or delay the rupture propagation (Latour et al., 2013).

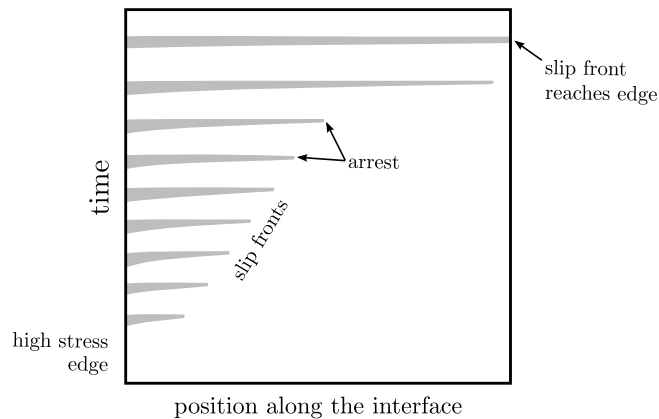


Figure 2.6: Schematic illustration of slip precursors as first observed by Rubinstein et al. (2007). A sequence of slip fronts initiate spontaneously at an edge with concentrated high stress level due to a closely located (shear) pusher. Each slip front propagates along the interface until it naturally arrests, usually at a position further than the arrest of the previous slip front. The number of slip fronts shown here is below the numbers seen in experiments in order to facilitate the reader's understanding.

2.2.3 Evolution of Local Frictional Strength

In the previous section, we reviewed the propagation of slip fronts at frictional interfaces and showed that the variety of different local friction phenomena is large. The origin of many of these observations is a weakening process that occurs at the interface. The local frictional strength and its weakening development is the result of smaller scale mechanisms, such as plowing of asperities or inter-atomic forces. For the present work, these aspects are out of scope and the evolution of the frictional strength is considered from a meso-scale point of view.

Experimentally, it is very challenging to capture the meso-scale evolution of the frictional strength at an interface. Most known results, presented in Section 2.1, show the macro-scale behavior of the friction force and it is far from obvious that these observations represent the actual evolution of the local strength. Some experimental evidence of the existence of local phenomena were given by Dieterich and Kilgore (1994) showing direct observations of the real contact area increasing with time. Such results can be used to get insights about local mechanisms but they do not provide detailed information about how the local frictional strength evolves. Furthermore, most friction experiments report on steady-state properties. For instance, the rate-dependence shown by Burwell and Rabinowicz (1953) describes the friction force for a given sliding speed at steady-state. Exceptions are the experiments by Dieterich (1979), which present the evolution of the frictional strength after an instantaneous change of the sliding speed. However, the applied slip rates are very low and probably considerably below the range of velocities occurring at the interface during the propagation of a dynamic slip front. The transitional behavior of frictional strength for various rock interfaces

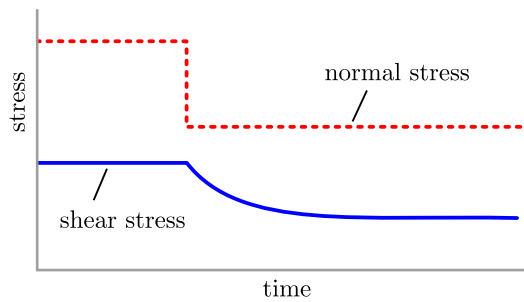


Figure 2.7: Schematic illustration of experimental observation by Prakash and Clifton (1993b). The friction force, measured as the shear stress, adapts over a characteristic time or slip distance to an instantaneous drop of the normal stress. This observation contradicts Coulomb's friction law, which imposes a sudden reaction of the friction force to an instantaneous change in the contact pressure.

was experimentally observed by Goldsby and Tullis (2011) for slip rates up to 0.4 m/s. However, as mentioned before, all these experiments study the macroscopic frictional strength which can only be taken as indicative information about the evolution of the local frictional strength.

Given that the experimental observation of local meso-scale frictional strength is challenging, different approaches can provide information about the mechanics of the interface. For instance, various analytical studies demonstrated that it is not very likely that meso-scale friction is governed by Coulomb's friction law. It was shown for deformable-rigid (Renardy, 1992; Martins et al., 1995) and deformable-deformable (Adams, 1995; Martins and Simões, 1995; Ranjith and Rice, 2001) interfaces between solids of different material properties that Coulomb's friction law is ill-posed under certain conditions. If these are satisfied, a nominally steady-state solution becomes dynamically unstable and self-excited motion occurs.

Experimental indication for non-Coulomb friction was found in plate impact experiments (Prakash and Clifton, 1993a,b; Prakash, 1998). The impact of two plates causes a shock wave, which modifies the contact pressure at the interface. The response of the frictional strength to a sudden change of the contact pressure is then determined by measuring the shear traction of the interface. These experiments showed that there is no instantaneous response of the frictional strength but a characteristic slip distance over which it adapts to the new contact pressure. A schematic illustration of a typical observation by Prakash and Clifton (1993b) is shown in Figure 2.7. Other friction experiments confirmed that the shear strength does not immediately increase for an increased normal stress (Kilgore et al., 2012).

On one hand, analytical (Ranjith and Rice, 2001) and numerical (Cochard and Rice, 2000) studies suggest that the problem of the ill-posedness of Coulomb's friction at bi-material interface can be solved by introducing a regularizing effect to the frictional strength with respect to the contact pressure. On the other hand, analytical (Adda-Bedia and Ben Amar, 2003) and numerical (Ben-Zion and Huang, 2002) studies showed that dynamically unstable phenomena do still occur with regularization, but later.

2.3 Numerical Models of Frictional Slip

Numerical models for the propagation of slip fronts at frictional interfaces are a powerful tool to support experimental and theoretical work on friction. This section provides an overview of the state of the art of numerical modeling of friction. It describes the different numerical methods used for the simulation of frictional slip and presents some applications to various problems with emphasis on the simulation of slip fronts at different propagation speeds, arresting naturally, and propagating through interface heterogeneities.

2.3.1 Numerical Methods

Various numerical methods have been applied to the simulation of frictional slip. A short review of these methods is here provided.

The simplest method is the spring-mass method, which consists of a number of blocks of given mass connected by springs (Burrige and Knopoff, 1967; Braun et al., 2009). The motion of the blocks is governed by Newton's second law of motion, which states that the force on an object is equal to the acceleration times the mass of the object. These models are often one-dimensional and sometimes two-dimensional. Friction occurs at an interface formed by the masses and a rigid flat plane, and is governed either by a local phenomenological friction law (Carlson and Langer, 1989) or by a group of springs representing contact asperities (Braun et al., 2009). The advantage of such models is simplicity and low computational cost. However, the discrete system of masses and springs does not correctly represent the continuum nature of solids.

Molecular dynamics is another discrete approach to numerical modeling of various physical phenomena (Griebel et al., 2007). It describes the motion of single atoms by Newton's second law and the interactions between particles by an inter-atomic potential. Molecular dynamics simulations have been used, for instance, to simulate the propagation of frictional shear cracks (Abraham and Gao, 2000) or the evolution of small-scale surface roughness under shear loads (Spijker et al., 2011). The frictional interactions in such simulations are the natural result of inter-atomic reactions. This method is an important tool to study friction at an atomistic scale and to cast light on the underlying mechanisms. However, limited by current computational resources, only simulations of tiny systems (~ 100 nm) are feasible.

A well-suited approach for interface problems is the spectral boundary integral method (Perrin et al., 1995; Geubelle and Rice, 1995). It solves the spectral formulation of the elastodynamic equation. The contribution of slip history to interface tractions is included by a convolution operation in Fourier space. In addition, a local friction law governs the interface and incorporates its efforts to the elastodynamic equation. The advantages of this method are the continuum approach to model solids, and the need of only discretizing the interface.² As no discretization of the surrounding solids is needed, finer meshes and more accurate solutions

²Even though discretization is needed for solving numerically, the method is still continuum based.

are possible. Boundary element methods are, however, mainly used for problems with infinite interfaces between two semi-infinite linear elastic solids. More complex systems with material non-linearities and solids of finite size require more advanced techniques which mitigate or eliminate the advantages of surface discretization.

Numerical methods that discretize entire solids include the finite-difference method (Thomas, 1995), the finite-element method (Zienkiewicz and Taylor, 2000) and the spectral-element method (Patera, 1984). These approaches are widely used for simulations of continuum mechanics in general, but, if extended, also for modeling the propagation of (shear) cracks and frictional slip. The finite-difference method uses a finite-difference equation, which is based on a Taylor series expansion, to solve differential equations. The finite-element method, which is described in more details in Section 3.4, is a variational approximation method that solves boundary value problems for differential equations. The spectral-element method is a particular version of the finite-element method, which uses high-order polynomial basis functions. All three methods as well as the spectral boundary integral method require additional tools to treat the discontinuity at the interface. A cohesive zone approach (Barenblatt, 1959; Ida, 1972) is generally adopted and applied within a traction-at-split-node technique (Andrews, 1973, 1999). The cohesive zone approach assumes a finite zone around the tip in which cohesive forces act across the interface. The traction-at-split-node method, which is described in more details in Section 3.5, concentrates these forces to the discretization points (*i.e.* nodes of the mesh).

The advantages of the finite-difference, finite-element and spectral-element methods lie in the continuum approach, the flexibility to model any constitutive behavior of the solids and the accuracy of information in the entire domain. The disadvantage, however, is the relatively high computational cost, which often requires high-performance computations (*i.e.* parallel simulations).

The comparison of simulation results from different numerical methods for a given test problem has shown that the solutions of the finite-difference method and the spectral boundary integral method are almost indistinguishable (Day et al., 2005). A similar comparison came to the same conclusion for solutions of the spectral-element method and the spectral boundary integral method (Kaneko et al., 2008)

2.3.2 Simulations of Frictional Slip Problems

Simulations of systems with frictional interfaces have been applied to various problems. Early numerical work was focused on ideal systems to study the basics of the mechanics of interface ruptures. An example of three-dimensional slip front simulations is the work by Day (1982a) who modeled the dynamic propagation of a rupture at fixed velocity along a rectangular interface.

Another problem studied intensively with numerical simulations is the unstable propagation

of slip pulses at bi-material interfaces. The dynamic reduction of the normal stress across the interface results in a continuous sharpening of the slip front leading to self-sustaining pulses and mesh convergence issues (Andrews and Ben-Zion, 1997; Harris and Day, 1997; Cochard and Rice, 2000; Ben-Zion and Huang, 2002; Shi and Ben-Zion, 2006). Additional effects, such as three-dimensional ruptures combining in-plane and anti-plane failure (Brietzke et al., 2007), the influence of the material mismatch on the propagation speed (Xu and Needleman, 1995), and interface roughness (Di Bartolomeo et al., 2010), have been studied for ruptures at bi-material interfaces.

The simulation of mechanisms occurring at tectonic faults is a promising path to a better understanding of earthquakes. For instance, numerical models of rate- and state-dependent faults with unstable zones surrounded by stable regions were shown to reveal an earthquake-like cycle with episodic spontaneous ruptures occurring under slow loading over long duration (Rice, 1993; Ben-Zion and Rice, 1997; Lapusta et al., 2000). Other simulations illustrated how the material contrast as well as off-fault plasticity affect the fault branching behavior of earthquakes (DeDontney et al., 2011, 2012). Numerical models can also provide insights about how to interpret ground motion caused by an earthquake in order to determine whether an interface heterogeneity is a strong area or a highly pre-stressed zone (Page et al., 2005).

2.3.3 Propagation Speed of Slip Fronts

When slip fronts spread on an interface, they present various propagation speeds. From a theoretical point of view, it had long been assumed that shear cracks cannot propagate faster than the shear wave speed at single-material interfaces. It was finite-difference simulations by Andrews (1976b) that demonstrated that shear ruptures can transition from sub-Rayleigh to super-shear speeds.³ Theoretical (Burridge et al., 1979) and experimental (Rosakis et al., 1999; Xia et al., 2004) confirmation followed years later. The transition was shown to occur through the creation of a small crack (often called “daughter crack”) ahead of the main crack.

The discovery of the sub-Rayleigh to super-shear transition of shear cracks incited a large number of numerical studies. Needleman (1999) used the finite-element method to confirm the findings of Andrews (1976b) and to reproduce numerically the experimental observations of Rosakis et al. (1999). By using a different cohesive characterization of the interface than Andrews (1976b) and obtaining comparable results, he showed that the existence of the transition to super-shear rupture is independent of the cohesive law. The daughter-crack mechanism also exists at the atomic-scale, as was observed by Abraham and Gao (2000) in molecular dynamics simulations. Numerical studies at the continuum scale using the spectral boundary integral method analyzed systematically the influence of the external loading (Geubelle and Kubair, 2001), a favorable heterogeneity (Liu and Lapusta, 2008) and the nucleation procedure (Lu et al., 2009). The transition to super-shear rupture was also

³In fact, Burridge (1973) showed for the special case of a self-similar shear crack with friction but without cohesion that the dilatational wave speed is a possible rupture speed. However, according to his theory, the crack cannot propagate at any other speed between the shear and the dilatational wave speed.

observed to occur as a three-dimensional effect of interface heterogeneities (Fukuyama and Olsen, 2002; Dunham et al., 2003).

More recently, slow fronts (Rubinstein et al., 2004; Nielsen et al., 2010), a new aspect of rupture propagation, draw the attention of the numerical research community. Reproducing with simulations such slow propagation was found to be challenging. One successful approach consists of friction models that exhibit a velocity-weakening-strengthening behavior (Bouchbinder et al., 2011; Bar Sinai et al., 2012). Rupture velocities ranging from slow up to super-shear are also observed for spring-mass models with friction characteristics based on asperity-type considerations using interface springs (Braun et al., 2009; Trømborg et al., 2014). Another possibility for slow fronts was shown to be stress concentrations at a rate- and state-dependent frictional interface (Kaneko and Ampuero, 2011).

2.3.4 Precursors – the Arrest of Slip Fronts

Slip fronts that propagate along frictional interfaces may never stop and reach the edge, or may arrest naturally at a point on their paths. The arrest of slip fronts has in the past attracted only limited attention because of lacking experimental observation. An exception is Ampuero et al. (2006) who used fracture mechanics arguments to determine rupture arrest and to analyze the connection between statistical properties at the interface and the macroscopic behavior of earthquakes.

Most numerical interest arose from the experimental observation of slip precursors by Rubinstein et al. (2007). In these friction experiments with a pusher located closely to the interface, slip fronts initiate well before global sliding, propagate over parts of the interface and stopped naturally. The length of these slip precursors increases continuously and follows systematically (for several experiments) the same load-length relation. Using one-dimensional (Maegawa et al., 2010; Amundsen et al., 2012) and two-dimensional (Trømborg et al., 2011) spring-mass models, this behavior was qualitatively reproduced and shown to be (in a certain range) independent of the slider and pusher geometry.

2.3.5 Slip Front Propagation through Interface Heterogeneities

For simplicity, propagation of interface ruptures is often studied at homogeneously loaded interfaces with homogeneous frictional strength. Real interfaces, however, are rarely homogeneous. Heterogeneities are present in the loading and in the strength. Causes include, for instance, the finite size of the system, varying material or interface properties.

Nevertheless, some numerical studies considered interface heterogeneities. Das and Aki (1977) showed with two-dimensional simulations that shear cracks can overcome barriers, which are zones of higher strength. The results of three-dimensional simulations demonstrated that, under certain conditions, such barriers can lead to a transition from sub-Rayleigh to super-shear ruptures (Dunham et al., 2003). A different type of interface heterogeneities is a zone of

Chapter 2. State of the Art

higher (shear) pre-stress, which makes the propagation of the rupture energetically favorable. An abrupt (positive) jump in rupture speed for fronts reaching an increased pre-stress region was observed by Day (1982b) in three-dimensional finite-difference simulations. Similar to barriers, these zones cause the rupture to transition to super-shear (Fukuyama and Olsen, 2002; Liu and Lapusta, 2008).

3 Theoretical and Numerical Framework

The research presented in this thesis relies on several theoretical and numerical concepts of the mechanics of continua. This chapter describes basic theory of continuum solid mechanics, mechanics of contact and friction, and linear elastic fracture mechanics. It also provides a fundamental description of the finite-element method and the traction-at-split-node method.

3.1 Continuum Solid Mechanics

Continuum solid mechanics describes the deformation and the stress that a solid – a volume of a given mass – experiences under a given set of boundary conditions. Basic elements of continuum mechanics include the following definitions and equations:

- **kinematic** equations, which describe the deformation of the continua,
- **stress** measures, which define the concept of internal stresses,
- equations of **conservation**, which are the fundamental laws of physics, and
- **constitutive** equations, which describe the material properties.

Considering that continuum mechanics is a well-known subject, this section is kept to a strict minimum and readers are, for more information, referred to the following textbooks: Bower (2009); Holzapfel (2000).

3.1.1 Kinematic Equations

The motion of a continuum body is described by the position of its material points over time. An initial and undeformed configuration of a body at time $t_0 = 0$ occupying the domain denoted Ω_0 is considered as the *reference configuration*. At $t > t_0$, the deformed body occupies in the *current configuration* the domain Ω . These two configurations are illustrated in Figure 3.1.

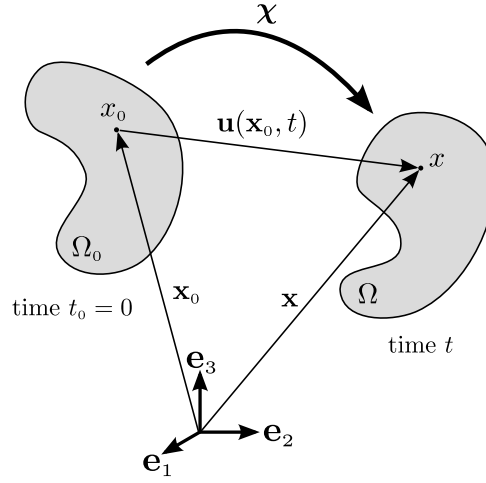


Figure 3.1: Lagrangian description of a continuum body shown with the initial (reference) configuration Ω_0 as well as the deformed (current) configuration Ω .

Assuming a one-to-one correspondence between a material point x_0 in reference configuration and x in current configuration, the motion of this material point is described by

$$\mathbf{x} = \chi(\mathbf{x}_0, t) \quad \forall \mathbf{x}_0 \in \Omega_0, \quad (3.1)$$

where \mathbf{x}_0 and \mathbf{x} are the positions of x_0 and x , respectively, and χ is the mapping corresponding to the motion. In Lagrangian (material) description, the motion and all other related quantities are expressed with respect to the so-called material coordinate \mathbf{x}_0 . In Lagrangian form, the displacement field

$$\mathbf{u}(\mathbf{x}_0, t) = \mathbf{x} - \mathbf{x}_0 = \chi(\mathbf{x}_0, t) - \mathbf{x}_0 \quad \mathbf{x}_0 \in \Omega_0, \quad (3.2)$$

relates the current position \mathbf{x} with the referential position \mathbf{x}_0 , as also shown in Figure 3.1. The displacement gradient tensor is defined as

$$\mathbf{H} = \nabla_0 \mathbf{u}, \quad (3.3)$$

where ∇_0 is the gradient operator with respect to the material coordinate \mathbf{x}_0 . The deformation gradient is defined as

$$\mathbf{F} = \nabla_0 \mathbf{x} = \frac{\partial \chi(\mathbf{x}_0, t)}{\partial \mathbf{x}_0} \quad \forall \mathbf{x}_0 \in \Omega_0. \quad (3.4)$$

Based on these definitions, the deformation gradient is related to the displacement gradient tensor by $\mathbf{F} = \mathbf{I} + \mathbf{H}$, where \mathbf{I} is the identity matrix. The Jacobian of the deformation gradient is defined by

$$J(\mathbf{x}_0, t) = \det \mathbf{F}(\mathbf{x}_0, t). \quad (3.5)$$

The Jacobian is a measure of the volume change produced by the deformation from the reference to the current configuration and can be written as $dV = J dV_0$. Physically admissible displacement fields \mathbf{u} impose therefore that $J > 0$.

The Green-Lagrange strain tensor can be computed by

$$\mathbf{E} = \frac{1}{2} (\mathbf{F}^T \cdot \mathbf{F} - \mathbf{I}) = \frac{1}{2} (\mathbf{H}^T + \mathbf{H} + \mathbf{H}^T \mathbf{H}) . \quad (3.6)$$

The infinitesimal strain tensor is a linear approximation of the Green-Lagrange strain tensor and is defined as

$$\boldsymbol{\varepsilon} = \frac{1}{2} (\mathbf{H}^T + \mathbf{H}) . \quad (3.7)$$

This approximation is only valid for small shape changes of the body.

The kinematic equations, as given for instance by Equation (3.3) and (3.7), describe the deformation of the continua as a function of the displacement of the material points.

3.1.2 Stress Measure

Considering a boundary traction vector $\bar{\mathbf{t}}$ and an outwards-pointing boundary normal vector \mathbf{n} , the First Piola-Kirchhoff stress tensor \mathbf{P} is defined as

$$\bar{\mathbf{t}} = \mathbf{P} \mathbf{n} , \quad (3.8)$$

where the function parameters (\mathbf{x}_0, t) are omitted for clarity. The definition of \mathbf{P} describes the stress occurring in the current configuration with respect to the reference configuration. It is therefore also called the nominal stress.

Another well-known stress measure is the Cauchy stress tensor $\boldsymbol{\sigma}$, which describes the stress in the current configuration with respect to the current configuration. Describing the same stress state, the two measures are related by

$$\mathbf{P} = J \boldsymbol{\sigma} \mathbf{F}^{-T} . \quad (3.9)$$

3.1.3 Conservation Equations / Balance Principle

The balance of linear momentum in terms of nominal stress results in the equation of motion

$$\nabla_0 \cdot \mathbf{P} + \rho_0 \mathbf{b} = \rho_0 \ddot{\mathbf{u}} \quad \forall \mathbf{x}_0 \in \Omega_0 , \quad (3.10)$$

where ρ_0 is the density, \mathbf{b} is a body force, and $\ddot{\mathbf{u}}$ is the material acceleration. The function parameters (\mathbf{x}_0, t) were omitted for better readability.

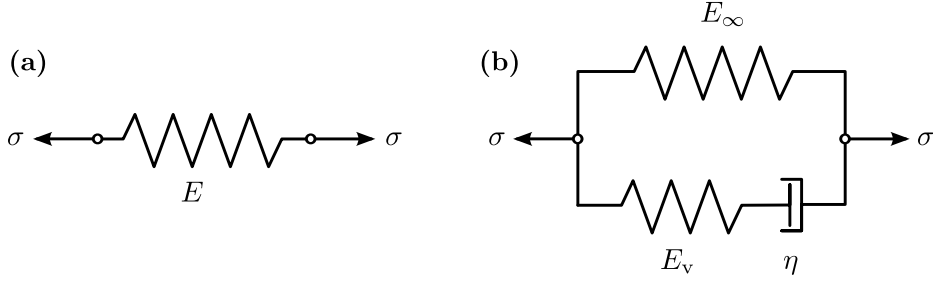


Figure 3.2: One-dimensional representation of constitutive material laws for (a) linear elasticity, and (b) viscoelasticity modeled by the standard linear solid model.

The balance of angular momentum causes the Cauchy stress tensor to be symmetric $\boldsymbol{\sigma} = \boldsymbol{\sigma}^T$. The first Piola-Kirchhoff stress tensor, however, is in general not symmetric: $\mathbf{P}\mathbf{F}^T = \mathbf{F}\mathbf{P}^T$ as deduced from Equation (3.9).

3.1.4 Constitutive Material Laws

The constitutive laws describe the material properties and provide an equation that links the stress tensor with the strain tensor. The two constitutive laws applied in this work are linear elasticity and a basic law of viscoelasticity, the standard linear solid model. A one-dimensional representation of both laws is shown in Figure 3.2.

Linear Elasticity

Linear elasticity provides a linear stress-strain relation and corresponds, in one dimension, to a simple spring described by $\sigma = E\varepsilon$, see Figure 3.5(a). For a continuum solid, the constitutive equation becomes:

$$\boldsymbol{\sigma} = \frac{E}{1+\nu} \left(\boldsymbol{\varepsilon} + \frac{\nu}{1-2\nu} \text{Tr } \boldsymbol{\varepsilon} \mathbf{I} \right), \quad (3.11)$$

where E is the Young's modulus and ν the Poisson's ratio.

An alternative form of Equation (3.11) uses the Lamé parameters, which results in

$$\boldsymbol{\sigma} = \lambda \text{Tr } \boldsymbol{\varepsilon} \mathbf{I} + 2G\boldsymbol{\varepsilon}, \quad (3.12)$$

with Lamé's first parameter λ and the shear modulus G . The Lamé parameters as well as the bulk modulus K are related to the Young's modulus and the Poisson's ratio through

$$\lambda = \frac{\nu E}{(1+\nu)(1-2\nu)} \quad G = \frac{E}{2(1+\nu)} \quad K = \frac{E}{3(1-2\nu)}. \quad (3.13)$$

In two-dimensional systems, the stress-strain relation can be approximated by the plane-strain or plane-stress assumptions. In both cases, $\boldsymbol{\sigma}$ and $\boldsymbol{\varepsilon}$ are 2×2 tensors.

The plane-strain approximation imposes the out-of-plane strain to be zero (as if the solid was infinite in this direction) and the out-of-plane stress component is given by $\sigma_z = \nu(\sigma_x + \sigma_y)$. The stress-strain relation is valid as given for the three-dimensional problem.

The plane-stress approximation assumes zero stress in the out-of-plane direction (as if the solid was infinitely thin) and the out-of-plane strain component is given by $\varepsilon_z = -\nu(\sigma_x + \sigma_y)/E$. The stress-strain relation is given by Equation (3.12) with modified Lamé parameters. In plane-stress approximation, Equations (3.13) are adapted to

$$\lambda = \frac{\nu E}{1 - \nu^2} \quad G = \frac{E}{2(1 + \nu)} \quad K = \frac{E(1 + 2\nu)}{3(1 - \nu^2)}. \quad (3.14)$$

Note that the shear modulus is the same in plane-stress as in plane-strain approximation.

The propagation speed of longitudinal waves in a continuum is

$$c_d = \sqrt{\frac{\lambda + 2G}{\rho}} \quad (3.15)$$

with λ and G given by Equation (3.13) or (3.14) depending on the type of the problem, and ρ the density of the material. The shear waves propagate at

$$c_s = \sqrt{\frac{G}{\rho}}. \quad (3.16)$$

The Rayleigh wave, which is a surface wave of great importance for the mechanics of interface ruptures, has a propagation speed of approximately

$$c_r = \frac{0.862 + 1.14 \nu}{1 + \nu} c_s, \quad (3.17)$$

and is slightly slower than the shear wave speed (Achenbach, 1973).

Standard Linear Solid

Viscoelasticity can be described by a variety of constitutive laws. The standard linear solid model chosen here, is particularly suitable for modeling polymers. The provided description is largely build on Chapter 10 of Simo and Hughes (1998). The starting point is an alternative expression of Equation (3.11), which is split into a spherical and a deviatoric part

$$\boldsymbol{\sigma} = K \text{Tr } \boldsymbol{\varepsilon} \mathbf{I} + 2G \left(\boldsymbol{\varepsilon} - \frac{1}{3} \text{Tr } \boldsymbol{\varepsilon} \mathbf{I} \right). \quad (3.18)$$

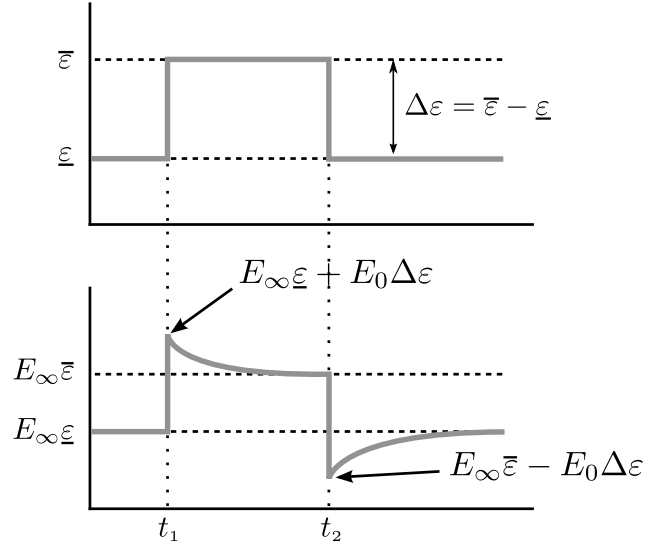


Figure 3.3: Schematic illustration of the viscoelastic response in stress to a rectangular change in strain of $\Delta\varepsilon = \bar{\varepsilon} - \varepsilon$. Initially, the system is assumed to be in equilibrium, and the time between the strain steps t_1 and t_2 is considerably longer than the relaxation time of the viscoelastic properties.

As shown in Figure 3.2(b), the standard linear solid model adds parallel to the linear elasticity spring an element containing another spring and a dashpot. A polymer is best modeled if this viscous element applies only to the deviatoric part of the stress-strain relation. The Cauchy stress tensor of a deviatoric standard linear solid model is, therefore, given by

$$\boldsymbol{\sigma}(t) = K_\infty \text{Tr } \boldsymbol{\varepsilon} \mathbf{I} + \int_{-\infty}^t 2G(t-s) \left(\dot{\boldsymbol{\varepsilon}} - \frac{1}{3} \text{Tr } \dot{\boldsymbol{\varepsilon}} \mathbf{I} \right) ds, \quad (3.19)$$

where $\dot{\boldsymbol{\varepsilon}}$ is the strain rate tensor and the shear modulus evolves over time according to $G(t) = G_\infty + G_v \exp(-t/t_v)$. The shear modulus is composed of the static G_∞ and viscous G_v shear moduli. The characteristic relaxation time $t_v = \eta/E_v$ depends on the material viscosity η and the viscous Young's modulus E_v . The static bulk modulus K_∞ is given by Equation (3.13) or (3.14) for $E = E_\infty$. The shear moduli can be computed by Equation (3.13) using the static E_∞ and viscous E_v Young's modulus, respectively.

An illustration of the behavior of the standard linear solid model is shown in Figure 3.3 for a one-dimensional problem with instantaneous Young's modulus $E_0 = E_\infty + E_v$. A solid, which is initially in equilibrium at $\sigma = E_\infty \varepsilon$, is subjected to a rectangular strain change of amplitude $\Delta\varepsilon = \bar{\varepsilon} - \varepsilon$. The instantaneous response of the stress to the first strain step at t_1 is

$$\sigma(t_1^+) = E_\infty \bar{\varepsilon} + E_0 \Delta\varepsilon = E_\infty \bar{\varepsilon} + E_v \Delta\varepsilon.$$

The stress then evolves over time with an exponential decrease from the instantaneous re-

sponse to the new equilibrium state $\sigma = E_\infty \bar{\varepsilon}$ following

$$\sigma(t) = E_\infty \bar{\varepsilon} + E_v \exp\left(-\frac{t-t_1}{t_v}\right) \Delta\varepsilon \quad \forall t_1 < t < t_2,$$

where t_v is the characteristic relaxation time of the viscosity. For time periods considerably longer than the relaxation time, the stress reaches the new equilibrium $\sigma(t \gg t_1 + t_v) = E_\infty \bar{\varepsilon}$, and if $t_2 - t_1 \gg t_v$, it does so before the second strain change at t_2 . The stress evolution due to this second strain step is the same but with an opposite sign.

The elastic wave speeds for viscoelastic materials are given by Equations (3.15), (3.16) and (3.17) with $\lambda = \lambda_\infty + \lambda_v$ and $G = G_\infty + G_v$.

3.2 Fundamentals of Contact Mechanics with Friction

The theoretical basis of contact mechanics with friction are well-established and documented. Here, we only provide a short summary of the contact conditions, the friction conditions, and some basic friction laws. For a more detailed description of contact mechanics with friction, the reader is referred to Kikuchi and Oden (1988); Wriggers (2006); Curnier (2007). The contact and friction description given here is similar to the approach of Ampuero (2002).

The contact interface of two solids is defined by the two possibly contacting boundaries S_0^{c1} and S_0^{c2} . Considering a point x_0 on S_0^{c1} with its pair-point \tilde{x}_0 on S_0^{c2} , we can define the gap as the vector pointing from x_0 to \tilde{x}_0 :

$$\mathbf{g}(\mathbf{x}_0, t) = \mathbf{u}(\tilde{\mathbf{x}}_0, t) - \mathbf{u}(\mathbf{x}_0, t) + \mathbf{g}_0(\mathbf{x}_0), \quad (3.20)$$

with initial gap $\mathbf{g}_0(\mathbf{x}_0) = \tilde{\mathbf{x}}_0(\mathbf{x}_0) - \mathbf{x}_0$. For simplicity, we here assume that the association of a pair-point \tilde{x}_0 to x_0 is unique and its position is a function of the position of x_0 . In most cases, however, a unique mapping of contacting nodes is not possible and more advanced methods need to be applied. More details on this popular problem of computational contact mechanics is given in Yastrebov (2013).

The gap can be decomposed into the normal and tangential part with respect to the boundary S_0^{c1} as

$$\mathbf{g} = g_N \mathbf{n} + \mathbf{g}_T, \quad (3.21)$$

where \mathbf{n} is the outward-pointing surface normal on S_0^{c1} , g_N is the length of the normal gap, and \mathbf{g}_T is the tangential gap. With this decomposition it is possible to handle contact and friction conditions independently, except if the friction condition is governed by a friction law coupling the friction traction with the contact pressure.

The contact of two solids results in reactions at the interface. In the same way as the gap, these

interface reactions can be decomposed into the normal and tangential part:

$$\mathbf{r} = r_N \mathbf{n} + \mathbf{r}_T, \quad (3.22)$$

where r_N is the contact pressure and \mathbf{r}_T is the friction traction (vector) of the interface. In later chapters of this thesis, the components of the interface reaction are denoted σ for the contact pressure and τ for the shear traction in order to emphasize the link to the stress state in the solids.

3.2.1 Contact Conditions

A basic condition of contact is impenetrability of the solids, which only allows the gap at the interface to be positive, if not in contact, and to be zero while in contact. This condition is enforced by the contact pressure acting on both boundaries with opposed sign (negative on the reference boundary S_0^{cl}). When there is no contact, the contact pressure is zero. The combination of these two conditions leads to the Hertz-Signorini-Moreau conditions:

$$g_N \geq 0 \quad (3.23)$$

$$r_N \leq 0 \quad (3.24)$$

$$g_N \times r_N = 0 \quad (3.25)$$

Such conditions basically describe two states. Either the solids are in contact, which results in non-zero contact pressure $r_N < 0$ but no gap $g_N = 0$, or the solids do not touch, which leads to an interface opening $g_N > 0$ but no contact pressure $r_N = 0$. A representation of these contact conditions is shown in Figure 3.4.

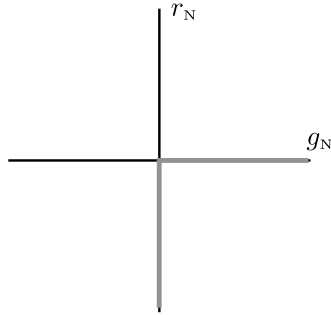


Figure 3.4: Representation of contact conditions. The normal contact reaction, also called contact pressure, is zero if there is a gap at the interface and is non-zero (negative) if the contact boundaries are in contact.

These conditions apply only to single points of the interface, which means that some parts of the interface can be in contact while other parts are detached.

3.2.2 Friction Conditions

In common language terms, we can describe friction at an interface as a resistance-type of force, which reacts to a load but does not exist without it. Using the same approach as for defining contact conditions, friction conditions can be described as

$$|\mathbf{r}_T| - r_F \leq 0 \quad (3.26)$$

$$|\dot{\mathbf{g}}_T| \times (|\mathbf{r}_T| - r_F) = 0, \quad (3.27)$$

where r_F is the frictional strength given by the constitutive friction law. The frictional strength is in later chapters also denoted as τ^s . The two states described by these conditions are: sticking and sliding. If the two boundaries are sticking to each other, there is no tangential gap rate $|\dot{\mathbf{g}}_T| = 0$ (also called slip rate) and the friction traction is smaller than the frictional strength: $|\mathbf{r}_T| - r_F < 0$. However, if the two boundaries are sliding over one another, the slip rate is non-zero $|\dot{\mathbf{g}}_T| > 0$ and the friction traction is exactly equal to the strength: $|\mathbf{r}_T| - r_F = 0$.

The friction conditions formulated in terms of the tangential gap rate $\dot{\mathbf{g}}_T$ instead of the tangential gap \mathbf{g}_T present the advantage of explicitly illustrating the possibility of a frictional stick-slip phenomenon. However, a formulation of the friction conditions in terms of \mathbf{g}_T is preferable regarding computational techniques. An equivalent form of the friction conditions (3.27) can be written as

$$|\mathbf{r}_T| - r_F \leq 0 \quad (3.28)$$

$$|\mathbf{g}_T^a| \times (|\mathbf{r}_T| - r_F) = 0, \quad (3.29)$$

using \mathbf{g}_T^a the tangential part of an adapted gap function, which is defined as

$$\mathbf{g}^a(\mathbf{x}_0, t) = \mathbf{g}(\mathbf{x}_0, t) - \mathbf{g}(\mathbf{x}_0, \hat{t}), \quad (3.30)$$

where \hat{t} is the last time the interface stuck. If the interface has never been stuck: $\mathbf{g}(\mathbf{x}_0, \hat{t}) = 0$. The adapted gap function behaves in the normal direction the same way as the original gap function because for any \hat{t} , we find $g_N^a(\mathbf{x}_0, \hat{t}) = 0$. In the tangential direction, \mathbf{g}^a is the relative tangential gap with respect to the last time the interface was sticking.

As for the contact conditions, the friction conditions apply only to single points of the interface, thus some parts of the interface can be sticking while other parts are sliding. However, the friction conditions are only valid if there is contact, *i.e.*, $g_N = 0$, and the frictional strength r_F is, by definition, zero if there is loss of contact.

3.2.3 Friction Laws

The frictional strength, which defines the upper limit of possible friction tractions, is given by a constitutive friction law. The variety of different friction laws is great and we here summarize only some basic friction laws that are applied in the presented simulations. The choice is

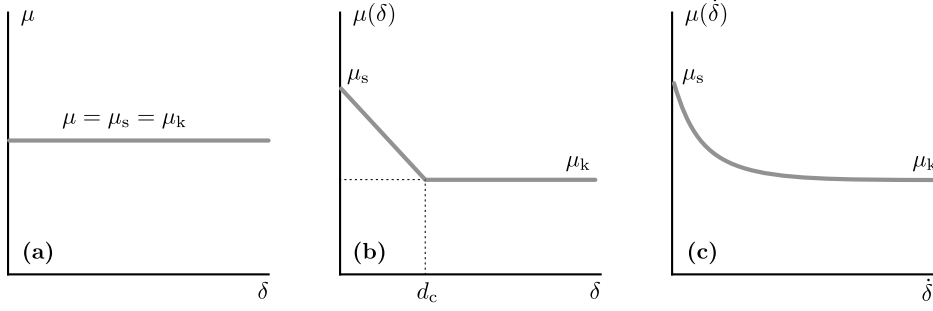


Figure 3.5: Representation of different friction laws: **(a)** Coulomb's friction, **(b)** linear slip-weakening friction, and **(c)** exponential rate-weakening friction.

largely based on simplicity because a simple friction law is often sufficient to model a particular friction phenomenon and has the advantage of having a limited number of parameters, the effects of which need to be studied.

Coulomb Friction

The Coulomb friction law, as introduced in Section 2.1, describes the frictional strength r_F at the scale of interface tractions by following Equation (2.1) as

$$r_F = \mu r_N, \quad (3.31)$$

where μ is the friction coefficient and r_N the contact pressure. Here, μ is a simplified way of describing an interface property and should not be mistaken for the apparent macroscopic friction coefficient.

Coulomb's friction law is often defined using a static μ_s and a kinetic μ_k friction coefficient, where $\mu_s > \mu_k$. However, this is not what is done here. The present Coulomb friction law, as shown in Figure 3.5(a), has a single friction coefficient valid for the static and kinetic state. Weakening processes, which are often observed, are integrated in other Coulomb-based friction laws described below.

Linear Slip-Weakening Friction

The weakening process of the frictional strength can be described as a function of the slip distance. One of the most basic friction laws is the linear slip-weakening law which integrates a slip-dependence into μ . The friction coefficient evolves, as shown in Figure 3.5(b), linearly from its static value μ_s to the kinetic value μ_k over the characteristic slip distance d_c , which can be written as

$$\mu(\delta) = \begin{cases} \mu_s - \frac{\delta}{d_c} (\mu_s - \mu_k) & \forall \delta < d_c \\ \mu_k & \forall \delta \geq d_c, \end{cases} \quad (3.32)$$

where δ is the local slip at the interface. It is a cumulative property that is defined as

$$\delta(t) = \int_{\hat{t}}^t |\dot{\mathbf{g}}_r(s)| \, ds \quad (3.33)$$

where \hat{t} is the time when this point last stuck. According to this definition, δ is always zero when no slip occurs. The interface presents, therefore, instantaneous healing. More advanced friction laws include healing features describing the strengthening process through a time-dependent process of the friction coefficient.

The presented friction law integrates the slip-weakening process into the local friction coefficient. The frictional strength, however, is still proportional to the contact pressure as given by Equation (3.31), which ensures that it is still a Coulomb-based friction law.

Exponential Rate-Weakening Friction

Another possibility of describing the transition of frictional strength from static to kinetic values are rate-weakening friction laws. One option is the exponential rate-weakening law as shown in Figure 3.5(c). This friction law is given by

$$\mu(\dot{\delta}) = \mu_k + (\mu_s - \mu_k) \exp\left(-\dot{\delta} \sqrt{(\mu_s - \mu_k) / \alpha}\right), \quad (3.34)$$

with slip rate $\dot{\delta} = |\dot{\mathbf{g}}_r|$ and transition parameter α . Similar to the linear slip-weakening law, the frictional strength is based on Coulomb and is given by Equation (3.31).

3.3 Basis of Linear Elastic Fracture Mechanics

Linear elastic fracture mechanics (LEFM) is today a well established theory, which is widely used in engineering design. Many extensions of LEFM for more advanced problems, such as fracture of elasto-plastic materials, exist and are still developed. In this section, we provide a short summary of the basics of LEFM, limited to the theory needed for this work. For a more detailed description, the reader is referred to the following textbooks: Anderson (2005); Freund (1990).

Fracture of a solid is the creation of an interface (or two surfaces) due to the loss of inter-atomic bonds. One can distinguish between three fundamental modes of fracture as shown in Figure 3.6. In Mode I, the opening of the interface is perpendicular to the interface. Mode II fracture is the propagation of a rupture within the plane of the shear load and the relative displacement. Out-of-plane loads lead to Mode III ruptures in which the propagation direction is perpendicular to the relative displacement. This fracture mode is sometimes also called anti-plane shear rupture.

In this work, we study the propagation of slip at frictional interfaces. Assuming an analogy

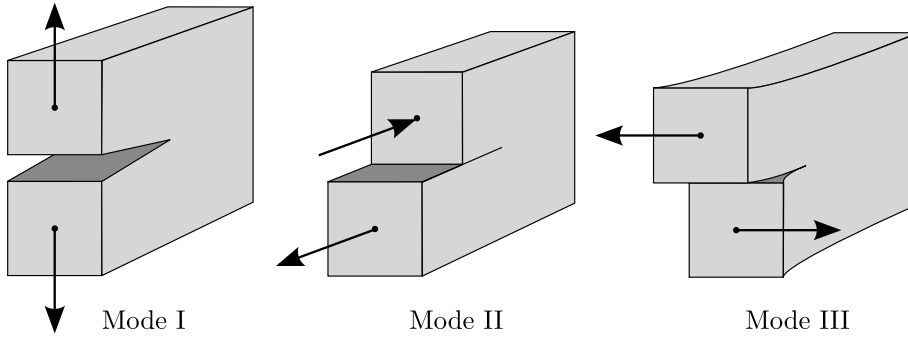


Figure 3.6: Three fundamental rupture modes are defined: Normal fracture (Mode I), in-plane shear fracture (Mode II), and out-of-plane shear fracture (Mode III).

between fracture and friction, we describe the propagation of slip regions as a combination of Mode II and III ruptures. In the special case of friction between two thin plates, the onset of sliding corresponds best to a Mode II fracture. Thus, we focus on the description of Mode II fracture. The presented theory, however, is valid for all three modes.

There are two basic approaches to the description of fracture mechanics of linear elastic solids. A global approach based on energy consideration leads to the definition of an energy release rate and its critical value in order to determine whether a crack undergoes stable or unstable growth. The second approach is based on the description of the local stress field surrounding a crack. A stress intensity factor is defined and provides a measure of the crack stability. Both approaches are equivalent and the different interface properties are uniquely related.

Griffith (1920) proposed that, under equilibrium conditions, the energy balance for an incremental crack area dA is

$$\frac{d\Pi}{dA} + \frac{dW_s}{dA} = 0, \quad (3.35)$$

with Π the potential energy of the solid (strain energy and energy from external forces), and W_s the work required to create a new interface. The total energy in the system is $\Pi + W_s$. The work used to create a new interface is equal to the work required to create two new surfaces.

Irwin (1956) introduced the energy release rate Γ which is a measure of the energy available for an increment of a crack and is defined as

$$\Gamma = -\frac{d\Pi}{dA}. \quad (3.36)$$

Based on the energy balance, Equation (3.35), a critical energy release rate Γ_c can be defined

as

$$\Gamma_c = \frac{dW_s}{dA}, \quad (3.37)$$

which binds the potential energy made available by the energy release rate. Therefore, crack extension occurs when the energy release rate reaches its critical value.

Once the critical energy release rate is achieved, the crack can either grow under stable or unstable conditions. Whether a crack grows dynamically or quasi-statically can be determined with the driving force curve and the resistance curve. Considering a two-dimensional problem with an initial crack of length a_0 , the driving force curve $\Gamma(a)$ is the energy release rate as a function of the crack extension a . The resistance curve $R(a)$ is the energy needed to increase the interface depending on the length of the crack. If the surface energy is independent of the crack length, the resistance curve is equal to the critical energy release rate: $R(a) = \Gamma_c$. However, if the surface energy changes for an increasing crack, the critical energy release rate is often used to define the initiation of crack growth independently of whether stable or unstable. It can therefore be stated as $R(a_0) = \Gamma_c$.

Using the driving force curve and the resistance curve, the stability condition of crack growth can be formulated in the following way. Stable crack growth occurs if

$$\Gamma = R \quad \text{and} \quad \frac{d\Gamma}{da} \leq \frac{dR}{da}, \quad (3.38)$$

with the incremental crack length da , which is related to the incremental crack area dA through the width of the interface. Stable crack growth appears when the driving force curve goes below the resistance curve for an increasing crack length. If Γ stays above R the crack growth will be unstable. This condition can be expressed as

$$\Gamma = R \quad \text{and} \quad \frac{d\Gamma}{da} > \frac{dR}{da}. \quad (3.39)$$

Under these conditions, the available energy for crack growth is higher than the energy dissipated through the fracturing of the solid. No equilibrium solution exists and the crack propagates dynamically.

Another approach to the description of fracture mechanics is at the local level by expressing the stress field surrounding a crack tip. A closed form exists for isotropic linear elastic materials under certain crack configuration. The stress tensor is, in polar coordinates r and θ , of the following form:

$$\sigma_{ij} = \frac{K}{\sqrt{2\pi r}} f_{ij}(\theta) + \sum_{m=0}^{\infty} A_m r^{m/2} g_{ij}^{(m)}(\theta), \quad (3.40)$$

with K the stress intensity factor and f_{ij} a dimensionless function of θ . Higher-order terms contribute through the amplitude A_m and the dimensionless function $g_{ij}^{(m)}$ for the m -th term.

Higher-order terms are, in linear elastic materials, negligible close to the crack tip. Thus, one can write for Mode II:

$$\lim_{r \rightarrow 0} \sigma_{ij}^{(II)} = \frac{K_{II}}{\sqrt{2\pi r}} f_{ij}^{(II)}(\theta) . \quad (3.41)$$

At the interface of Mode II cracks ($\theta = 0$), the dimensionless functions take the values

$$f_{xx}^{(II)} = 0 \quad f_{yy}^{(II)} = 0 \quad f_{xy}^{(II)} = 1 , \quad (3.42)$$

which leads to the following stress fields in the $1/\sqrt{r}$ singularity-dominated zone:

$$\sigma_{xx} = 0 \quad \sigma_{yy} = 0 \quad \tau_{xy} = \frac{K_{II}}{\sqrt{2\pi r}} . \quad (3.43)$$

Outside this area, the higher-order terms in Equation (3.40) are not negligible and the stresses are the result of the remote boundary conditions (*i.e.* depend on the system set-up).

For linear elastic materials, the principle of superposition is valid for stress intensity factors of the same mode. Independently determined stress intensity factors for load configurations A and B can be summed together for the stress intensity factor of the combined load configuration: $K_{II}^{(A+B)} = K_{II}^{(A)} + K_{II}^{(B)}$. The superposition principle, however, is not valid for stress intensity factors of different modes: $K \neq K_I + K_{II}$.

The two presented descriptions of fracture are closely related. The connection between the global approach, the energy release rate, and the local description, the stress intensity factor, was demonstrated by Irwin (1957). He showed that for any given crack, one can write

$$\Gamma = \frac{K^2}{\hat{E}} \quad (3.44)$$

with $\hat{E} = E$ for plane-stress and $\hat{E} = E/(1 - \nu^2)$ for plane-strain configurations.

3.4 The Finite-Element Method

The finite-element method is a variational approximation method that uses piecewise polynomial basis functions for the numerical solution of boundary value problems governed by partial differential equations. In continuum mechanics, the finite-element method is used to solve the equation of motion. Before developing the finite-element method, a summary of the complete boundary value problem, as introduced in Section 3.1, is provided.

The description of the finite-element method is here kept to a strict minimum. For more detailed information, the reader is referred to the following textbooks: Belytschko et al. (2000); Curnier (2000); Zienkiewicz and Taylor (2000)

3.4.1 Problem Statement

The equation of motion, as already given by Equation (3.10), can be written as

$$\nabla_0 \cdot \mathbf{P}(\mathbf{x}_0, t) + \rho_0(\mathbf{x}_0)\mathbf{b}(\mathbf{x}_0, t) = \rho_0(\mathbf{x}_0)\ddot{\mathbf{u}}(\mathbf{x}_0, t) \quad \forall \mathbf{x}_0 \in \Omega_0 \quad (3.45)$$

with the reference position \mathbf{x}_0 , time t , the material gradient operator ∇_0 , the First Piola-Kirchhoff stress tensor \mathbf{P} , the density ρ_0 , the body force \mathbf{b} , the material acceleration field $\ddot{\mathbf{u}}$, and the reference domain Ω_0 of the solid. The First Piola-Kirchhoff stress tensor \mathbf{P} is given by the constitutive material laws, as shown in Section 3.1.4. The boundary of Ω_0 can be divided into the displacement-imposed domain boundary S_0^u and the traction-imposed domain boundary S_0^t .

The Dirichlet boundary conditions (also known as the essential boundary conditions) on S_0^u states that

$$\mathbf{u}(\mathbf{x}_0, t) = \bar{\mathbf{u}}(\mathbf{x}_0, t) \quad \forall \mathbf{x}_0 \in S_0^u, \quad (3.46)$$

with the displacement field \mathbf{u} , and the imposed boundary displacement vector $\bar{\mathbf{u}}$.

The Neumann boundary conditions (also known as the natural boundary conditions) on S_0^t imposes

$$\mathbf{P}(\mathbf{x}_0, t)\mathbf{n}(\mathbf{x}_0) = \bar{\mathbf{t}}(\mathbf{x}_0, t) \quad \forall \mathbf{x}_0 \in S_0^t, \quad (3.47)$$

with the outwards-pointing boundary normal vector \mathbf{n} , and the boundary traction vector $\bar{\mathbf{t}}$.

The initial conditions of the problem are given by the initial displacement vector \mathbf{u}^i and the initial material velocity vector \mathbf{v}^i as

$$\mathbf{u}(\mathbf{x}_0, t_0) = \mathbf{u}^i(\mathbf{x}_0) \quad \forall \mathbf{x}_0 \in \Omega_0 \quad (3.48)$$

$$\dot{\mathbf{u}}(\mathbf{x}_0, t_0) = \mathbf{v}^i(\mathbf{x}_0) \quad \forall \mathbf{x}_0 \in \Omega_0 \quad (3.49)$$

over the entire domain Ω_0 at $t = t_0$.

The problem statement was provided with full information about the function's parameters. In the following the parameter information is omitted for better readability.

3.4.2 Weak Formulation

The finite-element method of continuum solid mechanics is based on the principle of virtual power applied to the equation of motion. The needed test $\delta\mathbf{u}(\mathbf{x}_0)$ and trial $\mathbf{u}(\mathbf{x}_0, t)$ functions are defined in the spaces \mathcal{U}_0 and \mathcal{U} , respectively. Both, \mathcal{U}_0 and \mathcal{U} , are spaces of kinematically admissible displacements. An additional constraint imposes on \mathcal{U}_0 that all displacements vanish on S_0^u .

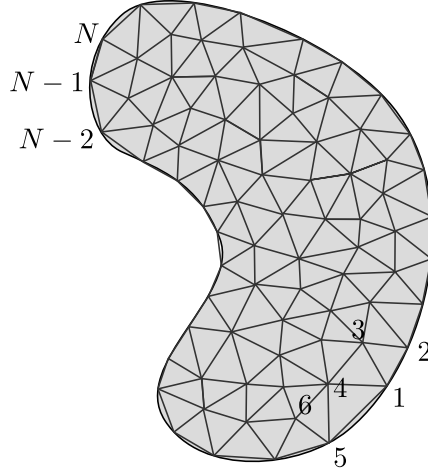


Figure 3.7: Schematic illustration of a triangular finite-element mesh. The continuum body is discretized by the mesh is shown in gray. The nodes of the mesh are numbered from 1 to N .

The weak form results from multiplying Equation (3.45) with the test function and integrating over the initial configuration:

$$\int_{\Omega_0} (\nabla_0 \cdot \mathbf{P} + \rho_0 \mathbf{b} - \rho_0 \dot{\mathbf{u}}) \cdot \delta \mathbf{u} \, d\Omega_0 = 0. \quad (3.50)$$

Applying Gauss's theorem leads to the following expression of the weak form:

$$\int_{\Omega_0} \rho_0 \dot{\mathbf{u}} \cdot \delta \mathbf{u} \, d\Omega_0 + \int_{\Omega_0} \mathbf{P} : \nabla_0 \delta \mathbf{u} \, d\Omega_0 - \int_{\Omega_0} \rho_0 \mathbf{b} \cdot \delta \mathbf{u} \, d\Omega_0 - \int_{S_0^t} \bar{\mathbf{t}} \cdot \delta \mathbf{u} \, dS_0 = 0, \quad (3.51)$$

where $\mathbf{A} : \mathbf{B}$ is the inner product of two second-order tensors. Terms are rearranged, grouping inertial, internal and external forces. For simplicity, this form does not explicitly express the possibility of having different types of boundary conditions (essential vs. natural) in different directions at the same point of the boundary.

3.4.3 Space Discretization

The finite-element solution of the equation of motion is based on the Ritz-Galerkin method. The spatial discretization, for which an example is shown in Figure 3.7, is created using the following approximation for the trial and test functions:

$$\mathbf{u}(\mathbf{x}_0, t) = \sum_{I=1}^N \mathbf{u}_I(t) N_I(\mathbf{x}_0) \quad (3.52)$$

$$\delta \mathbf{u}(\mathbf{x}_0, t) = \sum_{I=1}^N \delta \mathbf{u}_I(t) N_I(\mathbf{x}_0), \quad (3.53)$$

where N_I are the shape functions, \mathbf{u}_I and $\delta\mathbf{u}_I$ are nodal values, and N is the number of nodes of the mesh (see Figure 3.7). The same shape functions are used for all spatial dimensions of the problem. The Ritz-Galerkin method as it is applied here, separates the time and space parameters. The shape functions are constant over time and change only in space, whereas the nodal values are not associated to the variation in space but evolve over time.

Applying the approximation to Equation (3.51), the weak form of the equation of motion can be expressed in matrix form as

$$\mathbf{M}\ddot{\mathbf{u}} + \mathbf{f}^{\text{int}} - \mathbf{f}^{\text{ext}} = \mathbf{0}, \quad (3.54)$$

with the mass matrix \mathbf{M} , the nodal acceleration vector $\ddot{\mathbf{u}}$, the internal force vector \mathbf{f}^{int} , and the external force vector \mathbf{f}^{ext} . These are all global matrices and vectors containing nodal values for all spatial dimensions of all nodes. The contribution of a given node pair I and J is computed by

$$\mathbf{M}_{IJ} = \mathbf{I} \int_{\Omega_0} \rho_0 N_I N_J \, d\Omega_0 \quad (3.55)$$

$$\mathbf{f}_I^{\text{int}} = \int_{\Omega_0} \mathbf{P} \nabla_0 N_I \, d\Omega_0 \quad (3.56)$$

$$\mathbf{f}_I^{\text{ext}} = \int_{\Omega_0} N_I \rho_0 \mathbf{b} \, d\Omega_0 + \int_{S_0^{\text{st}}} N_I \bar{\mathbf{t}} \, dS_0. \quad (3.57)$$

From a computational point of view, local matrices and vectors (at the element level) are often a useful tool for the assembly of the global problem.

3.4.4 Time Discretization

A common time integrator is the Newmark β -method named after its developer Newmark (1959). The two parameters β and γ control stability and artificial viscosity of the integration scheme. Detailed descriptions of the Newmark β -method are given in Curnier (2000) and Belytschko et al. (2000).

The explicit central-difference method, which is the Newmark β -method for $\beta = 0$ and $\gamma = 1/2$, is a well-suited integration scheme for dynamic problems. It is computationally efficient because it solves the matrix system explicitly (as the name indicates).

In the following, we state the different steps of the integration procedure. The n -th time step of the nodal fields is indicated with a subscript n , whereas the superscript i designates the iteration number. The incremental time step is defined as the difference between the time of the current step and the next step as $\Delta t = t_{n+1} - t_n$.

The predictor computes the first estimation of the nodal displacement, velocity, and acceleration field of the next time step. Based on these fields, the external forces are given by the boundary conditions, and the internal force field is computed by the constitutive material law.

Chapter 3. Theoretical and Numerical Framework

The incremental acceleration is computed by solving the equation of motion. The corrector finally applies the incremental acceleration to correct the nodal displacement, velocity and acceleration fields. The equations for these steps are the following:

Step 1 – Predictor:

$$\mathbf{u}_{n+1}^0 = \mathbf{u}_n + \Delta t \dot{\mathbf{u}}_n + \frac{\Delta t^2}{2} \ddot{\mathbf{u}}_n \quad (3.58)$$

$$\dot{\mathbf{u}}_{n+1}^0 = \dot{\mathbf{u}}_n + \Delta t \ddot{\mathbf{u}}_n \quad (3.59)$$

$$\ddot{\mathbf{u}}_{n+1}^0 = \ddot{\mathbf{u}}_n \quad (3.60)$$

Step 2 – Compute Forces:

$$\mathbf{f}_{n+1}^{\text{exti}} \leftarrow \text{boundary condition} \quad (3.61)$$

$$\mathbf{f}_{n+1}^{\text{inti}} \leftarrow \text{constitutive material law} \quad (3.62)$$

Step 3 – Solve (for nodal acceleration increment vector):

$$\delta \ddot{\mathbf{u}} = \mathbf{M}^{-1} \left[\mathbf{f}_{n+1}^{\text{exti}} - \mathbf{f}_{n+1}^{\text{inti}} - \mathbf{M} \ddot{\mathbf{u}}_{n+1}^i \right] \quad (3.63)$$

Step 4 – Corrector:

$$\mathbf{u}_{n+1}^{i+1} = \mathbf{u}_{n+1}^i \quad (3.64)$$

$$\dot{\mathbf{u}}_{n+1}^{i+1} = \dot{\mathbf{u}}_{n+1}^i + \frac{\Delta t}{2} \delta \ddot{\mathbf{u}} \quad (3.65)$$

$$\ddot{\mathbf{u}}_{n+1}^{i+1} = \ddot{\mathbf{u}}_{n+1}^i + \delta \ddot{\mathbf{u}} \quad (3.66)$$

In the explicit central-difference method, one iteration is sufficient to solve the problem. For other (implicit) β -methods, several iterations are needed. In this case, if convergence is not achieved after the corrector, an additional iteration starting with computing the forces (step 2) is needed.

From a computational point of view, an explicit integration scheme is generally less expensive than an implicit method. However, the explicit solution imposes a stability requirement onto the incremental time step, which has to be smaller than a stable time step:

$$\Delta t < \frac{\min |\Delta \mathbf{x}|}{c_d}, \quad (3.67)$$

where $\min |\Delta \mathbf{x}|$ is the smallest distance between any two nodes of the system, and c_d is the dilatational wave speed of the material. If Δt fails to satisfy this condition, the integration leads to unstable (exploding) solutions. Solving the equation of motion can be computationally demanding because the mass matrix has to be inverted and the matrix equation solved. By using a diagonalized mass matrix, often called a lumped mass matrix, the matrix system is

decoupled and the solution of each degree of freedom can be found independently (without solving the entire matrix system).

3.4.5 Static Solution

The static deformation of a continuum solid has to satisfy the equation of equilibrium, which is the equation of motion without the inertial contribution. The equation of equilibrium is deduced from Equation (3.54) by defining $\ddot{\mathbf{u}} = \mathbf{0}$. In Voigt form, the internal force can be split into the product of the stiffness matrix \mathbf{K} and the nodal displacement vector \mathbf{u} as $\mathbf{f}^{\text{int}} = \mathbf{K}\mathbf{u}$. The static solution for the nodal displacement vector can generally be computed for non-linear problems using the Newton-Raphson method. For a linear elastic problem the static solution corresponds to

$$\mathbf{u} = \mathbf{K}^{-1} \mathbf{f}^{\text{ext}} . \quad (3.68)$$

3.4.6 Numerical Damping

Adding numerical damping to the simulation of dynamic systems is sometimes needed for stability reasons or to avoid accumulation of kinetic energy in a pure elastic system. One way of applying numerical damping is introducing an additional term to the equation of motion, such that Equation (3.54) becomes

$$\mathbf{M}\ddot{\mathbf{u}} + \mathbf{C}\dot{\mathbf{u}} + \mathbf{f}^{\text{int}} - \mathbf{f}^{\text{ext}} = \mathbf{0} , \quad (3.69)$$

where \mathbf{C} is a damping matrix. This results in a modification of the solve step in the integration scheme. Hence, Equation (3.63) becomes

$$\delta\ddot{\mathbf{u}} = \left(\mathbf{M} + \frac{\Delta t}{2} \mathbf{C} \right)^{-1} \left[\mathbf{f}_{n+1}^{\text{ext}} - \mathbf{f}_{n+1}^{\text{int}} - \mathbf{C}\dot{\mathbf{u}}_{n+1}^i - \mathbf{M}\ddot{\mathbf{u}}_{n+1}^i \right] . \quad (3.70)$$

There are various ways of defining a damping matrix. A typical method is Rayleigh damping (Rayleigh, 1945), where the damping matrix is a linear combination of the mass matrix and the stiffness matrix. It was shown that this kind of numerical damping results in a damped dynamic system with classical normal modes (Caughey, 1960).

3.5 The Traction-At-Split-Node Method

The development of new and robust techniques for the simulation of contact and friction within the framework of standard computational methods such as the finite-element method is the main goal of the computational contact mechanics research community. Various methods with different advantages and disadvantages exist and the development of a general approach capable of handling any kind of contact is very complex and intensively studied.

The list of textbooks on the computational aspects of contact mechanics and friction is long and includes among others: Laursen (2003); Wriggers (2006); Curnier (2007); Yastrebov (2013).

General contact mechanics methods are particularly useful in commercial software, which are used in a wide variety of problems. A more specialized approach might represent major advantages for specific problems. Computational cost is potentially lower and numerical precision higher. The approach presented here is a forward Lagrange multiplier method (Carpenter et al., 1991) on a node-to-node discretization of the interface. This is particularly suitable for the simulation of small slip at nominally flat interfaces. Contact algorithms with a node-to-node discretization were already applied in the early 1970's and are often referred to as traction-at-split-node method (Andrews, 1973, 1999).

The description of the applied computational contact and friction method is kept to a necessary minimum including the basic weak formulation, the discretized matrix equation, and the numerical algorithm.

3.5.1 Weak Formulation

The weak form of a contact problem is the combination of the weak forms of the two continuum solids and the contact contribution. The weak form of a contact problem is an inequality because the contact conditions (3.23) and (3.24) are inequalities. However, if the contact interface is known, the weak form can be written as an equality. The developed node-to-node algorithm enables a decoupled contact detection for each node pair and provides the possibility of determining the contact interface “on the fly”. For this reason as well as for simplicity, we here provide the weak form as an equality (assuming that the contact interface is known). The following expressions are adapted from the notation of Wriggers (2006).

Using Equation (3.51), the weak form of a continuum solid, we can write

$$\sum_{\iota=1}^2 \left\{ \int_{\Omega_0} \rho_0 \ddot{\mathbf{u}} \cdot \delta \mathbf{u} \, d\Omega_0 + \int_{\Omega_0} \mathbf{P} : \nabla_0 \delta \mathbf{u} \, d\Omega_0 - \int_{\Omega_0} \rho_0 \mathbf{b} \cdot \delta \mathbf{u} \, d\Omega_0 - \int_{S_0^\iota} \bar{\mathbf{t}} \cdot \delta \mathbf{u} \, dS_0 \right\} + C_c = 0, \quad (3.71)$$

where ι is the index of the solid bodies, and C_c is the contact interface contribution.

There are various methods to integrate the contact contribution including the penalty method and the augmented Lagrange method. The Lagrange multiplier method, which is applied here, describes the contact contribution while the interface is sticking as

$$C_{c,stick}^{LM} = \int_{S_0^c} (\Lambda_N \delta g_N^a + \Lambda_T \cdot \delta \mathbf{g}_T^a) \, dS_0 + \int_{S_0^c} (\delta \Lambda_N g_N^a + \delta \Lambda_T \cdot \mathbf{g}_T^a) \, dS_0, \quad (3.72)$$

with Λ_N and Λ_T the normal and tangential Lagrange multipliers, respectively. The test function of the adapted normal and tangential gap are δg_N^a and $\delta \mathbf{g}_T^a$, respectively. The Lagrange multipliers have test functions $\delta \Lambda_N$ and $\delta \Lambda_T$ for the normal and tangential components, respectively. The first term of $C_{c,stick}^{LM}$ corresponds to the virtual work of the Lagrange multipliers

along the variation of the gap function. The second term ensures that the contact and friction constraints are enforced. The Lagrange multipliers represent the contact pressure and the friction traction that occur at the interface.

The contact contribution is different if slip motion occurs at the interface. Instead of finding Λ_T from the no-slip constraint of the interface, it is given by the friction law as \mathbf{r}_T by satisfying Equation (3.28). As there is no need for the tangential constraint, the contact contribution becomes

$$C_{c,\text{slip}}^{\text{LM}} = \int_{S_0^c} (\Lambda_N \delta \mathbf{g}_N^a + \mathbf{r}_T \cdot \delta \mathbf{g}_T^a) dS_0 + \int_{S_0^c} \delta \Lambda_N g_N^a dS_0. \quad (3.73)$$

The stick and slip contact contributions to Equation (3.71) are complementary because an interface can be sticking in some parts and sliding in other parts.

3.5.2 Node-to-Node Discretization

Using a node-to-node approach and the finite-element space discretization, as given in Section 3.4.3, the weak form of the contact problem can be expressed as

$$\mathbf{M}\ddot{\mathbf{u}} + \mathbf{f}^{\text{int}} - \mathbf{f}^{\text{ext}} + \mathbf{G}^T \mathbf{B} \Lambda = \mathbf{0}, \quad (3.74)$$

where Λ is the Lagrange multiplier vector, \mathbf{B} is the boundary matrix, and \mathbf{G} is a surface contact displacement constraint matrix. The node-to-node discretization leads to a Lagrange multiplier vector Λ with one component for each interface node pair and each dimension of the problem. The diagonal matrix \mathbf{B} transforms the Lagrange multiplier vector from a nodal traction vector to a nodal force vector (in units, from Pascal to Newton).

The enforcement of the contact constraint is ensured by

$$\mathbf{G}\mathbf{u} + \mathbf{g}_0 - \mathbf{g}_{\hat{t}} = \mathbf{0}, \quad (3.75)$$

where \mathbf{g}_0 is the initial nodal gap vector, and $\mathbf{g}_{\hat{t}}$ is the last stick gap vector, which is the nodal vector of $\mathbf{g}(\mathbf{x}_0, \hat{t})$ used in the definition of the adapted gap function as given by Equation (3.30).

3.5.3 Time Discretization

The time integration of the contact problem is an essential part of the traction-at-split-node method and needs to be adapted to the time integration scheme of the finite-element method. Carpenter et al. (1991) showed that if the Lagrange multiplier in explicit integration enforces the contact constraints at the current time step, the system of equations presents a singularity because the contact pressure has no influence on the current displacement. They proposed the forward Lagrange multiplier method, an alternative formulation, which relates the current

Chapter 3. Theoretical and Numerical Framework

Lagrange multiplier to the contact constraint of the following time step. This leads to the following matrix system, where the subscript indicates the time step:

$$\mathbf{M}\ddot{\mathbf{u}}_n + \mathbf{f}^{\text{int}}_n - \mathbf{f}^{\text{ext}}_n + \mathbf{G}^T_{n+1}\mathbf{B}\boldsymbol{\Lambda}_n = \mathbf{0}. \quad (3.76)$$

The surface contact displacement constraint matrix \mathbf{G} has to satisfy the non-penetration and stick-slip condition at the following time step through

$$\mathbf{G}_{n+1}\mathbf{u}_{n+1} + \mathbf{g}_{0n+1} - \mathbf{g}_{in+1} = \mathbf{0}. \quad (3.77)$$

In an explicit time integration scheme with lumped mass and boundary matrices, this system is decoupled and the solution of each degree of freedom can be computed independently. Thus, the contact and friction problem can be treated at the level of the split nodes. The Lagrange multiplier vector $\boldsymbol{\Lambda}_n$ of the current step is therefore found by pre-computing steps 3,4 and 1 (of the next time step) for all split nodes. Once $\boldsymbol{\Lambda}_n$ is determined, it contributes locally to the solution through a modified step 3 of the integration scheme presented in Section 3.4.4.

4 A Critical Length Scale in Regularized Friction

Even though numerical simulations are powerful tools to study friction and to gain new insights about local phenomena of slip at frictional interfaces, they also present important challenges. This chapter deals with numerical instabilities and analyzes the effect of friction regularizations on the simulation of interfacial slip. First, it is shown that mesh convergence is obtainable in simulations of slip events at regularized deformable-rigid interfaces without any numerical damping in the bulk. By varying the characteristic length scale of the friction regularization, we demonstrate that there is a critical length below which a given slip front behaves always the same, independent of the regularization. This shows that the propagation of a given slip event at an unregularized interface governed by Coulomb's friction law and at a regularized interface with a characteristic length below the critical value is identical. Therefore, a domain of influence for the friction regularization is defined and used to show that a slip event needs to contain sufficient energy in the high-frequency domain in order to present a propagation affected by the regularization.

This chapter is a modified version of a scientific article originally published by Elsevier as:

D.S. Kammer, V.A. Yastrebov, G. Anciaux, J.F. Molinari, "The existence of a critical length scale in regularised friction", *Journal of the Mechanics and Physics of Solids*, 63(0):40-50, 2014.

4.1 Ill-posedness of the Classical Coulomb Friction Law

Adams (1995) as well as Ranjith and Rice (2001) showed that dynamic sliding of bi-material interfaces under Coulomb's friction law is in many cases unstable, which results in an unbounded increase of displacement oscillations in response to small perturbations at the interface. In real experiments such behavior has never been observed. For the particular case of deformable-rigid interfaces, the stability of Coulomb friction was first studied analytically by Renardy (1992), and Martins and Simões (1995). They showed that sliding of a linear elastic solid on a rigid surface is ill-posed if the static and kinetic coefficients of friction are equal and its value is greater than one: $\mu_s = \mu_k = \mu$ and $\mu > 1$. Moreover, if velocity weakening friction is applied, ill-posedness occurs for smaller friction coefficients as well.

In numerical simulations the instability due to the bi-material effect results in a lack of mesh convergence (Cochard and Rice, 2000). Therefore, most simulations of local slip events need some regularization to solve this stability problem. Two strategies are known: either the regularization is applied onto the bulk (*e.g.*, Rayleigh damping or viscoelastic constitutive material) or at the interface (*e.g.*, friction regularization). In any case, however, it influences the dynamics of local slip events and thus raises questions about the interpretation of numerical results.

A physical basis to interface regularizations is found in the results of experimental work by Prakash and Clifton (1993b). They show that the frictional resistance does not change instantaneously to a sudden jump of the normal force, but evolves continuously with time. This observation opposes the Coulomb friction law, as given by (3.31), where the frictional strength is proportional to the contact pressure with the friction coefficient. Recently, Kilgore et al. (2012) confirmed on a different experimental set-up that there is no direct effect on the frictional strength due to a jump in the normal force. A friction law based on these observations introduces a length scale to the definition of the friction force. It was shown that the use of a simplified version of such friction laws renders the bi-material friction problem well-posed and allows to reach mesh convergence (Cochard and Rice, 2000; Ranjith and Rice, 2001). This regularization of friction has since been used widely for earthquake simulations (Rubin and Ampuero, 2007; Kaneko et al., 2008; Brietzke et al., 2009).

In purpose of avoiding damping in the bulk, we assume here that friction is governed by the Prakash-Clifton law and focus our attention on its effect on the mechanics of slip at frictional interfaces. The parameters of this friction regularization have important implications on the local as well as the global behavior of friction (Di Bartolomeo et al., 2012), and need therefore to be chosen wisely in order to get meaningful numerical results. However, the choice of appropriate parameters is difficult due to the absence of experimental data for most materials. Furthermore, the characteristic length scale deduced from the experiments of Prakash and Clifton (1993b) is of the order of micrometers (Cochard and Rice, 2000), which requires very fine discretization and heavy computational efforts.

In this chapter, we study the rupture of interfaces between deformable and rigid solids gov-

erned by a regularized friction law. Equal static and kinetic friction coefficients that are smaller than one ensure a well-posed problem even without regularization (Renardy, 1992). Choosing a slip event that is well-posed with and without a friction regularization avoids a possible distortion of the analysis of the mechanics of regularized friction due to the transition from an ill-posed to a well-posed problem. In Section 4.3, we confirm that mesh-converged solutions are achieved without numerical damping in the bulk for sliding with regularized friction at a deformable-rigid interface. We then depict a convergence map with respect to the characteristic length of the friction regularization and the discretization of the interface. Using mesh-converged solutions, we show that the friction regularization has for a given slip event a converging behavior with respect to the characteristic length of the regularization.¹ The behavior of a slip event is the same for every characteristic length below the critical length. These observations are confirmed and explained in Section 4.4 by the high-frequency-filter effect of the Prakash-Clifton friction law. The implications of the converging regularization are analyzed in Section 4.5 showing that there is a domain of influence for the Prakash-Clifton friction regularization linked with the characteristic length of the regularization and the spectral content of the slip event. Outside this domain of influence, the propagation of a slip event under regularized friction is equivalent to the propagation under Coulomb's friction law.

4.2 Simulation Set-up

We study the propagation of a rupture at a frictional interface between a semi-infinite isotropic elastic half-space and a rigid flat surface. The set-up is shown in Figure 4.1. This two-dimensional plane strain geometry as well as the material properties are similar to the systems studied by Andrews and Ben-Zion (1997) and Cochard and Rice (2000). We impose in x direction periodic boundary conditions with replication length $L = 40$ m. The height $H = 20$ m ensures that no reflected elastic wave reaches the interface within the time of rupture propagation and does not influence the results of the simulations. The deformable solid is subjected to a remote compressive normal load $-\bar{p} = 0.0150$ Pa and a remote shear load $\bar{t} = 0.0105$ Pa.

The material properties of the elastic solid are density $\rho = 1$ kg/m³, Young's modulus $E = 2.5$ Pa, and Poisson's ratio $\nu = 0.25$. The resulting elastic wave speeds for dilatational and shear waves are $c_d = 1.73$ m/s and $c_s = 1.0$ m/s, respectively. Friction at the interface is governed by Coulomb's law with equal static and kinetic coefficient of friction $\mu = 0.75$, as presented in Section 3.2.3, and is regularized by a simplified Prakash and Clifton (1993b) law as proposed by Cochard and Rice (2000)

$$\frac{d\tau^{\text{es}}}{dt} = -\frac{\dot{\delta} + \nu_{\text{pc}}}{d_{\text{pc}}} (\tau^{\text{es}} - \tau^{\text{s}}), \quad (4.1)$$

where τ^{es} is the effective (regularized) frictional strength, τ^{s} is the unregularized frictional

¹Note that throughout this chapter two different convergences are considered: convergence with respect to the mesh discretization, and with respect to the characteristic length of the friction regularization.

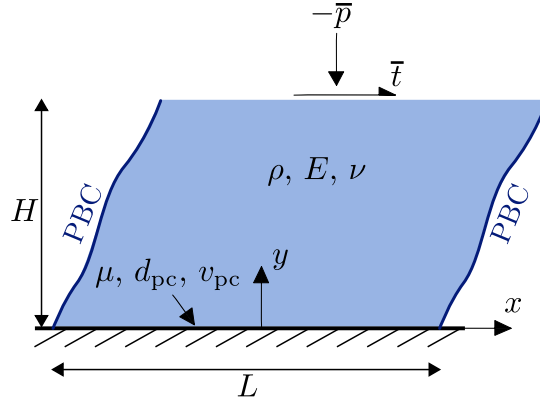


Figure 4.1: Two-dimensional plane strain model of a frictional interface between an isotropic elastic semi-infinite half-space and a rigid plane. PBC indicates a periodic boundary condition. The deformable solid is subjected to a remote static normal and shear load. A rupture, which is nucleated artificially, propagates along the interface until it stops naturally.

strength based on Coulomb's friction law, as given by (3.31), $\dot{\delta}$ is the slip rate, v_{pc} is a (positive) reference rate, and d_{pc} is the characteristic length of the regularization. The combination of friction parameters, material properties and imposed loading conditions induces a uniform shear traction at the interface that is at 93.3% of the frictional strength ($\bar{t} = 0.933\mu|\bar{p}|$). This value enables the propagation of an interface rupture nucleated by an artificial change of normal contact pressure, as it was done in previous studies (Andrews and Ben-Zion, 1997; Cochard and Rice, 2000). A detailed description of the nucleation procedure is provided in Appendix A.1 as it was already presented in Cochard and Rice (2000). This spatial-temporal nucleation region is of elliptic shape in the $x - t$ plane with a_{ell} and b_{ell} being half the ellipse's minor and major axis, respectively. The parameter v_{ell} inclines the elliptic shape of the nucleation region in the $x - t$, which ensures that the propagation of the interface rupture is oriented in the positive direction of x (*i.e.*, the maximum of the artificial change of contact pressure propagates roughly at velocity v_{ell} in the x direction). The parameter choice for this study is $a_{ell} = 0.6$ m, $b_{ell} = 3.6$ m, and $v_{ell} = 0.825$ m/s. In contrast to previous work, our simulation tool allows for interface opening. In order to avoid such opening and to be consistent with previous studies, we decrease the contact pressure by at most 80% of its initial value.

The system is modeled using the finite-element method with an explicit Newmark β -integration scheme and a lumped mass matrix. A detailed description of the method is given in Section 3.4. The deformable solid is discretized by regular quadrilateral elements with linear interpolation and four integration points. The mesh is characterized by the node density n_d at the interface, which ranges in the present study from 10 to 120 nodes per meter (nd/m). The mesh density is homogeneous in the entire solid in order to avoid spurious wave reflections due to a gradient of mesh density.

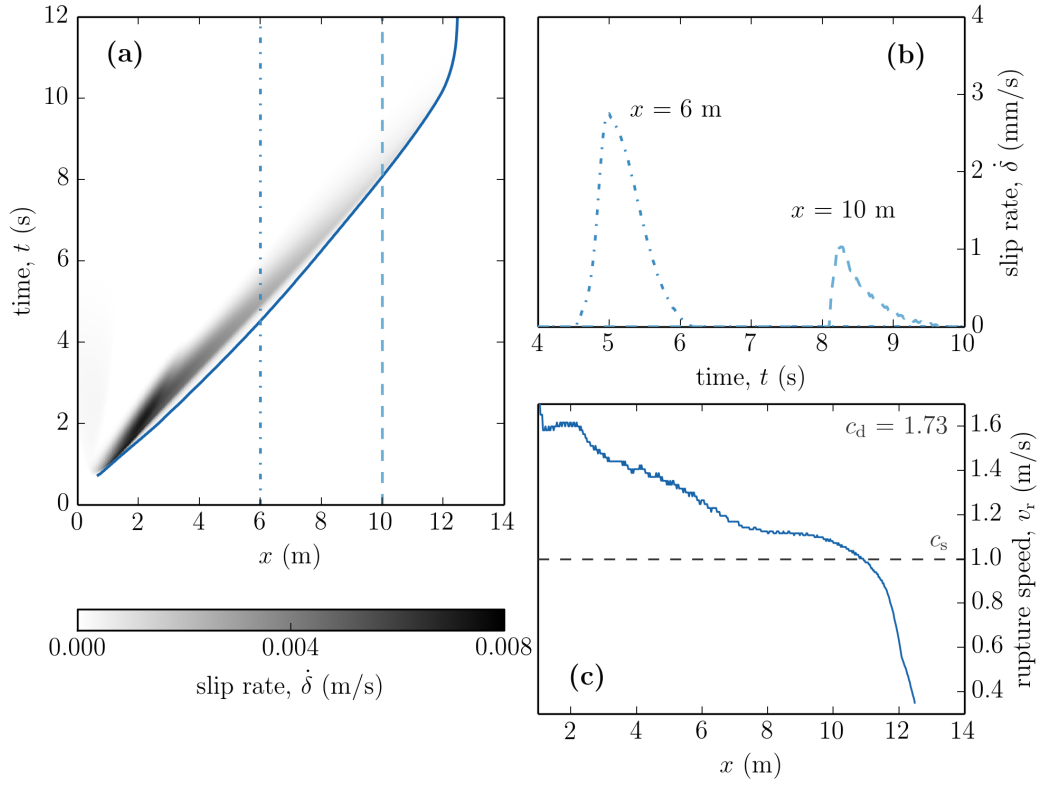


Figure 4.2: Example of interface rupture with regularization parameters $\nu_{pc} = 10^{-4}$ m/s and $d_{pc} = 5 \cdot 10^{-5}$ m; and interface mesh density $n_d = 40$ nd/m. **(a)** Slip rate $\dot{\delta}$ is shown in the spatial-temporal $x - t$ plane as grey area, where darker colors correspond to higher slip rates. Vertical lines in **(a)** indicate positions for which in **(b)** the evolution of $\dot{\delta}$ is shown over time. The dark line adjacent to the grey area in **(a)** marks the front of the interface rupture for which the propagation speed is traced in **(c)**.

A typical result of a nucleated interface rupture is shown in Figure 4.2. The contact pressure reduction, which triggers the slip event, is located close to the origin. From this point the rupture propagates in the positive direction of x . The maximal slip rate is $\dot{\delta} = 8$ mm/s in the beginning and decreases continuously until the rupture stops at $x \approx 12.5$ m. The dark line adjacent to the grey area in Figure 4.2(a) indicates space and time when the slip rate starts to be non-zero, which we call hereinafter the *slip front*. The light area between this dark line and the dark parts of the grey area shows that the maximal slip rate does not occur at the front of the interface rupture, which is also notable in Figure 4.2(b). However, the time between the slip front and the maximum of the slip rate generally reduces with increasing propagation distance.

The rupture speed v_r shown in Figure 4.2(c) corresponds to the slope of the dark curve in Figure 4.2(a). The rupture propagates with super-shear speed, $c_s < v_r < c_d$, during almost its entire propagation. It decelerates fast only shortly before the arrest of slip. Even though the

slip front in the $x - t$ plane seems to be straight, the rupture speed slows down continuously except for a short distance at $x = 8 - 10$ m, where it remains quasi constant. The decreasing rupture speed along $0 < x < 8$ m is the transition phase before the rupture enters a steady state, which lasts in this simulation for approximately 2 m until the phase of arrest starts. Other simulations with different regularization parameters present steady state phases that may span over almost the entire propagation distance.

In the next section, the slip rate $\dot{\delta}$ as well as the rupture speed v_r are analyzed for different mesh densities and different values of friction regularization parameters. We show that the interface ruptures simulated with regularized friction do not only converge with respect to the mesh, but also with respect to the characteristic length of the regularization.

4.3 Influence of Friction Regularization on Slip

The simplified Prakash-Clifton friction regularization as proposed by Cochard and Rice (2000) has two parameters, d_{pc} and v_{pc} , and depends on the slip rate $\dot{\delta}$. In order to simplify the analysis of this regularization in the present study, we fix $v_{pc} = 10^{-4}$ m/s and consider the variation of the characteristic length d_{pc} . Different values for v_{pc} result in equivalent observations and conclusions. This simplification leads to a regularization that still depends on the slip rate. Other approaches were applied in previous studies (DeDontney et al., 2011; Di Bartolomeo et al., 2012), where the $(\dot{\delta} + v_{pc})/d_{pc}$ term was replaced by $1/t^*$. The resulting one-parameter regularization is similar to our simplification but without dependence on slip rate.

Before studying the influence of the friction regularization on the propagation of interface ruptures, we first confirm the mesh-converging quality of the system under consideration and determine a convergence map with respect to the characteristic length d_{pc} . This map enables the choice of an appropriate mesh density for a given d_{pc} in order to study the effects of the friction regularization on mesh-converged simulations.

4.3.1 Mesh Refinement Analysis

The mesh refinement analysis is conducted on meshes with interface node densities n_d ranging from 10 nd/m to 120 nd/m. The slip rate and rupture speed for $d_{pc} = 5 \cdot 10^{-6}$ m and different meshes are shown in Figure 4.3, where the color intensity is chosen accordingly to the mesh density with dark colors being finer meshes. High-frequency oscillations with important amplitudes are present in simulations with coarse meshes. By refining the mesh, the dominant oscillations increase in frequency and decrease in amplitude. Mesh convergence is achieved when by refining the discretization the relative error over the slip event's total propagation distance is below 0.5%. In addition, we measure the arrival time at $x = 11$ m. The relative error of this time due to the last mesh refinement is below 0.1% for the case presented in Figure 4.3.

In contrast to the slip rate, the propagation speed of the interface rupture is less affected by

4.3. Influence of Friction Regularization on Slip

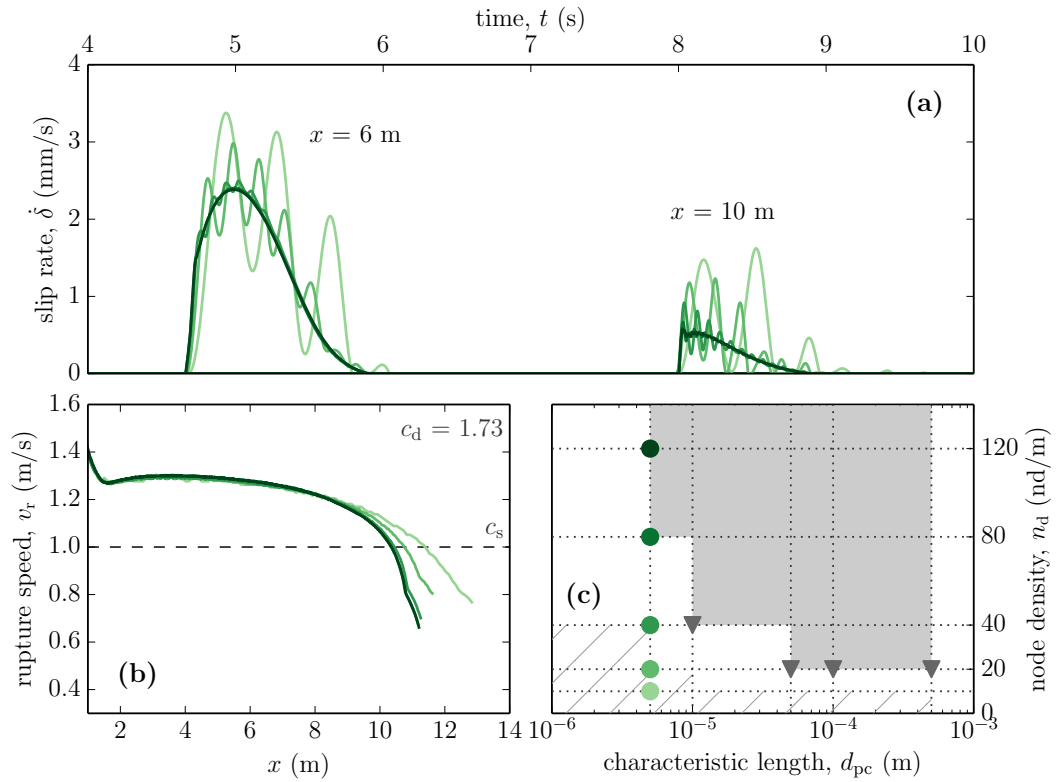


Figure 4.3: Illustration of mesh convergence for a frictional interface rupture with simplified Prakash-Clifton regularization $d_{pc} = 5 \cdot 10^{-6}$ m and $v_{pc} = 10^{-4}$ m/s. **(a)** The evolution of the slip rate over time is shown at two positions. **(b)** The rupture speed is depicted with respect to x . **(c)** The convergence map in the $d_{pc} - n_d$ plane indicates the zone of mesh-converged (solid area) and unconverged (hatched area) simulations for $v_{pc} = 10^{-4}$ m/s. The filled circles designate the simulations presented in (a) and (b). The triangles mark mesh-converged simulations for different d_{pc} .

the mesh density. The difference can be distinguished only in the arrest-phase, where for the finer mesh the rupture speed decreases significantly faster. A coarser (non-converged) mesh causes the interface rupture to propagate farther and faster during the arrest phase than the converged solution. Compared with the results obtained for $d_{pc} = 5 \cdot 10^{-5}$ m (see Figure 4.2), the rupture speed for this slip event, with $d_{pc} = 5 \cdot 10^{-6}$ m, is more steady before arresting and does not present an important decelerating phase before the steady propagation.

The mesh converging behavior of this interface rupture is summarized in Figure 4.3(c). The filled circles indicate the characteristic length and the node densities of the simulations for which slip rates and rupture speeds are presented in Figure 4.3(a-b). Similar analysis were conducted with different values of d_{pc} . The corresponding node densities at the limit of mesh convergence are indicated with triangles. Simulations with $d_{pc} = 10^{-3}$ m present no interface rupture anymore due to the strong regularization, which prevents initiation of slip

for the considered triggering. The solid area marks the zone of mesh-converged solutions, whereas the hatched area shows the zone of non-converged simulations. The limit of mesh-convergence is located in the white area between the two marked zones. The convergence map demonstrates that simulations with smaller characteristic lengths of the friction regularization need finer meshes for mesh-converged solutions. This observation, which was already noticed without illustration by Cochard and Rice (2000), is here confirmed and visualised.

A main observation in Figure 4.3(a) is that the mesh refinement changes the frequency of the perturbing oscillations. The origin of these oscillations lies in the non-smoothness of the slip rate in the transition from stick to slip, which excites all ranges of frequencies of the system. A finite discretized solid, however, has only a limited and discrete set of eigenfrequencies. Therefore, the energy in the spectral space above the highest representable frequency of the discretization seems to be lumped at this maximal eigenfrequency of the mesh, which is also in the range of the perturbing oscillations. Because smaller elements enable the representation of shorter wavelengths, mesh refinement causes higher frequencies of the oscillations. The presence of high-frequency noise is common in this kind of simulations and it is often eliminated by numerical damping in the bulk. Here, we have shown that simulations with regularized friction converge without any bulk damping, which is a necessary condition in order to be able to study the influence of the friction regularization on the propagation of interface ruptures. It is interesting to note that this (damping like) stabilising effect of regularized friction on numerical problems has already been exploited in recent studies on well-posed problems (*e.g.*, frictional interfaces between similar materials) (DeDontney et al., 2012).

4.3.2 Length Scale Convergence

We now study the influence of the regularization's length scale d_{pc} on the slip rate and rupture speed (see Figure 4.4), similarly as in the mesh convergence analysis. The applied meshes are chosen based on the convergence map, as presented in the previous section, at the limit of mesh convergence. The value of the friction regularization strongly affects both the slip rate and the rupture speed, see Figure 4.4(a) and (b). The simulation with the largest characteristic length d_{pc} (in lightest color) is the most salient with a considerably smaller slip rate at $x = 6$ m. Further, the slip front reaches $x = 6$ m later than the other simulations despite higher rupture speeds until this position. At a first glance this seems to be incoherent. However, the strong regularization delays the initiation of the interface rupture, which explains why the slip front is behind the rupture tip of the other simulation despite its higher propagation speed. The interface rupture with the second and third largest characteristic lengths ($d_{pc} = 10^{-4}$ m and $d_{pc} = 5 \cdot 10^{-5}$ m) have a similar behavior. Both have at $x = 6$ m a maximal slip rate of around 3 mm/s and reach the point at around 4.5 s. Both slip events also present a rupture speed that decelerates from 1.6 m/s to 1.0 m/s along almost the complete propagation distance until they arrest abruptly. Similar to the example shown in Figure 4.2, these interface ruptures do not have a phase of steady propagation.

4.3. Influence of Friction Regularization on Slip

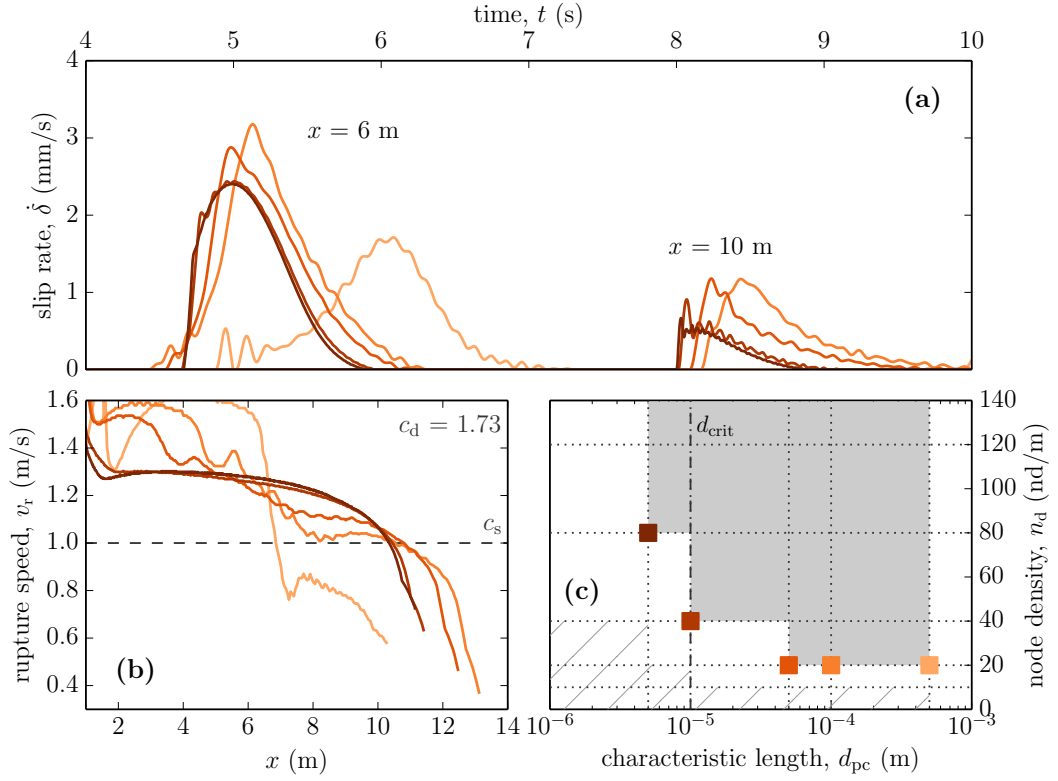


Figure 4.4: The slip rate in (a) and the rupture speed in (b) of mesh-converged simulations are shown for different characteristic lengths d_{pc} . (c) The squares indicate the node density n_d and characteristic length d_{pc} of the simulations presented in (a) and (b). All shown results are in the mesh-converged area of the $d_{pc} - n_d$ plane. d_{crit} marks the critical characteristic length of the simplified Prakash-Clifton friction law for the presented interface rupture, below which all converged simulations have the same global and local behavior.

The two slip events with the smallest d_{pc} (in darkest colors) obey almost the same propagation behavior. The slip rate evolution over time at $x = 6$ m and $x = 10$ m are nearly indiscernible. The most noticeable difference is the rupture speed for $x < 2$ m, where a larger characteristic length causes a slightly higher rupture speed. As already illustrated on the slip event shown in Figure 4.3, the propagation speed for interface ruptures with small characteristic lengths presents a steady phase with an almost constant speed during a large part of the propagation distance. Comparing the interface ruptures for all five different characteristic lengths, starting from the largest d_{pc} , we observe a converging behavior with respect to a decreasing characteristic length d_{pc} . This shows that there is a critical characteristic length d_{crit} below which the choice of d_{pc} does not influence the propagation of a given slip event. For the interface rupture presented here, the critical length is estimated as $d_{crit} = 10^{-5}$ m. This convergence of the interface rupture with respect to the friction regularization has not been observed before.

4.4 Filter Analogy of Frictional Regularization

In Section 4.3, we observed that the regularization affects differently the oscillations of various frequencies in the slip rate $\dot{\delta}$. These oscillations are closely related to coupled oscillations of the frictional and normal forces. The oscillations in the frictional force and in the slip rate vanish with the refinement of the mesh. The evolution of (mesh-converged) regularized frictional strengths for different d_{pc} at $x = 6\text{m}$ are shown in Figure 4.5(a). Similarly to the slip rates, the evolution of the frictional strength during the propagation of the interface rupture is smoother if the regularization d_{pc} is larger. Further, the simulation with the smallest characteristic length, which is converged with respect to d_{pc} , has a sharp peak at $t \approx 4.8\text{s}$. This feature is related to the fast transition from stick to slip, which is at the origin of the perturbing high frequency oscillations. The increasing non-smoothness of the transition for smaller regularizations gives a first hint to why finer discretizations are needed in order to achieve mesh-converged solutions for interface ruptures with small d_{pc} .

We suggest to consider the simplified Prakash-Clifton friction as a (temporal) filter for Coulomb's friction. The physical phenomenon that is regularized is therefore regarded as a signal. The filter receives an input signal, which is the unregularized frictional strength τ^s (Coulomb friction), and creates a filtered (or regularized) output signal, which is the effective frictional strength τ^{es} (Prakash-Clifton friction). If the filter based on (4.1) receives an input signal with average value $\bar{\tau}^s$ and a sinusoidal variation over time t of a given frequency f and amplitude A^s , the steady-state output signal (for $t \gg 1$) is of the same frequency but with a phase offset and a modified amplitude A^{es} . An example of an input signal (solid line) and the resulting output signal (dashed line) is shown in Figure 4.5(b). The analytical solution of the relative regularized frictional strength A^{es}/A^s is given by

$$\frac{A^{es}}{A^s} = \frac{1}{\sqrt{1 + \left(\frac{2\pi f}{C}\right)^2}} \quad (4.2)$$

with $C = -(v_{pc} + \dot{\delta})/d_{pc} < 0$. The complete derivation of (4.2) is given in Appendix A.2. The filter's influence on the variation of the output signal is independent from the average value $\bar{\tau}^s$ and from the friction coefficient μ . For physical interpretation, we impose $A^s < \bar{\tau}^s$ in order to avoid ambiguity of frictional strength during interface opening. Concerned by spurious oscillations in the simulations, we neglect the analysis of the phase offset and focus on the influence of the filter on the amplitude of the signal. The ratio of amplitudes of the output and input signals (A^{es}/A^s) as a function of the signal's frequency is shown in Figure 4.5(c) for filters of different characteristic lengths d_{pc} . The values of d_{pc} as well as the color code are the same as for the simulations of interface ruptures presented in Figure 4.4. The curves as well as (4.2) confirm that the simplified Prakash-Clifton friction law attenuates more the signals of high frequencies. It was shown by Ranjith and Rice (2001) that interfacial disturbances present unstable growth for all wavelengths and that the growth rate is inversely proportional to the wavelength. By having a stronger filtering of high frequencies, the friction regularization

4.4. Filter Analogy of Frictional Regularization

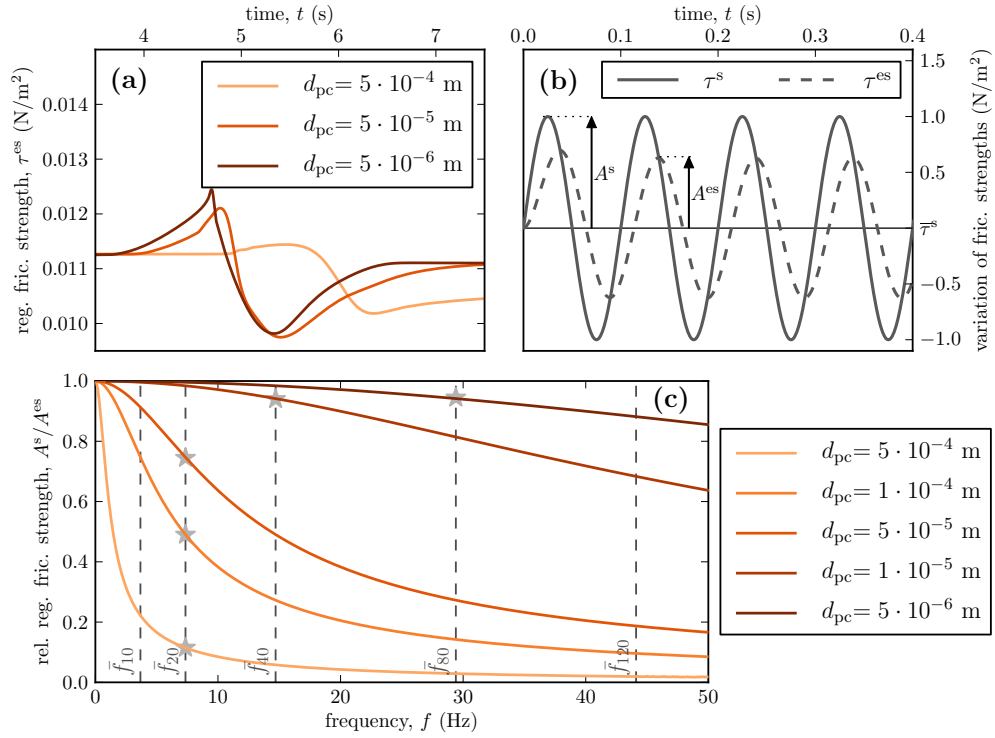


Figure 4.5: Frequency analysis of the simplified Prakash-Clifton friction law. **(a)** Variation of the regularized frictional strength τ^{es} over time at $x = 6$ m for the simulations of triggered interface ruptures as studied in Section 4.3.2. **(b)** Spectral analysis of periodic variations in unregularized frictional strength τ^s (Coulomb friction) around average value $\bar{\tau}^s$ with amplitude A^s (solid line) shows that the regularized frictional force τ^{es} has a shifted phase, the same frequency and reduced amplitude A^{es} (dashed line). **(c)** The relative regularized frictional strength A^e/A^s is shown with respect to the frequency of the input signal for friction laws with different characteristic lengths d_{pc} . The dashed vertical lines designated with \bar{f}_{n_d} indicate the highest eigenfrequencies of meshes with node density n_d applied in the finite-element simulations in Section 4.3. Grey stars mark for each characteristic length the node density needed for mesh-converged solutions.

compensates for the unstable growth due to interfacial disturbances and solves the problem of the ill-posedness of Coulomb friction at bi-material interfaces.

The signal of a given frequency is more attenuated by a regularization with larger d_{pc} . This consideration explains the link between d_{pc} and the node density needed to obtain mesh-converged simulations. The highest eigenfrequencies of the meshes used for the simulations presented in Section 4.3 are indicated by vertical dashed lines in Figure 4.5(c). They are labeled with \bar{f}_{n_d} where n_d specifies the interface node density of the mesh. Considering, for instance, the mesh with node density $n_d = 20$ nd/m, we see that its highest eigenfrequency is reduced to about 50% for $d_{pc} = 10^{-4}$ m. This is sufficient to obtain a mesh-converged solution. A smaller

characteristic length, *e.g.*, $d_{pc} = 10^{-5}$ m, attenuates a signal of frequency $f = 20$ Hz only by two percent, which appears to be insufficient for obtaining mesh-converged solutions. In the previous section, it was shown that a mesh with node density $n_d = 40$ nd/m is needed to obtain mesh convergence for this d_{pc} . The grey stars in Figure 4.5(c) indicate for each characteristic length the needed node density for mesh-converged solutions. Two different regimes are observed: 1) simulations with $d_{pc} \geq 5 \cdot 10^{-5}$ m, where mesh-converged solutions are achieved with node density $n_d = 20$ nd/m independently of the attenuation of the highest frequency, and 2) simulations with $d_{pc} \leq 1 \cdot 10^{-5}$ m, where different node densities n_d are needed to obtain mesh-converged solutions. For the latter regime, a mesh-convergence criterion can be defined. The current simulations indicate a need for an attenuation ratio A^{es}/A^s of maximal 95% to avoid perturbing oscillations and to obtain mesh-converged solutions. On the other hand, slip fronts at interfaces with larger d_{pc} (regime 1) do not present a particular attenuation ratio that satisfies convergence criterion. The explanation for this absence of criterion lies in the low range of frequencies. Although the highest frequencies of even coarser meshes seem to be attenuated sufficiently, these frequencies are needed in order to describe accurately the evolution of the frictional strength as shown in Figure 4.5(a). Therefore, convergence cannot be achieved with meshes of node densities smaller than $n_d = 20$ nd/m for this particular interface rupture because all needed frequencies are not present with coarser meshes.

The same argument is valid as explanation of the other convergence: the convergence with respect to the characteristic length d_{pc} of the Prakash-Clifton friction law. The evolution of the frictional strength over time of this given slip event is mostly composed of low frequencies. The mesh convergence regime 2 indicates that these frequencies lie below \bar{f}_{20} , which present attenuation ratios that approach one for decreasing characteristic lengths. Therefore, the influence of the friction regularization on the evolution of the frictional strength is vanishingly small starting from the critical length d_{crit} . In our case, we find $d_{crit} = 10^{-5}$ m, which has a minimal attenuation ratio A^{es}/A^s of 0.98% at \bar{f}_{20} . Every d_{pc} smaller than d_{crit} has negligible influence on the frequencies forming the slip event and every simulation with $d_{pc} \leq d_{crit}$ obeys the same behavior, which we call here the convergence with respect to the characteristic length of the friction regularization. These explanations confirm the observations based on finite-element simulations as reported in Section 4.3.2 and suggest that similar critical length scales should exist for slip events propagating at more general deformable-deformable interfaces.

4.5 Physical Interpretation

The critical characteristic length d_{crit} depends on the spectral content of the slip event, which is the result of the nucleation procedure. d_{crit} decreases for slip events reaching higher frequency ranges, as shown schematically in Figure 4.6. The relation between the critical length and the maximal frequency of a slip event is $d_{crit} \propto 1/f$, if a limiting attenuation ratio is assumed in (4.2). The hatched area $d_{pc} > d_{crit}$ in Figure 4.6 indicates the domain, where the parameter d_{pc} influences the solution. In the white area $d_{pc} \leq d_{crit}$, the solution is no longer affected

by the regularization. In this zone, the regularized slip propagation is equivalent to the non-regularized propagation (classical Coulomb friction), because the regularization's influence is vanishingly small.

Up to this point we considered a regularization as part of a modeling technique (based on physical observations) and showed that there is convergence with respect to its length scale d_{pc} without looking at the physical value of d_{pc} . Let us now assume that the interface has a physical length d_{ph} due to the presence of micro-contacts and that the interface is not governed by Coulomb friction. In this case, it would be important to determine d_{ph} for different interfaces in order to improve our understanding of frictional dynamics. However, until today, only few experiments (Prakash and Clifton, 1993b; Kilgore et al., 2012) have been able to show that friction has a characteristic length d_{ph} with respect to sudden changes in the contact pressure. The value of d_{ph} is estimated (Cochard and Rice, 2000) to be of the order of microns for the experiments of Prakash and Clifton (1993b). The experimental determination of d_{ph} , however, is challenging and our results show that the studied slip events have to be sufficiently rich in high frequencies in order to make the measurement possible.

Considering a particular interface with a given d_{ph} , one can distinguish the frequencies that are affected by the characteristic length from the frequencies that are not influenced. This critical frequency is given by $d_{crit}(f_{crit}) = d_{ph}$. Any slip event that has approximately all its frequency content below f_{crit} – situated to the left of the diamond in Figure 4.6 – is not influenced by d_{ph} and propagates as if the interface was governed by Coulomb's friction law. Therefore, one has to choose carefully the studied slip event and its nucleation procedure in order to determine experimentally d_{ph} of a new interface. The recommended evaluation procedure consists of: 1) experimentally monitor a slip pulse, 2) determine the measured characteristic length d_m by fitting the friction law to the experimental data, 3) compute the measured critical frequency with $d_{crit}(f_m) = d_m$, 4) if the frequency content of the monitored slip event exceeds f_m , the procedure was successful and the measured length scale is the physical length of the interface: $d_{ph} = d_m$ and $f_{crit} = f_m$. Otherwise, the studied slip event is not sufficiently rich in high frequencies and the procedure has to be repeated with a sharper slip event, because $d_m = d_{crit}$.

From a numerical point of view, the critical length scale d_{crit} gives in many cases the opportunity of introducing the Prakash-Clifton regularization in order to solve the issue of perturbing numerical oscillations without influencing the dynamics of the frictional interface rupture. Any regularization with a characteristic length smaller than the critical length does not affect the propagation of the slip event and the observable behavior corresponds to the propagation under Coulomb's friction law. In addition to the effect of removing nuisance oscillations, using the critical characteristic length in numerical simulations minimises the computational efforts because smaller characteristic lengths require finer discretizations. For instance, if the physical length d_{ph} is smaller than the critical length d_{crit} , numerical simulations can be carried out using d_{crit} instead of d_{ph} without losing the physical bases of the results. On the other hand, simulations of interface ruptures for which the spectral content above the

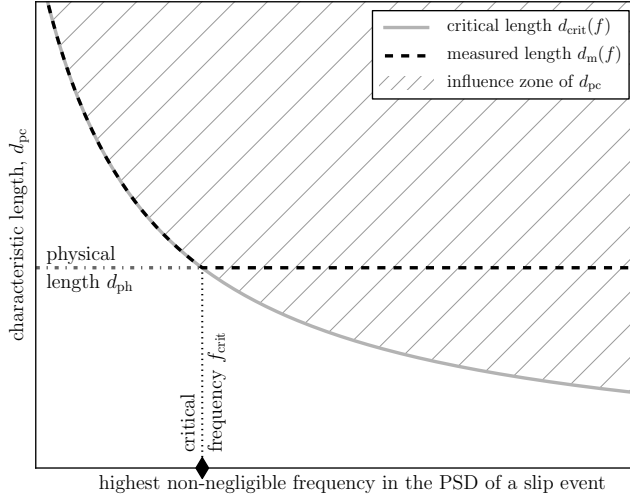


Figure 4.6: Schematic visualisation of the zone of influence of the Prakash-Clifton friction regularization. The critical characteristic length d_{crit} decreases for slip events with a power spectral density that presents higher non-negligible frequencies. Considering that an interface is not governed by Coulomb’s law but actually has a physical length d_{ph} , assumed to be independent of the frequency. The intersection of physical and critical lengths defines the critical frequency f_{crit} , which separates the slip event’s frequencies that propagate under Prakash-Clifton’s regularization ($f > f_{\text{crit}}$) and that is governed by Coulomb friction ($f \leq f_{\text{crit}}$). Fitting the Prakash-Clifton law to the friction and contact forces of a particular slip event with highest non-negligible frequency f results in the measured length scale $d_m(f)$. If $f \geq f_{\text{crit}}$, the measured length scale is the physical property of the interface, whereas if $f < f_{\text{crit}}$, the measured length is the critical length, which is higher than d_{ph} .

critical frequency $f > f_{\text{crit}}$ is important, does not provide any flexibility in the choice of the regularization parameters. The characteristic length has to be exactly equal to the physical length $d_{\text{pc}} = d_{\text{ph}}$ in order to obtain a correct simulation of the physical behavior.

4.6 Conclusion

We studied the simplified Prakash-Clifton friction law, which regularizes Coulomb’s friction with respect to sudden changes in contact pressure. As a test problem we considered the rupture of a planar frictional interface between an elastic solid and a rigid plane. The rupture was triggered artificially such that the slip front propagates in the direction of the movement of the elastic solid and stops after a while. Different stages of the propagation were observed: primary (a transition right after the initiation), steady (the front speed is almost constant), arresting (the front decelerates and stops). We first confirmed that mesh-converged solutions are achievable in the stable regime (for friction coefficients smaller than one) of the considered

problem without any numerical damping in the bulk. We delimited a mesh-convergence map with respect to the characteristic length d_{pc} of the Prakash-Clifton friction law. This map confirmed that mesh-converged solutions for smaller lengths need finer mesh discretizations.

In addition to mesh convergence, we discovered a convergence of the solution with respect to the characteristic length d_{pc} . This observation results from the analysis of mesh-converged solutions for different characteristic lengths. Considering a given slip event, a critical characteristic length d_{crit} exists, such that for any $d_{pc} < d_{crit}$ the propagation behavior of the interface rupture is the same. To confirm and explain this observation, we analyzed the regularization's effect on a range of temporal frequencies of the frictional strength. The damping of low frequencies, which are the essential part of the slip event, becomes vanishingly small for small characteristic lengths and influences no longer the propagation of the interface rupture. This insight enables the definition of a theoretical domain $d_{pc} > d_{crit}$ of influence of the Prakash-Clifton friction law with respect to the characteristic length of the regularization and the frequency content of the slip event. Outside of this domain $d_{pc} \leq d_{crit}$, the damping of the slip event's frequencies becomes negligible and the interface rupture propagates as if it was governed by Coulomb's friction law despite the presence of the regularization.

In conclusion, the presented results suggest that the experimental determination of the physical length scale d_{ph} of the Prakash-Clifton friction law requires the temporal power spectrum density of the analyzed slip event to contain enough energy in the high-frequency domain. We therefore propose an evaluation procedure that includes a verification of the slip event's frequency content. This is crucial to a successful determination of d_{ph} , because if the propagation of slip is fully determined by frequencies below a critical value, the real physical length scale d_{ph} of the Prakash-Clifton friction cannot be measured. The observed length scale instead corresponds to the critical length d_{crit} , which may be significantly higher.

5 Criteria for the Slip Front Speed

When slip fronts propagate at frictional interfaces, they do so at various speeds. Experimentally, it was observed that the rupture speed is closely related to the shear to normal stress ratio at the interface. This chapter confirms this observation using numerical simulations. However, it also demonstrates that the propagation direction affects the front speed and that the stress-speed relation is not unique. In order to improve the description of the propagation speed, two dynamic criteria are proposed. First, the stress ratio based on stresses dynamically measured during the propagation at a small distance in front of the rupture tip is considered. Even though this criterion is an improvement compared to the static stress ratio description, there is still a direction dependence in the rupture speed description. Second, a dynamic energy-based approach is proposed and shown to provide a unique stress-speed relation for slip fronts.

This chapter is a modified version of a scientific article originally published by Springer as:

D.S. Kammer, V.A. Yastrebov, P. Spijker, J.F. Molinari, “On the Propagation of Slip Fronts at Frictional Interfaces”, *Tribology Letters*, 48(1):27-32, 2012.

5.1 Slip Fronts Propagating at Various Speeds

The onset of dynamic sliding is often globally perceived as a uniform transition from sticking to sliding. In reality, however, it is a much more complex phenomenon. The shear stress distribution at an interface is generally nonuniform and reaches therefore the shear strength only at a narrow zone in which a slip front initiates. This frictional shear rupture propagates from this point on along the interface until it arrests naturally or reaches the edges.

Frictional shear cracks at interfaces between two solids have been observed in various experiments under different loading conditions and for different initiation processes (Baumberger et al., 2002; Rubinstein et al., 2004, 2007; Ben-David et al., 2010; Coker et al., 2005). Tracking the expansion of the slip fronts, it was shown that the measured speed of propagation range from slow (Baumberger et al., 2002; Rubinstein et al., 2004, 2007) to super-sonic (Coker et al., 2005).

However, different rupture speeds do not only vary from one experiment to another. A single slip event can change its speed any time during the propagation. Even surprisingly large speed jumps occur, such as from super-shear to slow propagation or the opposite (Rubinstein et al., 2004). By studying the stress field close to the interface, Ben-David et al. (2010) observed experimentally that the rupture speed of the slip front is coupled to the local ratio of shear stress τ_{st} to normal stress σ_{st} measured before slip initiation.

These experimental observations have numerically been reproduced with various models. One-dimensional (Braun et al., 2009) and two-dimensional (Trømborg et al., 2011, 2014) mass-spring models presented slip fronts at different speeds for set-ups with varying stress distributions along the interface. Other numerical models established that friction laws which consist of a rate-weakening-strengthening process cause the propagation of slow fronts (Bouchbinder et al., 2011; Bar Sinai et al., 2012).

In this chapter, we study numerically the propagation of a spontaneously initiated frictional slip front. We re-examine the hypothesis of Ben-David et al. (2010) on the correlation between the slip front speed and τ_{st}/σ_{st} with a set-up comparable to the experimental system providing realistic stress distributions along the interface. The applied finite-element method allows us to access dynamically, during the propagation of the front, detailed information about the evolution of the stress and represent correctly the mechanical behavior of the simulated solid (*e.g.* isotropy, elasticity).

5.2 Model Set-up

The two-dimensional system under consideration consists of a rectangular isotropic elastic plate ($L = 200$ mm, $H = 100$ mm) in contact with a rigid plane, as shown in Figure 5.1(a). The corners of the plate are rounded to avoid stress singularities at the edges. To study this system we use the finite-element method with an explicit Newmark β -integration scheme. More

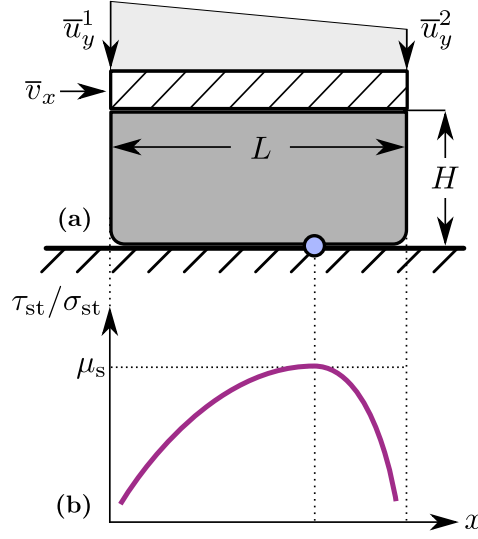


Figure 5.1: Two-dimensional set-up of the problem: **(a)** a thin rectangular plate in contact with a rigid plane is loaded on the top by a linearly distributed imposed displacement \bar{u}_y and a uniform velocity \bar{v}_x ; **(b)** the nonuniform distribution of shear to normal tractions (τ_{st} and σ_{st} , respectively) at the interface causes a first slip nucleation far from the edges [$\tau_{st}/\sigma_{st} > \mu_s$ marked by a circle in (a)].

details about the numerical method is given in Section 3.4. The plane-stress approximation is applied in order to represent the thin geometry of the block used in the experiments (Ben-David et al., 2010). Contact and friction is modeled with a traction-at-split-node method, as presented in Section 3.5, adapted to deformable-rigid interface problems. The material properties are Young's modulus $E = 2.6 \text{ GPa}$, Poisson's ratio $\nu = 0.37$, and density $\rho = 1200 \text{ kg/m}^3$. This is a first approximation to the properties of poly(methyl-methacrylate) (PMMA) which is an acrylic glass material also used in the experiments (Ben-David et al., 2010). These parameters result in dilatational wave speed $c_d = 1584 \text{ m/s}$ and shear wave speed $c_s = 890 \text{ m/s}$. We employ Rayleigh damping (Rayleigh, 1945; Caughey, 1960) with mass and stiffness proportionality coefficient of 0 and $0.1 \mu\text{s}$, respectively. The deformable solid is discretized by regular quadrilateral elements (with element side ranging for different meshes from 0.67 mm to 2 mm) interpolating the displacement field linearly.

A linearly distributed vertical displacement ($\bar{u}_y^1 = 0.37 \text{ mm}$, $\bar{u}_y^2 = 0.037 \text{ mm}$) is imposed at the top of the plate, as shown in Figure 5.1(a). This loading is, after reaching equilibrium, complemented by applying a uniform horizontal velocity $\bar{v}_x = 10^{-6} c_d$, where c_d is the dilatational wave speed in the deformable solid. The small value of the applied velocity ensures quasi-static loading conditions, similar to the experiments (Ben-David et al., 2010). The resulting stress distribution at the interface is nonuniform. Figure 5.1(b) is a schematic depiction of the ratio of the local tangential traction τ_{st} to the contact pressure σ_{st} . These tractions (denoted with a subscript st) are measured at the moment preceding interface rupture and

are referred to hereafter as static. The imposed loading conditions ensure a spontaneous nucleation of the slip front inside the contact interface far from the edges [indicated by a circle in Figure 5.1(a)], because this is where the non-symmetric stress distribution reaches a critical value $\tau_{st}/\sigma_{st} > \mu_s$, see Figure 5.1(b). The frictional strength is assumed to follow an exponential rate-weakening friction law. Thus, in the stick state, the tangential resistance of the interface is proportional to the contact pressure σ with a coefficient μ_s . As for the slip state, this coefficient of proportionality μ is determined by the rate-weakening friction law, as presented in Section 3.2.3. The governing equation, as given by (3.34), describes the friction coefficient μ as a function of the slip rate $\dot{\delta}$ as

$$\mu = \mu_k + (\mu_s - \mu_k) \exp\left(-\dot{\delta} \sqrt{(\mu_s - \mu_k)/\alpha}\right), \quad (5.1)$$

which ensures a smooth transition from the static μ_s to the kinetic μ_k friction coefficient governed by the transition parameter α . The parameters of the friction law are $\mu_s = 1.3$, $\mu_k = 0.6$ or 1.0 , and $\alpha = 0.1 \text{ m}^2/\text{s}^2$. The local μ_s corresponds to experimental results as reported in Figure 4(a-b) in (Ben-David and Fineberg, 2011) and is considerably higher than the global static coefficient of friction. An effect that was also observed in spring-mass simulations (Scheibert and Dysthe, 2010; Maegawa et al., 2010). The local kinetic friction coefficient as well as the transition parameter were not measured in the experiments. Therefore, they were studied here qualitatively (see first paragraph of the following section) and eventually chosen arbitrarily. When the ratio of the local tangential traction to the contact pressure exceeds the static friction threshold ($\tau_{st}/\sigma_{st} > \mu_s$), slip occurs and propagates in one or both directions along the frictional interface. The dynamics of the slip fronts are determined by the parameters of the friction law, Equation (5.1), as well as by the local stress state.

5.3 Results & Discussion

We have conducted several simulations (not all presented in this chapter) and have observed different types of slip: crack-like (the entire interface between the crack tips is slipping), pulse-like (the slip region propagates along the interface within a narrow pulse) and mixed modes when a crack converts to pulses and vice versa. The propagation speed of the slip tip v_r is related to the local stress state and seems not to depend on the type of slip. By studying the influence of the friction law parameters, we have observed that for an increasing (decreasing) difference between the static and the kinetic friction coefficients $\Delta\mu = \mu_s - \mu_k$, the slip type tends to be crack-like (pulse-like). A higher transition parameter α causes slower slip propagation especially during slip initiation and slip arrest.

In Figure 5.2, we compare our numerical results with the experimental observations of Ben-David et al. (2010) presenting the rupture speed v_r as a function of the ratio of shear to normal stress measured before slip initiation. In contrast to the experimentally reported results, we normalize the propagation speed v_r with respect to the dilatational wave speed c_d of the solid. Moreover, the local stress ratio, which was experimentally measured at finite distance

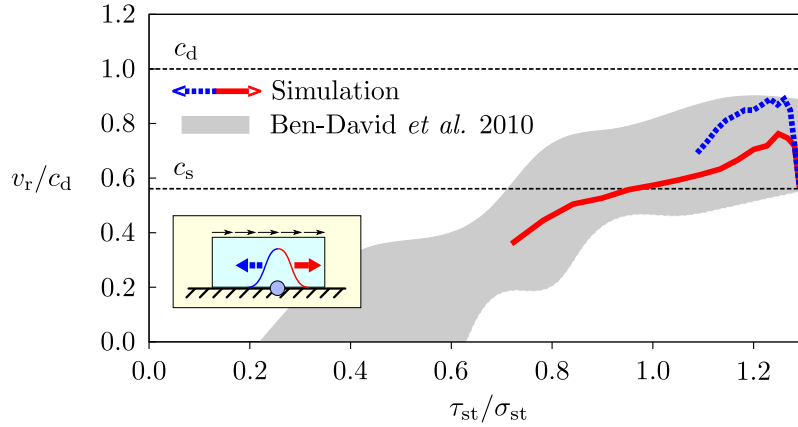


Figure 5.2: Comparison of numerical results with experimental observations by Ben-David et al. (2010). The normalized rupture speed is reported with respect to the static ratio of local tangential surface traction τ_{st} to contact pressure σ_{st} . Friction parameters are $\mu_s = 1.3$, $\mu_k = 1.0$ and $\alpha = 0.1 \text{ m}^2/\text{s}^2$

of the interface, is replaced by the local ratio of tangential traction τ_{st} to contact pressure σ_{st} measured directly at the interface. These interface tractions are referred to as static because they are measured at the moment of initiation, before propagation.

Our results confirm the experimentally (Ben-David et al., 2010) and numerically (Trømborg et al., 2011) observed general trend that the rupture propagation is faster for higher τ_{st}/σ_{st} ratios. For friction parameters $\mu_s = 1.3$, $\mu_k = 1.0$ and $\alpha = 0.1 \text{ m}^2/\text{s}^2$ the slip front speeds are in good quantitative agreement with the experimental results. Consistently with experiments (Ben-David et al., 2010), for the given type of loading (only at the top face), we do not observe slow fronts. Interestingly, we note that the rupture propagates considerably slower in the direction of the imposed shear load than in the opposite direction: in Figure 5.2 the solid red line is over the entire propagation distance below the dashed blue line, except during the initiation phase at $\tau_{st}/\sigma_{st} = 1.25 - 1.3$. These differences have not been reported in the experiments.

To enable the separation of effects due to slip directionality and any other sources that might cause a non-unique relation between the τ_{st}/σ_{st} ratio and the rupture propagation speed we consider two additional simulations, where slip events are triggered at the edges. In order to increase the propagation distance (in comparison to Figure 5.2, where the rupture propagating in the opposite direction of the imposed shear load arrests not far from the initiation zone) the kinetic coefficient of friction is reduced resulting in the following set of friction parameters: $\mu_s = 1.3$, $\mu_k = 0.6$ and $\alpha = 0.1 \text{ m}^2/\text{s}^2$. In all three cases the loading history of the body is identical up to the moment the tangential surface traction reaches the friction threshold, *i.e.*, the initial stress state is the same for all simulations (see solid line in Figure 5.5). The slip propagation is then triggered by manually increasing the local tangential surface traction

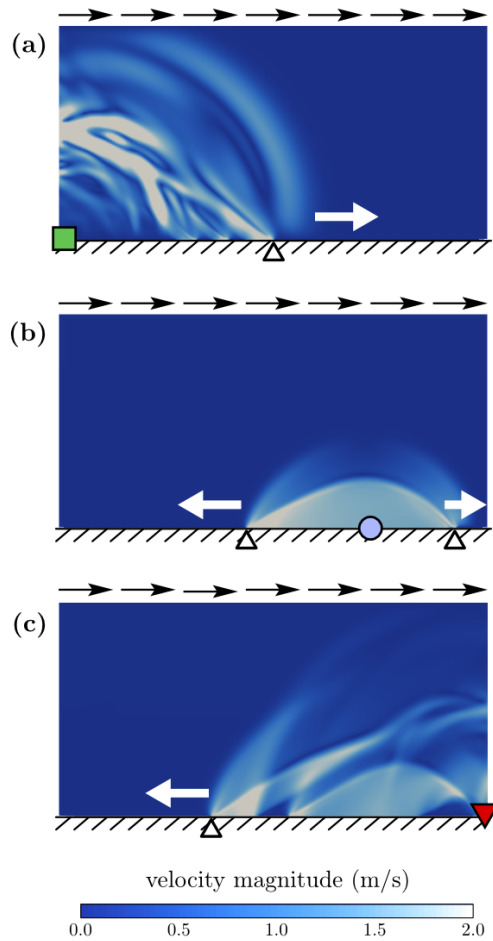


Figure 5.3: Three different slip events are presented for the same initial stress state (before triggering or spontaneous initiation). Instantaneous material velocity is shown for the slip event (a) triggered at the left edge, (b) spontaneously initiated far from the edges and (c) triggered at the right edge. Colors from blue to white denote material velocities ranging from 0 m/s to 2 m/s, respectively. The starting point of each event is marked with a square, a circle and a triangle, respectively. Small white triangles show the location of the tip of the slip front. Black arrows indicate the direction of the imposed global shear load, whereas white arrows show the direction of the rupture propagation.

within small nucleation zones at the edges. The velocity field within the bulk of the solid is shown for these two simulations in Figure 5.3(a,c). The green square and the red triangle indicate the left and right triggering positions, respectively. The small white triangle indicate the current position of the front tip and the white arrows the direction of propagation. In a third simulation, the global shear load is slightly increased and rupture nucleates spontaneously far from the edges as for the reference simulation reported in Figure 5.2. The velocity field in the bulk of the solid for this case is shown in Figure 5.3(b) with the blue point indicating the position of spontaneous initiation.

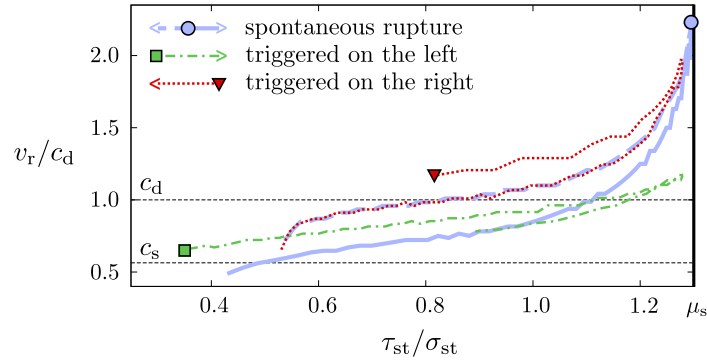


Figure 5.4: The normalized rupture speed for the three slip fronts shown in Figure 5.3 is depicted with respect to the local static ratio of tangential traction τ_{st} to contact pressure σ_{st} (data close to the triggering zone are not shown). All three slip fronts propagate along an interface with the same initial stress state (before triggering or spontaneous initiation). The solid blue line is the result of the spontaneously initiated rupture far from the edges, the dashed-dotted green line for the front triggered at the left edge and the dotted red line for the rupture triggered at the right edge. Friction parameters are $\mu_s = 1.3$, $\mu_k = 0.6$ and $\alpha = 0.1 \text{ m}^2/\text{s}^2$

Figure 5.4 presents the normalized rupture speed with respect to the static interface traction ratio τ_{st}/σ_{st} . The spontaneously initiated slip front, shown in Figure 5.4 by a solid blue line, starts at $\tau_{st}/\sigma_{st} = \mu_s$, indicated by the same blue point as in Figure 5.3(b), and propagates fast toward the edges. The front speed decreases along the path with decreasing ratio τ_{st}/σ_{st} . Note that under some conditions we observe super-sonic slip fronts, which were not observed in (Ben-David et al., 2010). However, our results are consistent with rupture in bi-material interfaces where the stiffer material limits the propagation speed as observed experimentally and numerically by Coker et al. (2003).

The two edge-triggered ruptures depart at lower τ_{st}/σ_{st} levels than the spontaneously initiated front. The start positions are indicated by the same square and triangle as in Figure 5.3(a,c). While during the initiation these slip fronts propagate relatively slowly, they accelerate continuously until reaching a maximum value for maximal ratio τ_{st}/σ_{st} , and finally decelerate. Although the triggered ruptures are unidirectional, there is no unique slip tip speed associated with a given τ_{st}/σ_{st} value along their propagation path. In addition, comparing the three different slip fronts, one can see that the maximal rupture velocity of the left-triggered rupture does not exceed 60% of the maximal speed for the other two cases for the same static ratio τ_{st}/σ_{st} .

As seen best in Figure 5.3(a), the slip front (marked by a small white triangle) propagating at super-shear velocity follows the dilatational wave (the circular white zone furthest from the nucleation zone), which modifies the local stress state at the interface. Therefore, looking at the dynamic ratio τ_{dy}/σ_{dy} measured in front of the rupture tip, instead of examining the static ratio τ_{st}/σ_{st} , would allow to account for the dynamic nature of the slip propagation.

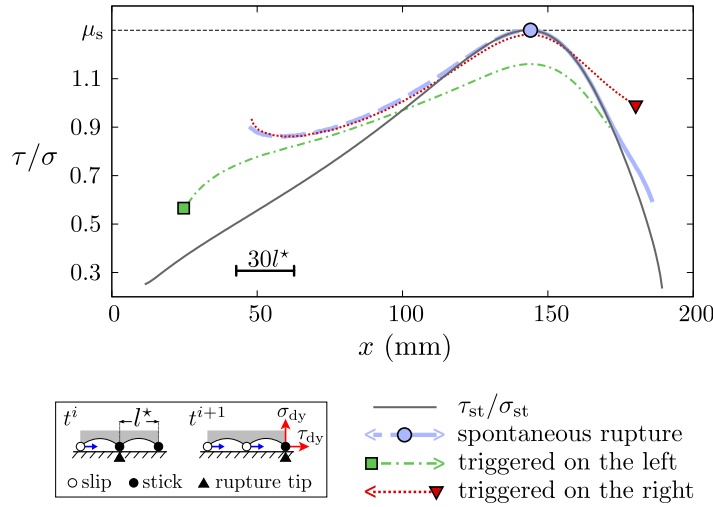


Figure 5.5: For each point along the interface x the dynamic stress ratio τ_{dy}/σ_{dy} is plotted at the moment when the slip front arrives at this location. Note that contrary to the reported static stress ratio τ_{st}/σ_{st} , this is not an instantaneous picture but an assembly of results over the entire time of propagation. Data close to the triggering zones are omitted. **(Inset)** The dynamic values τ_{dy} and σ_{dy} are measured at the sticking node in front of the slipping region at the moment t^{i+1} when the previous node starts to slip

Here, the location of the slip tip is determined to coincide with the position of the sticking node in front of the slipping nodes, as illustrated in the inset of Figure 5.5. According to this definition, the position of the rupture tip changes abruptly when the front advances. However, its velocity is computed in a continuous way as $v_r = l^*/\Delta t$, where l^* is a characteristic distance (here $l^* = 0.67$ mm) and Δt is the time interval that the rupture needs to advance this distance.

In the context of discrete contact, we propose to analyze an instantaneous dynamic stress state (τ_{dy} and σ_{dy}) at the slip tip right after it jumps to a new position, as illustrated in the inset of Figure 5.5]. The dynamic ratio τ_{dy}/σ_{dy} differs significantly from the static one, as shown in Figure 5.5. It is changed by the dilatational wave often preceding the slip front. It is also worth noting that the value of the dynamic ratio is far from the critical value μ_s for a large part of the propagation path, which implies the need for a strong change of the stress state at the rupture tip within a short time.

The relation between the speed of the slip front and the dynamic ratio τ_{dy}/σ_{dy} is depicted in Figure 5.6. Compared to Figure 5.4, the rupture triggered on the left is in better agreement with the other two (faster) slip fronts. Particularly, the slopes are more consistent for all curves and the range of velocities is smaller for a given ratio τ_{dy}/σ_{dy} . Again it is confirmed that the character of the slip propagation is directionality dependent. For a given ratio τ_{dy}/σ_{dy} , the slip fronts propagating in the direction opposite to the sliding are faster than the oncoming fronts. In Figure 5.6, the dotted red curve of the left-propagating front is always above the

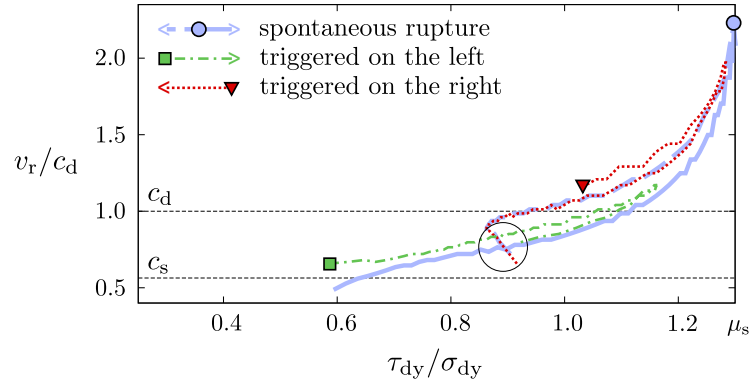


Figure 5.6: The normalized rupture speed is plotted with respect to the dynamic traction ratio τ_{dy}/σ_{dy} for the same three slip events shown in Figures 5.3 and 5.4. The slip front of the solid blue line spontaneously initiated far from the interface edges, whereas the green and red curves are ruptures artificially triggered at the left and right edge, respectively. Data close to the triggering zones are omitted.

dashed-dotted green curve of the right-propagating rupture. Nonetheless, the difference between the curves cannot be only attributed to the directionality because the two branches of the dotted red curve in Figure 5.6 are not superposed, nor are the two branches of the dashed-dotted green curve. The accelerating slip fronts show a faster rupture velocity than the decelerating ones for the same given ratio τ_{dy}/σ_{dy} . Further, the general trend of faster rupture for higher τ/σ is lost (enclosed by the large circle in Figure 5.6); at a certain moment, the rupture speed starts to decrease rapidly with increasing τ_{dy}/σ_{dy} along the propagation path. We observe this phenomenon only for slip fronts advancing against the sliding direction. Regardless of the simplicity of the static criterion τ_{st}/σ_{st} and the consistency of the dynamic criterion τ_{dy}/σ_{dy} , a stress ratio does not seem able to provide a fully reliable estimation of the velocity of the slip propagation.

The lack of generality of the speed criteria based on the ratio of the tangential traction to the contact pressure τ/σ suggests an independent consideration of τ and σ . It was proposed (Ben-David et al., 2010) that the propagation of the slip front is related to the energy densities \tilde{U}_s , stored at the front tip, and \tilde{U}_r , needed to advance the slip front. We propose a heuristic energy density at the contact interface as

$$\tilde{U}(\sigma, \tau) = (2(1 + \nu)\tau^2 + \sigma^2) / 2E. \quad (5.2)$$

The density of stored energy $\tilde{U}_s = \tilde{U}(\sigma_{dy}, \tau_{dy})$ is measured locally at the slip tip at the moment the front advances one length parameter l^* , similarly to the dynamic ratio τ_{dy}/σ_{dy} . The density of rupture energy $\tilde{U}_r = \tilde{U}(\sigma_u, \mu_s \sigma_u)$ is computed at the same material point just before the front advances another l^* , *i.e.*, when the ratio of tangential traction to contact pressure reaches the static coefficient of friction ($\tau_u/\sigma_u = \mu_s$), as illustrated by the inset of Figure 5.7.

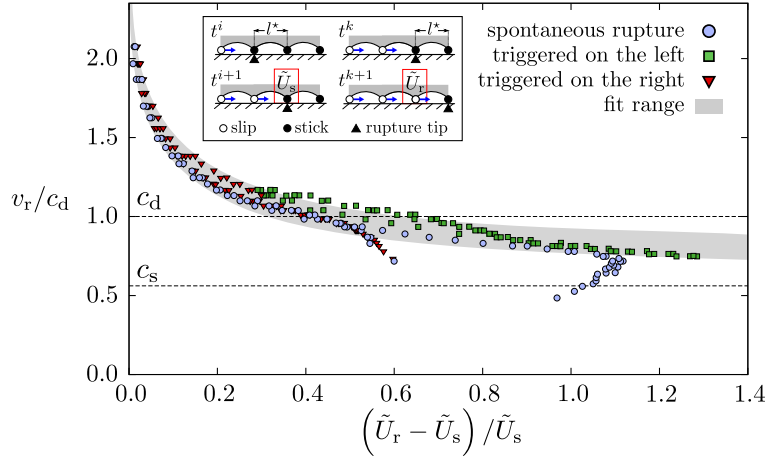


Figure 5.7: The normalized rupture velocity is shown with respect to a dynamic criterion based on a heuristic surface energy density \tilde{U} . The ratio $(\tilde{U}_r - \tilde{U}_s)/\tilde{U}_s$ represents the proportion of the energy change $\tilde{U}_r - \tilde{U}_s$ at the slip tip needed to advance the rupture front with respect to the locally stored energy \tilde{U}_s . The gray area is a data fit based on Equation (5.3) with $a = 0.76 \pm 0.07$, $b = 1.80$ and $c = 3.05$. **(Inset)** \tilde{U}_s and \tilde{U}_r are measured when the slip tip, respectively, reaches the observation point and overpasses it

The normalized rupture speed is shown in Figure 5.7 as a function of the change of the energy density at the slip tip $\Delta\tilde{U} = \tilde{U}_r - \tilde{U}_s$ normalized by the stored energy density \tilde{U}_s . The data of all three cases collapse within a narrow region properly described by

$$v_r/c_d = a + b \exp(-c \sqrt{\Delta\tilde{U}/\tilde{U}_s}), \quad (5.3)$$

where a , b and c are fitting parameters (see Figure 5.7). No differences due to the directionality of the slip propagation nor any other reason that caused branching for the previously studied criteria are now present. This shows that the energy density criterion is able to account for the dynamics of slip events at bi-material interfaces. Note that tails of data points falling outside of the fit range occur when the slip fronts start to decelerate rapidly before arresting.

5.4 Conclusion

In this chapter, it was demonstrated that the static ratio of shear to normal stress (Ben-David et al., 2010; Trømborg et al., 2011) is not a sufficient criterion for determining the speed of slip fronts. The use of the dynamic ratio, measured in front of the slip tip, improves the estimation of this speed. However, for our set-up we observed that, given a stress ratio (static or dynamic), the front going in the direction of the sliding is always slower than the front propagating in the opposite direction. Moreover, the decelerating fronts are also slower than the accelerating ones. The energetic criterion we proposed, eliminates these effects and highlights the similarities between the rupture of frictional interfaces (Coker et al., 2005) and crack propagation (Coker

et al., 2003). We hope that these findings motivate experimental work to access dynamic stress field measurements as well as theoretical studies to extend the principles of fracture mechanics to problems of frictional sliding.

6 Predicting the Propagation Distance of Frictional Slip

Slip fronts propagating at frictional interfaces may stop naturally before reaching the edges. In particular, series of arresting slip fronts with periods of sticking in between appear systematically in systems with highly concentrated shear loads. In this chapter, we study the arrest of frictional shear fronts with numerical and theoretical models. First, we compare the slip front behavior produced by a dynamic finite-element simulation with experimental data. Further, in order to get more insights on the fundamental aspects of frictional slip, we develop a theoretical model based on linear elastic fracture mechanics and analyze the influence of various interface and material parameters. By showing that the prediction of the theoretical model is in good quantitative agreement with experimental data, we provide evidence to recognize frictional slip as a fracture phenomenon.

This chapter is a modified version of a scientific article currently under review as:

D.S. Kammer, M. Radiguet, J.-P. Ampuero, J.F. Molinari, “Linear elastic fracture mechanics predicts the propagation distance of frictional slip”, *Tribology Letters*, submitted, 2014.

This work resulted also in the discovery of viscoelastic effects that lead to the survival of stress concentrations at frictional interfaces and was published in the following scientific articles:

M. Radiguet, D.S. Kammer, Ph. Gillet, J.F. Molinari, “Survival of Heterogeneous Stress Distributions Created by Precursory Slip at Frictional Interfaces”, *Physical Review Letters*, 111:164302, 2013.

M. Radiguet, D.S. Kammer, J.F. Molinari, “The role of viscoelasticity on heterogeneous stress fields at frictional interfaces”, *Mechanics of Materials*, in press, 2014.

6.1 The Propagation of Slip Precursors

Recent laboratory experiments have shown that nominally flat interfaces between solids under a localized quasi-static shear load may present local slip precursors well before global sliding (Rubinstein et al., 2007; Maegawa et al., 2010). These findings on the transition from sticking to sliding have attracted wide attention (Scheibert and Dysthe, 2010; Trømborg et al., 2011; Bouchbinder et al., 2011; Amundsen et al., 2012; Otsuki and Matsukawa, 2013). In the experiments, two poly(methyl-methacrylate) (PMMA) blocks are brought into contact under a constant normal load F_N . A shear load F_s is applied to the top block (slider) via a pusher located close to the interface. In this side-driven set-up, which is schematically illustrated in Figure 6.1(a), local slip fronts nucleate episodically at the trailing edge and propagate over parts of the interface. Their propagation distance increases proportionally to the applied load until approximately the middle of the interface. From this point on, the growth of the precursors is considerably faster (*e.g.*, see experimental data of Rubinstein et al. (2007) shown in Figure 6.5). Once a slip event propagates over the entire interface, global sliding occurs.

The remarkable increase of precursor lengths and its non-linear relation to the applied shear force F_s was shown to be highly reproducible and, if normalized by sample length and normal force, unique and independent of the slider geometry (length or height), of the normal load, and of the pusher position (Rubinstein et al., 2007; Trømborg et al., 2011). In essence, episodic nucleation and spontaneous arrest of precursor fronts arise from the spatial concentration of interface stresses induced by the applied load (Rubinstein et al., 2008). Several numerical models, one-dimensional spring-mass chains with arbitrary normal loads (Maegawa et al., 2010; Amundsen et al., 2012) as well as two-dimensional spring-mass models (Trømborg et al., 2011), were proposed to simulate the mechanics of precursors and to analyze the relation between the normalized precursor length and the measured macroscopic force ratio F_s/F_N . They confirmed experimental observations showing the absence of influence of the slider geometry and produced non-linear evolution of the precursor length. However, none of these numerical simulations provided quantitative comparison to experimental data. The main reasons being inconsistent interface stresses due to the discrete nature (Maegawa et al., 2010; Trømborg et al., 2011; Amundsen et al., 2012) or the one-dimensional geometry (Maegawa et al., 2010; Amundsen et al., 2012) of these models.

In addition to numerical models, only few theoretical approaches have been proposed so far. A quasi-static one-dimensional model (Scheibert and Dysthe, 2010) applied a simplified stress criterion, inspired by Griffith's energetic criterion, to study the kinematics of the transition from static to stick-slip friction, and showed that it is dominated by the system instead of the small scale parameters. Another analytical model (Amundsen et al., 2012) applied a reverse approach. Given a precursor length, they describe the interface stresses after precursor arrest and compute the associated macroscopic shear force by integration of the interface shear tractions. Even though these theoretical models offer interesting intuition about the propagation length of precursors, they do not give new insights about the mechanics of friction nor do they provide quantitative comparison with experiments. There are several causes to

this discrepancy. As for the numerical simulations, the one-dimensional geometry and the arbitrary initial stress states can result in inconsistent predictions. Moreover, the simplistic propagation criteria, and the use of post-precursor instead of pre-precursor stress states are additional limitations of existing models.

In this chapter, we first present a numerical model for the dynamic simulation of frictional slip in a set-up comparable to the experimental system of Rubinstein et al. (2007). We show that this model produces sequences of precursors and compare the results with experimental data. Further, we present a theoretical model based on Linear Elastic Fracture Mechanics (LEFM) that predicts the kinematics of slip precursors at frictional interfaces. Such LEFM approaches have long been used in earthquake modeling (Freund, 1979; Ampuero et al., 2006; Kato, 2012), and recently, experimental evidence was provided by measurements of LEFM strain fields around Sub-Rayleigh slip fronts (Svetlizky and Fineberg, 2014). We here develop this concept into a quantitative model that incorporates the continuum approach of linear elastic fracture mechanics as well as interface stress states resulting from the exact system geometry. The aim of this model is to be as simple as possible while comprising the essential features of fracture mechanics theory and addressing the shortcomings of previous theoretical models. With this approach, we study the link between meso-scale properties and the macro-scale response of a solid-body system containing a frictional interface. Friction mechanisms acting at even smaller scales (*i.e.*, atomic scale) are incorporated in a local (meso-scale) friction law.

Specifically, we use real interfacial stress states from a two-dimensional geometry to provide a prediction of the precursor length based on the shear load measured before the slip event and compare our results quantitatively with experimental data. In addition, we analyze the influence of several material and interface parameters, which has not been done before, and point out various sources of the precursor length non-linearity. This analysis is further extended by considering simplifications of our model which provide a fundamental understanding of the origin of the non-linearity of the precursor length evolution.

6.2 Models

Following Rubinstein et al. (2007), we study friction in a system consisting of a rectangular thin plate of length $L = 200$ mm, height $H = 75$ mm and thickness $W = 6$ mm, in contact with a much thicker deformable base block of dimension $300 \times 30 \times 27$ mm. A pusher of width $w_p = 5$ mm is applied at height $h_p = 6$ mm from the interface. The material properties are assumed to be viscoelastic, with Poisson's ratio ν , viscous E_v and static E_∞ Young's moduli. The resulting instantaneous Young's modulus is given by $E_0 = E_v + E_\infty$. A linear slip-weakening friction law (Palmer and Rice, 1973; Andrews, 1976a), as introduced in Section 3.2.3, is applied at the interface, describing the frictional strength as

$$\tau^s(\delta, x) = \begin{cases} [\mu_s + \delta/d_c (\mu_k - \mu_s)] \sigma(x) & \text{for } \delta < d_c \\ \mu_k \sigma(x) & \text{for } \delta \geq d_c, \end{cases} \quad (6.1)$$

Chapter 6. Predicting the Propagation Distance of Frictional Slip

where μ_s and μ_k are the static and kinetic friction coefficients, d_c is the characteristic weakening length, δ is the local interface slip, $\sigma(x)$ is the contact pressure, and x is the coordinate along the interface. More advanced friction laws, such as velocity-weakening-strengthening friction, have been used in the past to model precursor mechanics at PMMA interfaces (Braun et al., 2009; Bouchbinder et al., 2011; Bar Sinai et al., 2012; Bar-Sinai et al., 2014). Even though these models describe well the propagation of frictional slow fronts, they are not indispensable to model the propagation distance of precursors, as shown with dynamic finite-element simulations using slip-weakening friction (Radiguet et al., 2013). Here, the emphasis is on simplicity and the slip-weakening friction law enables simple determination of the interface's fracture toughness, which is essential to LEFM theory.

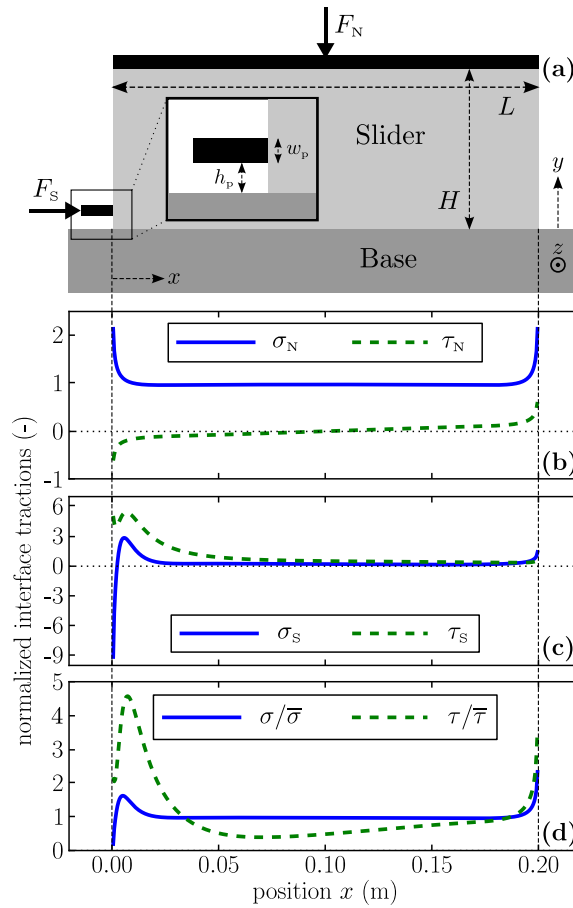


Figure 6.1: **(a)** Set-up of the side-driven system. A thin slider is pressed by a constant normal load F_N onto a thicker base block. A pusher applies a slowly increasing shear load F_S to the slider. **(inset)** Zoom on the pusher. **(b)** Static stress state at the interface for an applied normal load. Note the convention of positive σ for compression. **(c)** Static stress state at the interface for an applied unit shear load. **(d)** Interface stresses for an unruptured linear combination of both loadings with $F_N = 5F_S$ and normalized by the average interface stress.

The material as well as interface parameters are chosen in order to correspond best to the properties of PMMA. The viscoelastic material parameters are based on experimental measurements (Read and Duncan, 1981; Ciccotti and Mulargia, 2004; Svetlizky and Fineberg, 2014) and are chosen as $E_\infty = 2.6 \text{ GPa}$, $E_V = 3.0 \text{ GPa}$, $\nu = 0.37$, and $\rho = 1200 \text{ kg/m}^3$. The interface parameters are difficult to measure and are therefore estimated as well as possible from experimental observations (Rubinstein et al., 2007; Ben-David et al., 2010; Svetlizky and Fineberg, 2014). The values applied for this studies are $\mu_s = 0.9$, $\mu_k = 0.45$, and $d_c = 1 \mu\text{m}$. The effect of the parameter choice on the precursor load-length relation is studied in Section 6.3.2. The normal load of $F_N = 3300 \text{ N}$ applied in the experiments of Rubinstein et al. (2007) is adopted for all results shown in this chapter.

6.2.1 Numerical Model

The numerical model used for dynamic simulations of precursors is the same as presented by Radiguet et al. (2014), but with adapted geometry as well as material and interface properties. It is a two-dimensional finite-element model with an explicit Newmark β -method for time integration and a traction-at-split-node technique to model the frictional interface. More details about the numerical methods are given in Sections 3.4 and 3.5. The solids are discretized by regular quadrangular meshes and convergence with respect to the element size is verified.

With the objective of mimicking closely the experimental set-up, the thin slider is approximated with plane-stress assumption whereas the much thicker base block is modeled with a plane-strain approximation. The bottom edge of the base block is fixed and the external shear loading is applied at a constant loading rate $\bar{v}_x = 2.5 \text{ mm/s}$ through a spring of stiffness $K_s = 1 \text{ GN/m}^2$ and a rigid pusher.

The viscoelasticity of the bulk material is modeled by the standard linear solid approach. It is particularly well suited to represent polymeric materials, if the viscous property is only applied to the deviatoric part of the stress-strain relation. A detailed description of this constitutive law is given in Section 3.1.4. The evolution of the stress-strain relation is governed by the viscosity parameter η , which introduces the time scale of stress relaxation. For computational reasons, the viscosity is chosen as $\eta = 5 \text{ MPa}\cdot\text{s}$, which results in considerably faster relaxation times than realistic material properties. However, the relaxation time is still much longer than the typical duration of an interface rupture and has therefore no effect on the propagation distance of the precursors.

In the dynamic simulations, the linear slip-weakening friction law is regularized by a simplified Prakash and Clifton (1993b) law similar to the regularization studied in Chapter 4. The effective frictional strength is governed by

$$\frac{d\tau^{\text{es}}}{dt} = \frac{\tau^s - \tau^{\text{es}}}{t_{\text{pc}}}, \quad (6.2)$$

where $t_{\text{pc}} = 50 \mu\text{s}$ is the characteristic time of the regularization. This is a further simplification

of the regularization given by Equation (4.1), where the slip-rate dependence is eliminated. This simplified version still contains the essential features of the original regularization, which is the non-instantaneous adjustment to a change in the contact pressure, but limits the number of additional parameters to a minimum.

6.2.2 Theoretical LEFM Model

The unruptured tractions at the interface are computed by static finite-element simulations. An applied unit normal load leads to a normal $\sigma_N(x)$ traction satisfying the following condition $W \int_0^L \sigma_N(x) dx = 1$ N. The resulting contact pressure, as shown in Figure 6.1(b), is approximately uniform in the central 80% of the interface and presents singularities at the edges due to the perfect rectangular shape of the specimen. Poisson's lateral expansion is frustrated at the interface by the frictional strength leading to a shear traction $\tau_N(x)$, which is approximately linear and symmetric with respect to the center point of the interface. Similarly, $\sigma_S(x)$ and $\tau_S(x)$ result from an applied unit shear load and satisfy therefore $W \int_0^L \tau_S(x) dx = 1$ N. As shown in Figure 6.1(c), $\tau_S(x)$ presents a maximum close to the trailing edge, which will eventually lead to the initiation of precursors.

It is important to note that although the unruptured interface tractions are computed by static finite-element simulations, the following model is theoretical and independent of numerical simulations. Any interface stress state, also experimental data, could be used as starting point for our model.

Once the unruptured interface tractions, caused by external loadings, are known, the effective interface tractions are then modeled by linear superposition of these tractions and the stress drops due to previous interface ruptures. The normal $\sigma_r(x)$ and shear $\tau_r(x)$ tractions after $r - 1$ precursors, for any F_N and F_S , and after viscous relaxation are given by

$$\sigma_r(x) = \tilde{F}_N \sigma_N(x) + \tilde{F}_S \sigma_S(x) \quad (6.3)$$

$$\tau_r(x) = \tilde{F}_N \tau_N(x) + \tilde{F}_S \tau_S(x) + \frac{E_\infty}{E_0} \sum_{i=1}^{r-1} \Delta \tau_i(x), \quad (6.4)$$

with \tilde{F}_N and \tilde{F}_S ensuring that the macroscopic normal and shear loads are always equal to F_N and F_S , e.g., $W \int_0^L \sigma_r(x) dx = F_N$ and $W \int_0^L \tau_r(x) dx = F_S$. The change in the shear tractions caused by interface rupture i is introduced as $\Delta \tau_i(x)$, while contact pressure changes are neglected. As shown by Radiguet et al. (2013, 2014), the bulk material's viscoelasticity results in a partial restitution of pre-rupture shear tractions. The time scale of this viscous effect (given by η) is not explicitly incorporated in this model because the relaxation time is considerably longer than the duration of a single precursor, but shorter than the time between two slip events. As a consequence, the stress drops is multiplied by E_∞/E_0 in order to account for the viscoelastic restitution. Furthermore, a non-adhesion condition defines that where $\sigma_r(x) < 0$ we impose: $\sigma_r(x) = 0$ and $\tau_r(x) = 0$. An example of an effective stress state without a stress drop is shown in Figure 6.1(d). The contact pressure is rather uniform, while the shear traction

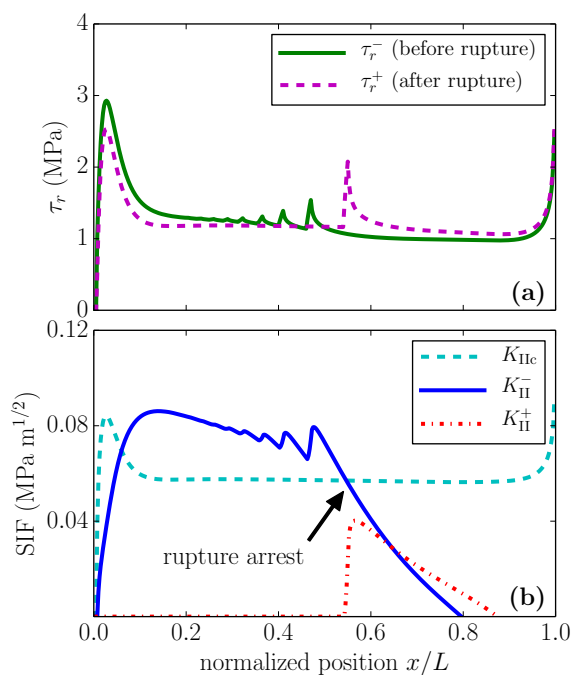


Figure 6.2: **(a)** Interfacial shear tractions before and after an interface rupture, given by Equation (6.4) for $r = 13$. **(b)** Fracture toughness K_{IIc} and stress intensity factor K_{II}^- (before) and K_{II}^+ (after) the rupture shown in (a).

presents an important peak close to the trailing edge, which is at the origin of slip nucleations.

Considering local slip events as interface ruptures, we model their propagation using LEFM (Freund, 1990), which implies that every rupture modifies the stress state of the interface behind as well as ahead of its tip. An example of how shear tractions change during a slip event is shown in Figure 6.2(a) for a rupture with arrest position $x/L = 0.55$. The shear tractions before and after an interface rupture (in time) are denoted with a superscript $-$ and $+$, respectively. The arrest of the precursor creates a peak at $x/L = 0.55$, and a square root decrease in shear tractions for $x/L > 0.55$ (see τ_r^+). The peaks in τ_r^- at $x/L = 0.3 - 0.5$ are the remains of stress concentrations of previous precursors. After the current rupture, they are erased due to the linear slip-weakening friction law (see τ_r^+) and will partially reappear over time. This effect was shown to be the result of the bulk's viscoelasticity (Radiguet et al., 2013, 2014).

The tractions before and after the rupture r are linked by the stress change $\Delta\tau_r(x)$ through $\tau_r^+(x) = \tau_r^-(x) + \Delta\tau_r(x)$. The stress τ_r^- is equal to $\tau_r(x)$, given by Equation (6.4), for F_N and F_S at the time of the rupture. The stress $\tau_r^+(x)$ is the result of the rupture and can be separated into three different areas as described below.

At the rupture tip, there is a process (weakening) zone, where $\delta < d_c$ and in which the shear traction drops from the static frictional strength $\tau^s(0, x)$ to the kinetic strength $\tau^s(d_c, x)$. A linear

Chapter 6. Predicting the Propagation Distance of Frictional Slip

slip-weakening friction law results, within the process zone, in a non-linear shear traction distribution, which, for reasons of simplicity, is here approximated by a linear function. The size of a static linear process zone is given by $w_{pz} = 9\pi K_{II}^2(l) / [32\sigma_r^2(l)(\mu_s - \mu_k)^2]$ (Palmer and Rice, 1973), where l is the arrest position of the precursor and K_{II} the mode II stress intensity factor. The leading end of the process zone is at $x = l_a$ and the trailing end at $x = l_a - w_{pz} = l_b$. The position l_a of the leading end is determined by the stress concentration as defined below, which always results in a process zone that satisfies $l_b < l < l_a$.

Behind the process zone, the stress state is imposed by the friction law, Equation (6.1). Because $\delta > d_c$ everywhere, we can write $\tau_r^+(x) = \tau^s(d_c, x) = \mu_k \sigma_r(x)$ for $x < l_b$.

Ahead of the slip event appears a stress concentration caused by the stress drop occurring behind the rupture tip. The stress change ahead is given in first order approximation as $\Delta\tau_r(x) \approx K_{II}(l) / \sqrt{2\pi(x-l)}$. Because frictional rupture does not allow for stress singularities, the frictional strength limits the maximal shear traction, similar to the assumption of a small plastic zone size in fracture mechanics. Therefore the position of the leading end of the process zone is determined such that $\mu_s \sigma_r(l_a) = \tau_r^-(l_a) + K_{II}(l) / \sqrt{2\pi(l_a - l)}$.

This is only a simplified approximation to the correct description of the stress state around a cohesive crack. In fact, the details have no significant effect on the precursor load-length relation studied here, and even neglecting entirely the process zone results in virtually the same observations with isolated shorter slip events that do not affect the load-length relation of the expanding precursors.

The stress change caused by an interface rupture can therefore be summarized as

$$\Delta\tau_r(x) = \begin{cases} \frac{K_{II}(l)}{\sqrt{2\pi(x-l)}} & \text{for } x \geq l_a \\ \Delta\tau_r(l_b) + \frac{x-l_b}{w_{pz}} \Delta\tau_{pz} & \text{for } l_b < x < l_a \\ \mu_k \sigma_r(x) - \tau_r^-(x) & \text{for } x \leq l_b, \end{cases} \quad (6.5)$$

with $\Delta\tau_{pz} = \Delta\tau_r(l_a) - \Delta\tau_r(l_b)$. The process zone is characterized by l the arrest position of the rupture, l_a and l_b the leading and trailing end, respectively, and $w_{pz} = l_a - l_b$ the process zone size.

The mode II stress intensity factor for a non-uniform shear stress drop $\Delta\tau_r$ along an edge crack of length a in a semi-infinite solid can be deduced from Equation (8.3) in Tada et al. (2000) by integration:

$$K_{II}(a) = \frac{2}{\sqrt{\pi a}} \int_0^a \frac{\Delta\tau_r(s) F(s/a)}{\sqrt{1-(s/a)^2}} ds \quad (6.6)$$

with $F(s/a) = 1 + 0.3(1 - (s/a)^{5/4})$ and $\Delta\tau_r(s) = \mu_k \sigma_r(s) - \tau_r^-(s)$ because the integration is along the crack interface and the process zone is neglected. A different possible choice of stress intensity factor is a semi-infinite crack approaching the edge of a semi-infinite solid [Equation (9.5) in Tada et al. (2000)]. On the studied system, this stress intensity factor leads to an almost

identical precursor load-length relation as in the model with Equation (6.6). Only a slightly steeper curve at $l/L > 0.5$ is observed (not shown here). As $\Delta\tau_r$ is multiplied by the non-linear factor $F(s/a)/\sqrt{1-(s/a)^2}$ over the crack face, the stress intensity factor is one possible source of non-linearity in precursor mechanics.

Given that the slider is a thin plate, the fracture toughness is computed in the plane-stress approximation with the frictional fracture energy Γ_c by:

$$K_{\text{IIC}}(x) = \sqrt{E_0 \Gamma_c(x)} = \sqrt{E_0 \frac{(\mu_s - \mu_k) d_c}{2} \sigma_r(x)}. \quad (6.7)$$

The fracture toughness is computed using E_0 because the characteristic frictional weakening time is significantly smaller than the relaxation time of the viscoelastic material (Rice, 1979).

Neglecting any dynamic effect, the precursor length l for a given stress state of the interface is determined by the position at which the stress intensity factor becomes smaller than the fracture toughness:

$$K_{\text{II}}^-(l) = K_{\text{IIC}}(l) \quad \text{and} \quad \frac{dK_{\text{II}}^-(l)}{dx} < \frac{dK_{\text{IIC}}(l)}{dx}. \quad (6.8)$$

An example is shown in Figure 6.2(b). The stress intensity factor right after an event K_{II}^+ is significantly lower than K_{IIC} , hence a finite load increment is required to nucleate the next precursor event.

Up to this point, we presented how the precursor length can be predicted for any given interface stress state. In order to complete the proposed model, we need to determine the shear force at which a slip event is expected. As the initiation of the rupture occurs at the trailing edge of the system and a rupture only propagates where the stress intensity factor is larger than the fracture toughness, we introduce a length scale l_n which represents the size of the nucleation zone and define that the next precursor occurs when the following condition is satisfied:

$$K_{\text{II}}^-(l_n) = K_{\text{IIC}}(l_n) \quad \text{and} \quad \frac{dK_{\text{II}}^-(l_n)}{dx} > \frac{dK_{\text{IIC}}(l_n)}{dx}. \quad (6.9)$$

The slip nucleation zone size l_n acts like a seed crack to the propagation of an interface rupture and can be thought of as the stable slip zone that occurs before dynamic ruptures (Uenishi and Rice, 2003; Garagash and Germanovich, 2012). Its size may vary from one to another slip event, but is chosen to be constant in our model. However, testing different values for l_n has shown that below a critical length, it has only a negligible influence on the precursor load-length relation. Decreasing l_n only leads to slightly less precursors. In this work, we chose $l_n = 0.012$ m, which is below the critical length and results in approximately the same precursor occurrence frequency as in the experiment of Rubinstein et al. (2007).

Before comparing our model with experimental data and studying the influence of various

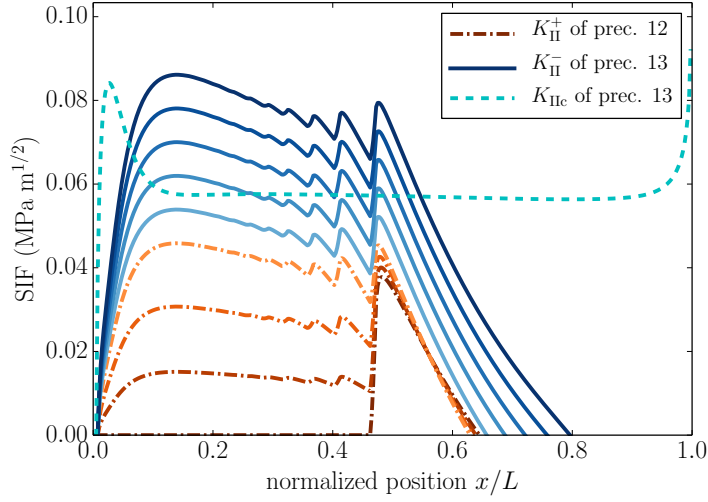


Figure 6.3: The evolution of the stress intensity factor is shown during the period between two precursors. Directly after precursor 12, the stress intensity factor K_{II}^+ is zero along the interface and non-zero ahead of the arrest position, as shown by the dash-dotted dark orange curve. Viscous relaxation of the bulk material, illustrated by the dash-dotted orange curves going from dark to bright, leads to a partial recovery of the pre-rupture stress intensity factor. Further, the increasing external shear load lifts continuously the stress intensity factor, as shown by the solid blue curves going from bright to dark. When the area of $K_{II}^- > K_{IIC}$ reaches the slip nucleation zone characterized by $x \leq l_n = 0.06L$, the next precursor propagates. For simplicity, the effects of the viscous relaxation and the external loading are here illustrated sequentially. In reality, they occur simultaneously. However, if complete relaxation occurs between two precursors, the sequential and simultaneous approaches are equivalent.

parameters, we here summarize the events occurring during a cycle of an interface rupture in order to provide the reader with a basic intuition of the observed phenomenon. Considering an interface stress state at which a slip event occurs [e.g. Figure 6.2(a)], a rupture propagates from the trailing (left) edge until a point where the stress intensity factor becomes smaller than the fracture toughness [Equation (6.8) and Figure 6.2(b)]. Behind the rupture occurs a stress drop and ahead of the tip a stress concentration as described by Equation (6.5). The stress concentrations of previous ruptures are erased because behind the process zone the friction law imposes shear tractions that depend only on the kinetic friction coefficient and the contact pressure. The viscous memory effect of the bulk material restores these concentrations partially over time (Radiguet et al., 2013). Directly after the rupture and before viscous relaxation, the stress intensity factor is zero along the interface up to the arrest position (see K_{II}^+ in Figure 6.2(b) and Figure 6.3). Thus, additional external shear loading is needed to reach a new interface stress state that allows for the propagation of a slip event. While the external loading increases, the stress intensity factor exceeds the fracture toughness first, for this particular set-up, at approximately $x/L = 0.15$ and short after at a position close to the last arrest position (see Figure 6.3). Nevertheless, no rupture initiates because the

shear traction is still below the static strength, $\tau_r(x) < \tau^s(0, x)$ (at the last arrest position due to viscous relaxation), and the stress intensity factor should be higher than the fracture toughness starting from the edge (and not solely in the middle of interface). For even higher external shear loads, the area with $K_{II}^- > K_{IIC}$ expands and once it reaches the seed crack at the edge, and satisfies Equation (6.9), a new slip event occurs and the cycle starts over again.

6.3 Results and Discussion

6.3.1 Numerical Simulations

The results of a numerical simulation based on the model presented in Section 6.2.1 are shown in Figure 6.4. The macroscopic shear to normal force ratio increases quasi-linearly with small force drops occurring at a regular interval until macroscopic sliding takes place at approximately $t = 0.26$ s. The apparent (macroscopic) static friction coefficient is slightly above $F_s/F_N = 0.5$, which is considerably below the local $\mu_s = 0.9$ imposed at the interface. This is the effect of strongly non-uniform interface tractions present in the side-driven set-up. The macroscopic force ratio is, if dynamic effects are neglected, the ratio of the interface tractions integrated over the entire interface. The local friction law, however, imposes a maximum to the local ratio of interface tractions. Thus, the apparent static friction coefficient is always smaller than the local static friction coefficient, if the interface tractions are non-uniform.

The force drops appearing before macroscopic sliding are the result of local slip events that

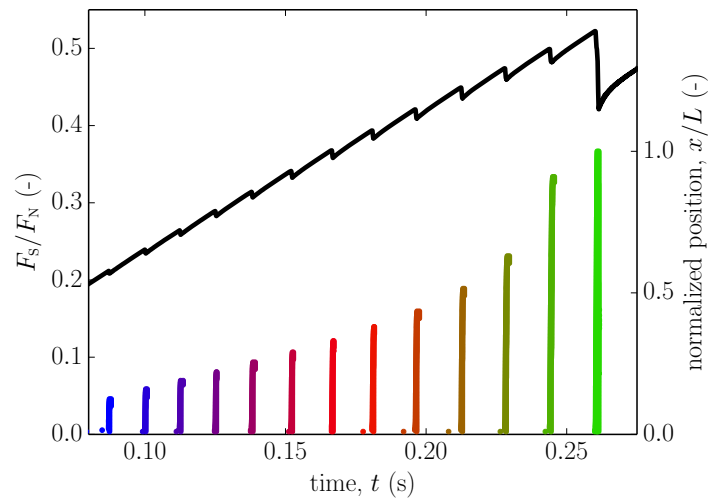


Figure 6.4: Numerical results for precursor propagation. The black line shows the macroscopic shear to normal force ratio over time. Small force drops appear before global sliding occurs at approximately $t = 0.26$ s. Colored areas indicate slip regions with respect to time, where the position is normalized by the interface length. The timing of slip precursors coincide with the macroscopic force drops.

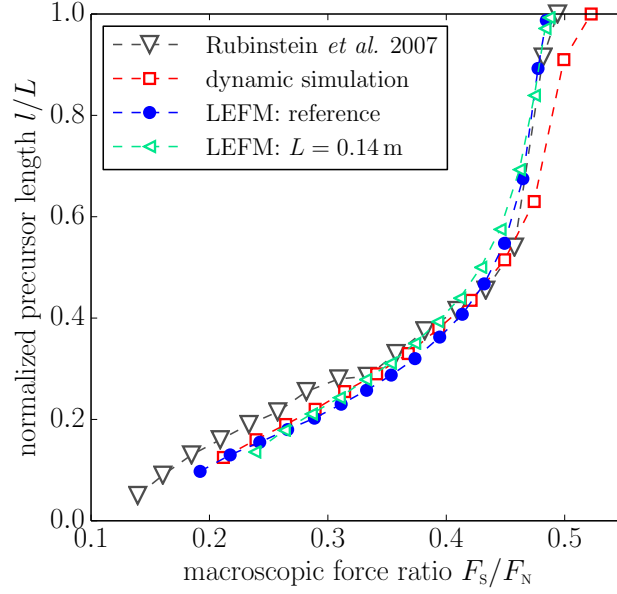


Figure 6.5: Evolution of normalized precursor length with increasing macroscopic force ratio F_s/F_N . Comparison of LEFM theory with experimental data from (Rubinstein et al., 2007), and dynamic finite-element simulations from (Radiguet et al., 2014).

propagate over parts of the interface. Such precursors, as shown as colored areas in Figure 6.4, initiate at the trailing edge $x/L = 0$ and stop before reaching the leading edge at $x/L = 1$. The interval between these slip events is approximately constant because the initiation of the dynamic rupture is governed by a slowly expanding quasi-static slip zone at the trailing edge that needs to reach a critical length. Because after each slip event the stress state of the interface close to the trailing edge is nearly the same and the loading rate is constant, this nucleation procedure repeats itself in an almost identical way and results in a constant stick period.

As observed in the experiments of Rubinstein et al. (2007), each precursor propagates further than the previous one. The precursor length increment is almost constant until a slip event reaches approximately the center point of the interface, from which on only one to two precursors occur before global sliding. The resulting precursor load-length relation, as introduced in Section 6.1, is shown in Figure 6.5 (red squares). It is in good quantitative agreement with experimental data from Rubinstein et al. (2007) and presents the same linear relation until $l/L \approx 0.5$ as well as a fast transition to global sliding.

6.3.2 Comparison of LEFM Model with Experimental Data

In Figure 6.5, we compare the prediction of the LEFM model (blue dots) with experimental data of Rubinstein et al. (2007) (gray triangles). The LEFM prediction is in good quantitative

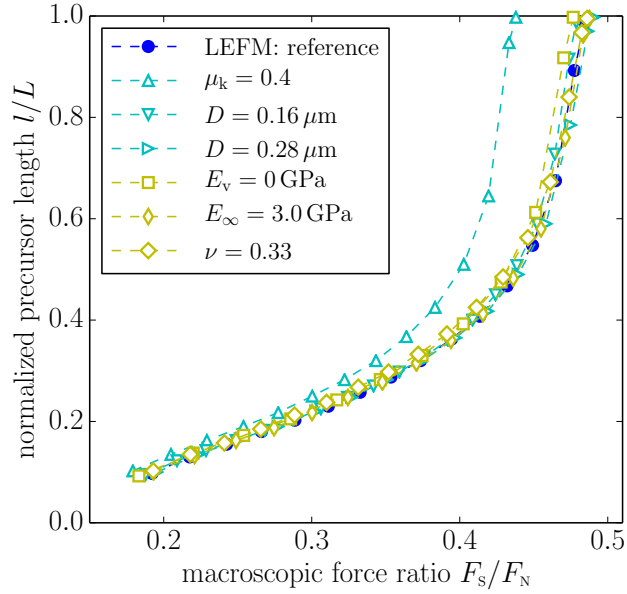


Figure 6.6: Analysis of the influence of different interface and material parameters on the precursors load-length prediction of the LEFM model. Parameters that are changed with respect to the reference case are given in the legend. The variation of the equivalent slip distance D for $\mu_k = 0.45$ corresponds to the uncertainty range of the frictional fracture energy deduced from experiments (Svetlizky and Fineberg, 2014).

agreement with experimental data and retrieves well the non-linearity of the length vs. load curve. It is also in good quantitative agreement with the results from the dynamic finite-element simulation as presented in Section 6.3.1. Further, we also confirm the observation of (Trømborg et al., 2011) that the slider geometry does not influence the normalized precursor length behavior by changing the slider length to $L = 0.14$ m (see cyan triangles in Figure 6.5).

We present in Figure 6.6 the influence of various material and interface properties with variations of the order of their uncertainties. The value of μ_k is estimated by the macroscopic force ratio F_s/F_N measured directly after a slip event, which is often $\mu_k \approx 0.4 - 0.45$ (Rubinstein et al., 2007). Introducing an equivalent slip distance $D = (\mu_s - \mu_k) d_c/2$ enables us to write Equation (6.7) as $K_{IIc}(x) = \sqrt{E_0 D \sigma(x)}$. According to the experiment-based estimation of the frictional fracture energy of PMMA interfaces reported by Svetlizky and Fineberg (2014), the uncertainty of the equivalent slip distance can be determined to be within the range of $D = 0.22 \pm 0.06 \mu\text{m}$ for $\mu_k = 0.45$.

With the exception of μ_k , the variations of all material and interface parameters within their uncertainties have negligible effects on the $l/L - F_s/F_N$ relation (Figure 6.6). Even neglecting entirely the viscoelasticity of the bulk material ($E_v = 0$ GPa) does not affect the precursor behavior. This weak influence originates from the square root contribution of E_0 and D to K_{IIc} . Only a change of μ_k within its uncertainty range results in an important shift of the $l/L - F_s/F_N$

curve due to its additional contribution to K_{II} , see Equation (6.5) and Equation (6.6).

6.3.3 Test of Model Assumptions

We have shown that the LEFM model is able to produce an accurate prediction of the precursor load-length curve, and reproduce the transition from the initial linear length increase to faster increase at a finite value of load. In the following, we aim at giving a more fundamental understanding of the origin of the load-length curve, by identifying several sources of the non-linearity in this scaling. This is done by removing different components from the LEFM model.

We present in Figure 6.7 a simplification of the theoretical model (denoted model A), which is based on the same LEFM approach, but where any change of the interface tractions due to slip is neglected ($\Delta\tau_i = 0 \quad \forall i$). Under these conditions, the discrete nature of precursors is lost. The length associated to a given macroscopic force ratio is independent of the slip history of the interface, and corresponds to the length that the first precursor would reach if it initiated at that specific loading. The loss in discreteness results in a more (but still not) linear $l/L - F_s/F_N$ relation. In this simplified model, for a given F_s , the stress drop close to the trailing edge is larger than in the reference case, resulting in a higher value of K_{II} and in longer precursors. But for $l/L > 0.7$, this effect is compensated in the full theory by the stress redistribution close to the arrest position of the previous precursor.

As noted before, the shear tractions at the interface result not only from the macroscopic shear load but also, due to frustrated Poisson's expansion, from the normal load. The influence of the latter is analyzed in model B. The shear contribution of the macroscopic normal load is removed by setting artificially $\tau_N(x) = 0 \quad \forall x$. All remaining interface tractions are kept the same as for the reference case. The resulting propagation distances reported with respect to the macroscopic force ratio are shown in Figure 6.7. For any given shear force F_s , the precursor length is longer for the simplified model B than for the reference model. For $l/L < 0.5$, this is the logic consequence of neglecting $\tau_N(x)$ which acts against the driving traction $\tau_s(x)$. Beyond the central point of the interface, the precursor lengths increase faster but still less than in the reference system, where $\tau_N(x)$ contributes to the propagation of precursors. From a global perspective, the precursor load-length curve is still non-linear (but less than the reference model). This indicates that the interfacial shear traction resulting from frustrated Poisson's expansion is one but not the only source of non-linearity in the system.

We also present the results of the simplified model AB, which is the combination of model A and B, where stress drops due to interface ruptures as well as shear traction caused by frustrated Poisson's expansion are neglected. As for model A, the discrete nature of precursors is lost in model AB. The precursor load-length relation, which is shown in Figure 6.7, is almost perfectly linear indicating that most sources of non-linearity (at least for the studied system and parameter range) are eliminated from this simplified model. The non-linear form of the stress intensity factor, which is still part of model AB, does not seem to affect the precursor

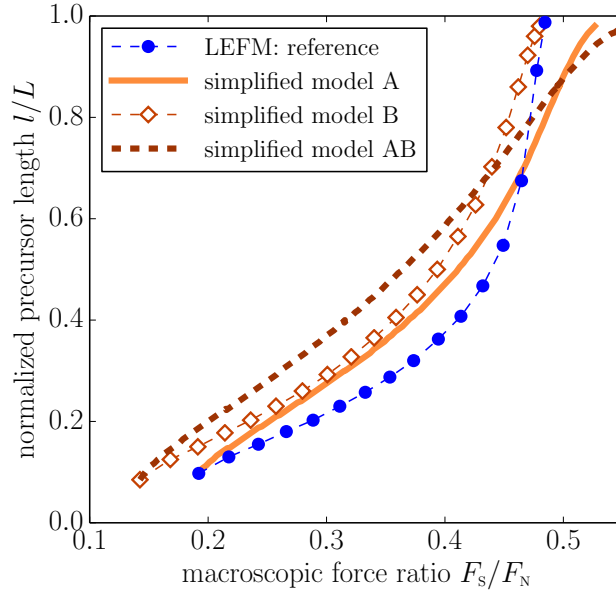


Figure 6.7: Precursor load-length relation for various simplified LEFM models with comparison to full LEFM theory. Model A: traction changes due to interface ruptures are neglected ($\Delta\tau_i(x) = 0$). Model B: Interface shear tractions due to frustrated Poisson's expansion are neglected ($\tau_N(x) = 0$). Model AB: combination of model A and B ($\Delta\tau_i(x) = 0$ and $\tau_N(x) = 0$).

propagation distance much within the length of the interface.

6.3.4 LEFM Prediction for Symmetric Set-up

Up to this point, we have compared our model to existing experimental data, analyzed the influence of different material and interface parameters, and have studied the non-linearity of the precursor load-length relation. Now, we can use our LEFM model to predict the response of a different system for which no experimental data has been published yet.

The set-up studied so far consists of a thin slider on a thicker base, which presents characteristics of a bi-material interface due to differences in the effective stiffness. This bi-material property influences the rupture propagation (Weertman, 1980). It is potentially interesting to remove this effect from experimental observations of frictional precursors by using a set-up with a single-material interface. We thus consider a symmetric system, where the base has the same geometry as the slider (in all three directions) and provide first insights to the propagation of precursors along a single-material interface. In this system, the non-zero τ_N due to frustrated Poisson's expansion [see Figure 6.1(b)] is naturally eliminated. Also all other interface traction components are different in a symmetric set-up and are computed with additional static finite-element simulations. An example of an effective normalized contact pressure of the symmetric set-up is shown in Figure 6.8(a) (solid pink line) and compared

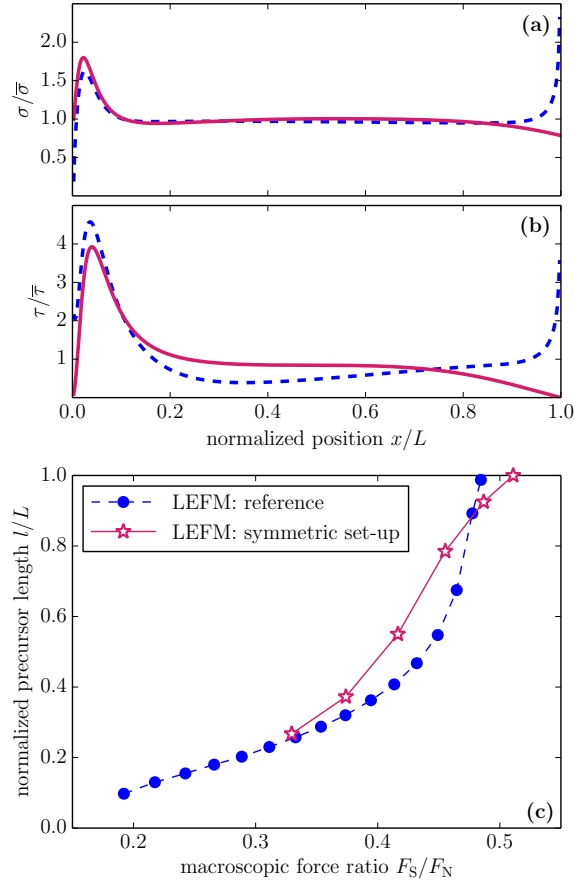


Figure 6.8: Comparison with a symmetric set-up, where the base has the same geometry as the slider. (a) Normalized contact pressure and (b) normalized shear traction of an unruptured interface for the reference set-up (blue dashed line), as also shown in Figure 6.1(d), and for a symmetric set-up (pink solid line) for $F_N = 5F_S$. (c) Normalized precursor length l/L reported with respect to the macroscopic force ratio F_S/F_N for the reference set-up (blue dots), as also shown in Figure 6.5, and for the symmetric set-up (pink stars).

with the normalized contact pressure of the reference set-up (dashed blue line), which was already reported in Figure 6.1(d). As expected, the main difference is the absence of the edge singularity in the symmetric set-up at $x/L > 0.9$, which will only have a small influence on the precursor mechanics. In Figure 6.8(b), the normalized shear traction at the interface of the symmetric set-up (solid pink line) and the reference set-up (dashed blue line) are compared. The symmetric set-up is generally a system of lower stiffness, which leads to a peak at approximately $x/L = 0.05$ which is smaller than in the reference set-up but a stress level that is considerably higher up to $x/L = 0.7$.

The precursor load-length prediction of our LEFM model for the symmetric set-up is shown in Figure 6.8(c) (pink stars) and compared with the prediction for the reference system (blue

dots), which was already shown in Figure 6.5. In the symmetric set-up, the first precursor appears at higher macroscopic force ratio, which is the result of the lower stress peak in $\tau_r(x)$ [see Figure 6.8(b)]. The length of the first precursor is about the same than the precursor propagating at the same F_s/F_N in the reference system. However, the precursor lengths increase faster in the symmetric system and the load-length relation presents an inflection point between the third and fourth precursors. Moreover, there are considerably less precursors in the prediction for the symmetric set-up (precursor length increments are larger), which indicates that it is harder to experimentally observe precursors in such a system.

6.4 Conclusion

We showed that a theoretical model based on linear elastic fracture mechanics predicts quantitatively well the precursor behavior observed in laboratory experiments (Rubinstein et al., 2007). Using this model, we revealed that the kinetic friction coefficient is key to an accurate prediction of the precursor length as it directly affects the stress intensity factor through the stress drop along the interface crack. Moreover, we showed that the variation of material parameters (within their uncertainty range) does not affect the observed precursor load-length relation. By simplifying this model in various ways, we analyzed different aspects that influence the non-linearity of the precursor growth and demonstrated that the shear tractions due to frustrated Poisson's expansion and the discrete nature of precursors are the main sources of the observed non-linearity. The redistribution of the shear tractions along the interface caused by each precursor is essential to the load-length relation. With the results of this theoretical description of slip precursors, we provide evidence for considering frictional slip and precursors as a fracture phenomenon.

7 Heterogeneous Interface

Interfaces at which slip fronts propagate are naturally heterogeneous at various length scales. The influence of such heterogeneities on the propagation of slip and the interface mechanics has long remained obscure due to various difficulties in experimental and numerical observations. It is, however, of great importance to many fields including engineering and earthquake science. In this chapter, we present results from three-dimensional simulations showing the propagation of a slip front at a striped heterogeneous interface. By comparing the slip front propagation at interfaces that differ solely by the length scale of the heterogeneous pattern, we illustrate that two different propagation regimes exist. These numerical results as well as theoretical considerations suggest that the origin of these two distinct propagation mechanisms lies in the interaction between the length scales of the slip front and the heterogeneous configuration. The implications for manufactured interfaces with desired high frictional strength is important because frictional energy dissipation during the onset of sliding is considerably increased at the transition from one to the other propagation regime for interfaces of equal average fracture toughness.

A scientific article containing the work presented in this chapter is currently in preparation for submission.

7.1 Slip Front Propagation through Interface Heterogeneities

The propagation of slip fronts at frictional interfaces as well as classic shear cracks at weak interfaces have, in the past, mainly been studied in two-dimensional systems. Neglecting the third dimension enabled the use of plane-strain or plane-stress approximations and reduced the interface to a one-dimensional line. This simplified the theoretical description of interface ruptures and decreased significantly computational cost of numerical simulations. Nevertheless, the propagation of ruptures along two-dimensional interfaces presents interesting additional aspects. The effect of non-homogeneous interfaces, for instance, is of great importance for earthquake sciences (because faults are not homogeneous) and engineering (where the use of “designed” materials such as composites is increasingly common). Most ruptures propagate along interfaces that present different types of heterogeneities at various scales. Examples are non-uniform loading, such as areas of higher or lower prestress, and heterogeneous interface properties, such as zones of stronger/weaker strength or rate-strengthening/weakening friction. Either of these types of heterogeneities affect the propagation of any rupture, but become particularly interesting for fronts of at least two dimensions because areas that are less easily broken can simply be circumvented (or partially circumvented and broken with delay).

The experimental observation of slip events at frictional interfaces is challenging and only few results of two-dimensional fronts have been reported so far. Brörmann et al. (2013) and Romero et al. (2014) showed on interfaces with discrete contacts (pillars and spherical caps, respectively) that the transition from sticking to sliding is characterized by slip fronts propagating along the interface, similar to the observations of Rubinstein et al. (2004) but at a two-dimensional interface. Latour et al. (2013) studied experimentally the effect of interface barriers on frictional slip. They showed, using different configurations of barriers, that heterogeneities can cause rupture arrest/delay as well as increase/decrease of the rupture speed. However, no systematic prediction can be provided because the behavior of a sequence of ruptures is complex and memory effects potentially cause inter-dependence of subsequent ruptures.

More experimental observations showing the effects of heterogeneities have been reported for Mode I (decohesion) ruptures. Natural heterogeneities of the interface (Måløy et al., 2006) and the bulk material (Ponson, 2009) were observed to affect the propagation speed. Måløy et al. (2006) analyzed local velocity fluctuations of an interface crack along a heterogeneous weak plane and showed that local velocities larger than the average front speed present a power law distribution. Ponson (2009) observed that the speed of a crack in a heterogeneous sandstone is related to the driving force in two distinct regimes. Theoretical studies of planar (tensile) cracks in heterogeneous media suggested that elastic wave propagation are a key component to explain the observed roughness of the fracture (Ramanathan et al., 1997; Ramanathan and Fisher, 1997, 1998; Bouchaud et al., 2002). Other experiments applied artificial heterogeneities in order to study their influence on the rupture fronts. Mower and Argon (1995) performed crack-trapping experiments showing a locally bowed configuration of

7.1. Slip Front Propagation through Interface Heterogeneities

a quasi-static crack between two obstacles with higher interface strength. Dalmas et al. (2009) and Chopin et al. (2011) described the shape of quasi-static and dynamic decohesion fronts, respectively, observed at interfaces with strips of different fracture energy. Xia et al. (2012) showed in thin-film experiments that the macroscopic peel force depends on the shape of the interface heterogeneities. Experiments with the same cumulative area of stronger interface results in different peel forces only due to modified heterogeneity configurations.

In addition to experimental observations, some numerical studies of the propagation of frictional shear ruptures at weak interfaces have been conducted in the past. This includes one-dimensional as well as two-dimensional interfaces with heterogeneities due to changed pre-stresses or modified frictional properties of the interface. The number of simulations with two-dimensional interfaces is limited because a set-up with a rupture far from the edges (to avoid the influence of wave reflection), with a small process zone compared to the rupture length, and with a sufficient fine discretization is computationally challenging. Early work by Day (1982b) showed that the rupture speed presents large changes during the propagation along an interface with zones of higher and lower pre-stresses. Fukuyama and Olsen (2002) and Dunham et al. (2003) demonstrated with numerical simulations of two-dimensional interfaces that a circular heterogeneity of higher pre-stress or higher fracture energy can provoke a transition from sub-Rayleigh to (temporary) super-shear propagation. Three-dimensional simulations provided also the opportunity to study differences in the near-source ground motion of earthquakes when an interface rupture propagates through an area of higher strength or higher pre-stress (Page et al., 2005). Other simulations were used to study earthquake mechanisms at faults with velocity-weakening patches surrounded by velocity-strengthening areas (Rice, 1993; Ben-Zion and Rice, 1997; Madariaga and Olsen, 2000; Kaneko et al., 2008; Ariyoshi et al., 2009; Kaneko and Ampuero, 2011; Ariyoshi et al., 2012). In these set-ups, the velocity-strengthening zone allows for a slowly increasing load and energy accumulation in the system, which eventually leads to dynamic ruptures (earthquakes) propagating mostly within the velocity-weakening zones. The dynamic propagation of ruptures at two-dimensional interfaces was also numerically modeled with heterogeneous initial stresses mimicking a realistic state of a fault (Andrews, 2005; Brietzke et al., 2009).

Even though the effect of heterogeneities on the propagation of slip fronts is different at one-dimensional interfaces, such simulations are still important tools to help understanding the underlying mechanisms. Das and Aki (1977) showed that ruptures at one-dimensional interfaces can propagate through areas of higher strength with and without breaking the heterogeneity. In a different set-up with a weak zone and a strengthening zone, Voisin et al. (2002) studied the arrest of frictional slip at the border of the areas of different properties and showed the presence of a self-healing slip pulse that penetrates the strong area. A detailed study of the transition from sub-Rayleigh to inter-sonic propagation by Liu and Lapusta (2008) demonstrated that a favorable heterogeneity leads to a secondary crack which transitions to inter-sonic speeds with an abrupt jump from the Rayleigh wave speed to an inter-sonic speed (without formation of a daughter crack).

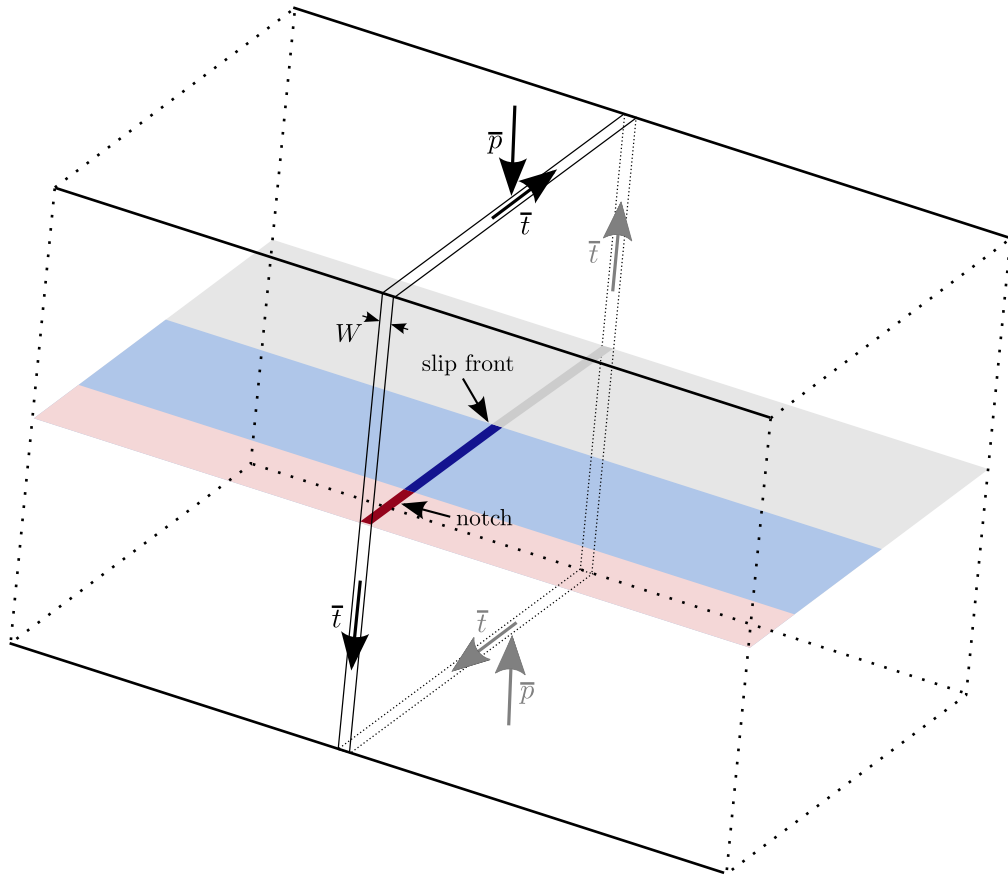


Figure 7.1: Three-dimensional set-up for simulations with heterogeneous interfaces. Two solids each of length L and height H are in contact and loaded by normal pressure \bar{p} and shear traction $\bar{\tau}$. Periodic boundary conditions in z -direction ensure an infinite width (with replication width W). A slip front is nucleated by a notch (red area) introduced at $t = 0$ and propagates in x -direction. The slipping and sticking areas of the interface are shown in blue and gray, respectively.

In this chapter, we present a study of the propagation of a rupture at a two-dimensional frictional interface and challenge the computational limitations of full three-dimensional (mesh-converged) finite-element simulations. With the goal of limiting the number of parameters to as few as possible, we consider a semi-infinite interface at which a (straight) slip front enters an area with strips of different fracture energies. The friction properties of the strips are chosen such that the propagation speed of ruptures along corresponding homogeneous interfaces result in sub-Rayleigh and inter-sonic speeds for the stronger and the weaker interfaces, respectively. Combining these properties in a strip configuration, however, leads to different types of rupture propagation depending on the width of the strips.

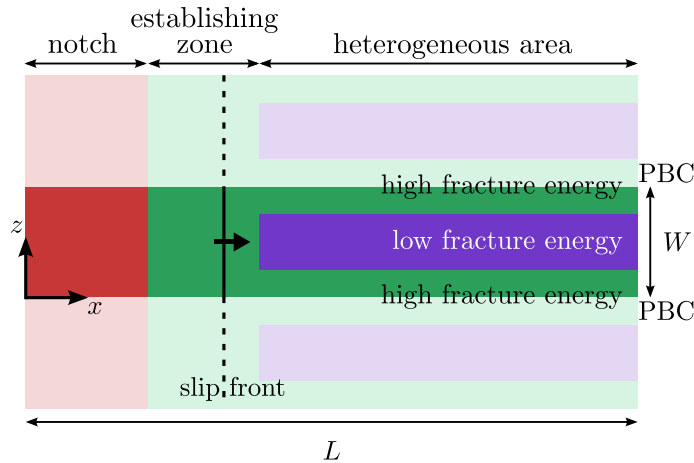


Figure 7.2: Configuration of heterogeneous interface (not to scale) of length L in x -direction and infinite width in z -direction. Periodic Boundary Conditions (PBC) are used to model the infinite width. Duplicates of the simulated interface are shown in lighter colors in order to provide an overall view. This figure corresponds to a view of the interface shown in Figure 7.1 from a negative y position in positive direction. The interface is separated into three areas: notch, establishing zone, and heterogeneous area. In the notch, the fracture energy is set to be zero, which causes the nucleation of the slip front. In the establishing zone, before reaching the heterogeneous area, the rupture accelerates and approaches a steady state with a straight front. In the heterogeneous part, the interface consists of strips of high and low fracture energy. The strips have wavelength W corresponding to the width simulated between the periodic boundary conditions.

7.2 Simulation Set-up

The propagation of a slip front at a two-dimensional heterogeneous frictional interface is studied in a simple set-up as shown in Figure 7.1. The two solids in contact are each of length $L = 200$ mm and height $H = 100$ mm, and are chosen to be infinite in the z -direction (perpendicular to the direction of propagation) in order to avoid edge effects. At a homogeneous interface, this set-up results in a straight slip front. Infinity in z -direction is modeled by periodic boundary conditions. The rather large geometry of the solids ensures that reflected waves cannot affect the propagation of the front along large parts of the interface. Perturbations due to reflected waves cannot be avoided close to the end of the interface because the waves ahead of the rupture are always reflected by the leading edge.

The system is loaded statically by a normal load $\bar{p} = 5$ MPa applied in the y -direction, and an in-plane shear load $\bar{t} = 2$ MPa applied on all boundaries in the $x - y$ plane. This load configuration results in uniform contact pressure and friction tractions at the interface and separates the effect of varying interface tractions from the effects of the heterogeneity. The influence of non-uniform stress states is studied in Chapter 5.

The material and interface properties do not represent a particular material but are, nev-

ertheless, realistic values. Emphasis is given to the necessity of enabling mesh-converged simulations of an interface rupture with a process zone of small size compared to the rupture length. If not indicated differently, the material and interface parameters are as follows. The bulk material is linear elastic with Young's modulus $E = 2.6 \text{ GPa}$, Poisson's ratio $\nu = 0.37$, and density $\rho = 1130 \text{ kg/m}^3$. The resulting wave speeds are $c_d = 2017 \text{ m/s}$, $c_s = 916 \text{ m/s}$, and $c_R = 859 \text{ m/s}$. Friction at the interface is governed by a linear slip-weakening law as described in Section 3.2.3. Two different sets of parameters are applied to create a heterogeneous pattern of the interface. Areas of higher fracture energy have a static friction coefficient $\mu_s = 0.9$, a kinetic friction coefficient $\mu_k = 0.2$ and a characteristic weakening length $d_c = 18 \mu\text{m}$, which results in a fracture energy of $\Gamma_c = (\mu_s - \mu_k)\bar{p}d_c/2 = 31.5 \text{ J/m}^2$ for the applied normal load \bar{p} . Other areas have a low fracture energy of $\Gamma_c = 10 \text{ J/m}^2$, which results from $\mu_s = 0.6$, $\mu_k = 0.2$, and $d_c = 10 \mu\text{m}$. Note that both sets of parameters have the same kinetic friction coefficient, which results in a uniform stress state behind the slip front. The weaker interface, however, has a lower static friction coefficient and a smaller characteristic weakening length.

The dynamic simulations of the slip fronts presented here are based on the finite-element method. Detailed information about this numerical method is provided in Section 3.4. An explicit Newmark β -method is used for time integration. Interface reactions including contact pressure and friction tractions are applied through a traction-at-split-node technique (see Section 3.5 for more details). A regular mesh with hexahedral elements is used to discretize the solids in contact. Other numerical methods, such as the spectral boundary integral method, could potentially be better suited for the simulation of this particular set-up with a flat interface between two homogeneous linear elastic solids under uniform load and with heterogeneities limited to the interface. However, this chapter is a first step on a path to modeling complex systems with non-linear heterogeneous bulk materials as well as a study of the effect of heterogeneous interfaces on the propagation of slip fronts.

The configuration of the heterogeneous interface is shown in Figure 7.2. The slip front is nucleated by introducing at $t = 0$ a notch (shown in red) which acts as a seed crack and in which the fracture energy is equal to zero by setting $\mu_s = \mu_k = 0.2$. The rupture starts at the tip of the notch and propagates in positive x -direction. The slip front is originally straight because of the infinite width of the interface. During propagation through the establishing zone (shown in green), in which the interface is homogeneous, the rupture accelerates and constitutes an interface crack with corresponding near-tip strain fields. At the end of the establishing zone, the slip front enters the heterogeneous area in which the interface is organized in strips of alternating frictional properties. Half of the strips present the same properties than the establishing zone with a high fracture energy (shown also in green). The second half of the strips is characterized by a lower fracture energy (shown in violet). The weaker and stronger strips are always of equal width in the simulations presented in this chapter. Hence, the width of the simulated interface changes if the strips wavelength is modified.

7.3 Homogeneous Reference Cases

Before studying the effect of the heterogeneous interface on the propagation of a slip front, we present reference cases with homogeneous interfaces of the same frictional properties as used in the heterogeneous set-up. The aim of these homogeneous reference cases is to provide a basic understanding of the slip front propagation caused by the different frictional properties in this particular system with the given bulk material.

The propagation of a slip front at a homogeneous interface with the frictional properties corresponding to the high fracture energy is shown in Figure 7.3. The configuration used

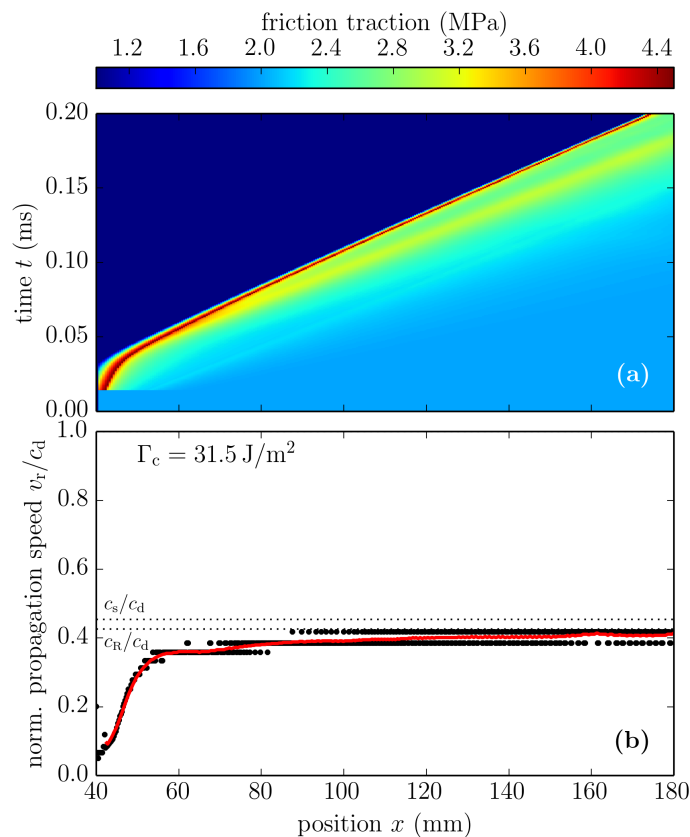


Figure 7.3: The propagation of a slip front at a homogeneous interface with fracture energy $\Gamma_c = 31.5 \text{ J/m}^2$. Data behind the seed crack $x < 40 \text{ mm}$ as well as close to the edge $x > 180 \text{ mm}$ is hidden in order to focus attention to a rupture that is not affected by wave reflections. **(a)** The friction traction at the interface is shown in color in a space-time map. The slip front starts at $x = 40 \text{ mm}$ and propagates in positive x -direction. The front is located in the red area, where the friction traction is maximal. The initiation phase of the rupture is invisible due to low data acquisition frequency during the beginning of the simulations ($t < 0.2 \text{ ms}$). **(b)** The rupture speed measured at each point of the space discretization (black points), which is also reported by an averaged value (red line), indicates that the slip front propagates at sub-Rayleigh speed. Values are normalized with respect to the dilatational wave speed c_d of the bulk material.

for this simulation corresponds to the interface shown in Figure 7.2 with a notch and a homogeneous interface everywhere else. The slip front nucleates at the tip of the notch and propagates in positive x -direction. It accelerates fast over the first 20 mm and, beyond this point, continues increasing slowly the rupture speed. Over the length of the interface, the rupture approaches the Rayleigh wave speed but stays sub-Rayleigh at all times. The process zone of the slip front, the yellow-red-yellow area in Figure 7.3(a), shrinks with increasing rupture speed as expected by linear elastic fracture mechanics theory (Rice, 1980; Freund, 1990).

In a second reference case, shown in Figure 7.4, a slip front is nucleated by the same notch and propagates first along a homogeneous interface of the same frictional properties as for the first reference case. During this phase, the observed behavior corresponds to the rupture propagation shown in Figure 7.3. However, after the same slip front as in the first reference case is established, the friction properties are modified and correspond to an interface of lower fracture energy. This set-up is similar to the configuration presented in Figure 7.2, except that in the so-called heterogeneous area, the interface is homogeneous and of low fracture energy over its entire width (only violet). The border between the establishing zone and the area of low fracture energy is at $x = 75$ mm and is marked by vertical lines in Figure 7.4. When the sub-Rayleigh slip front approaches the border, a secondary rupture nucleates in the area of lower fracture energy due to a shear stress peak that propagates ahead of the slip front. The secondary rupture, which merges shortly after with the main slip front, initiates directly at an inter-sonic speed just above the shear wave speed. The mechanism of a secondary crack at inter-sonic speed created within a favorable area was also observed by Liu and Lapusta (2008). From the border on, the slip front accelerates up to $0.83c_d$ at which speed it reaches a steady state. Similarly, in a set-up with homogeneous frictional properties of lower fracture energy over the entire length of the interface, the rupture accelerates directly to inter-sonic speed right after nucleation and reaches the same steady state. The peak value of the friction traction is smaller in the area of the weaker interface where $\Gamma_c = 10.0 \text{ J/m}^2$ (there is no red area in Figure 7.4(a) for $x > 75$ mm) because the static friction coefficient is smaller with $\mu_s = 0.6$ (compared to 0.9).

In summary, the reference cases showed that the proposed interface parameters result in the given system in two different propagation regimes. The set-up with the higher fracture energy at the interface can be characterized, following Andrews (1976b), by the seismic ratio $S = (\mu_s \bar{p} - \bar{t}) / (\bar{t} - \mu_k \bar{p}) = 2.5$, which causes a sub-Rayleigh propagation over the entire length of the system. The set-up with the lower fracture energy presents, however, a seismic ratio of $S = 1.0$, which results, for the applied nucleation procedure, directly in a rupture with inter-sonic speed. The effect on the propagation of a slip front by combining both friction properties in a single heterogeneous configuration is analyzed in the following section.

7.4. Heterogeneous Interface: Dynamic Simulation Results

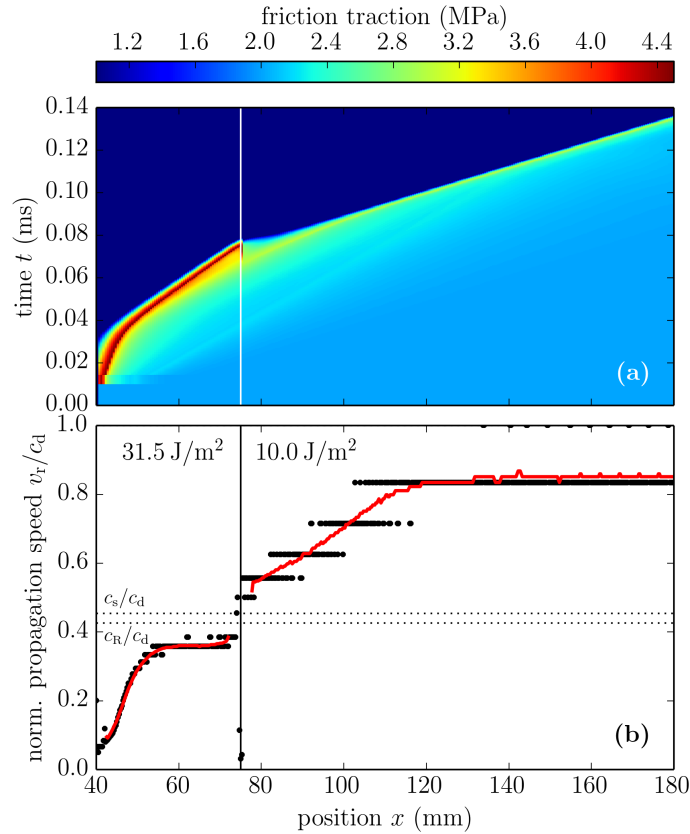


Figure 7.4: The propagation of a slip front at a homogeneous interface crossing the boundary from an area of high to low fracture energy, with $\Gamma_c = 31.5 \text{ J/m}^2$ and 10.0 J/m^2 , respectively. **(a)** The space-time map of the friction tractions presents a sudden change at the boundary from the high to low fracture energy area (indicated by a vertical white line). The maximal friction traction observed in the area of lower fracture energy is smaller than in the establishing zone because the static friction coefficient is smaller. **(b)** The rupture speed follows first the same trend as in Figure 7.3(b) until it reaches the area of lower fracture energy, in which it accelerates instantaneously to inter-sonic speed.

7.4 Heterogeneous Interface: Dynamic Simulation Results

7.4.1 Two Distinct Propagation Mechanisms

The propagation of slip fronts at heterogeneous interfaces present different behaviors depending on the wavelength of the strip configuration. Various simulations were conducted with wavelengths between $W = 4 \text{ mm}$ and $W = 8 \text{ mm}$ ($W = 4, 5, 6, 7, 8 \text{ mm}$). In all these simulations, two distinct propagation mechanisms are observed, which are described in this section. Snapshots of the expansion of the slip area are shown in Figure 7.5 for two representative interface ruptures, which are strip configurations with wavelength $W = 5 \text{ mm}$ and $W = 8 \text{ mm}$. The two distinct mechanisms are strictly separated by the wavelength of the strips. Slip fronts propagating at interfaces with $W \leq 6 \text{ mm}$ are equivalent to the slip front presented in the

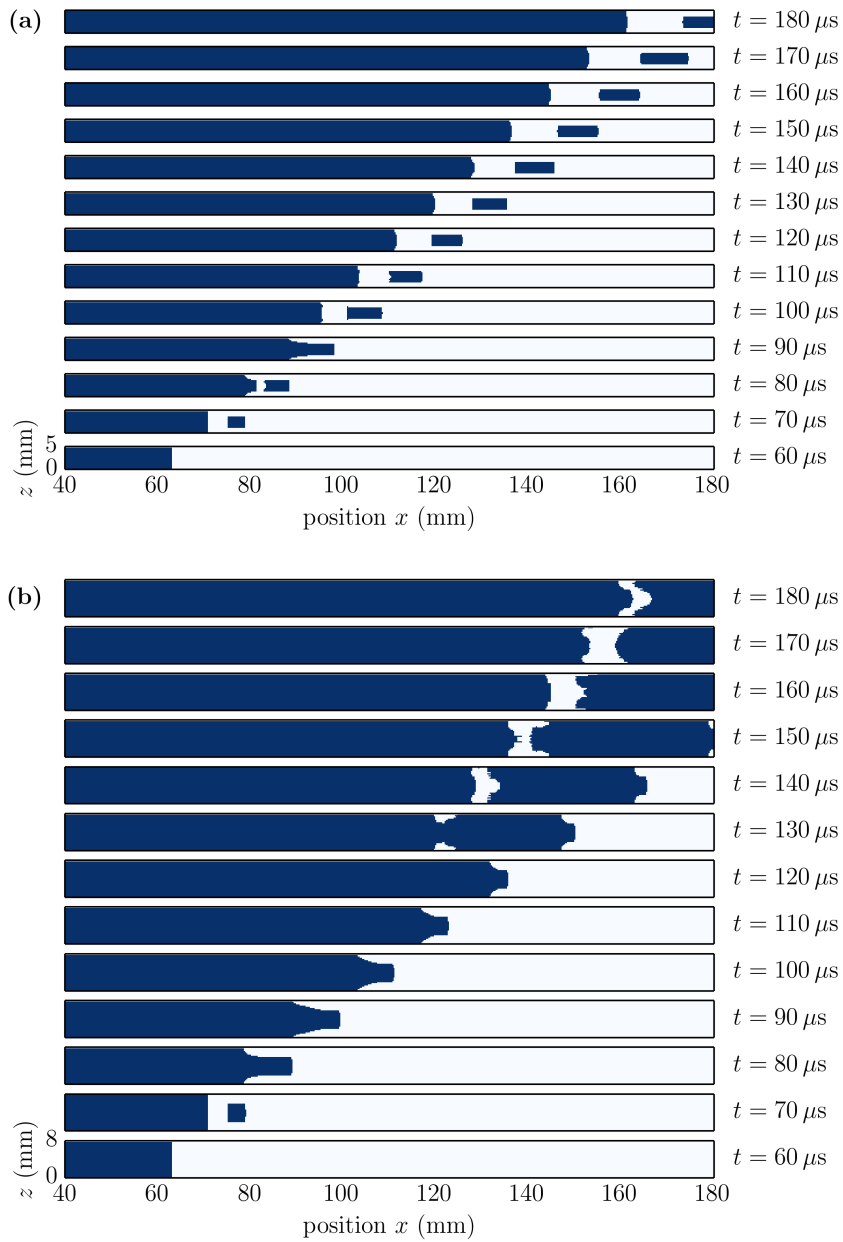


Figure 7.5: Interface snapshots of slip area (in blue) at heterogeneous interfaces. The heterogeneous area starts at $x = 75$ mm and consists of strips, as presented in Figure 7.2. The strip with lower fracture energy (violet strip in Figure 7.2) is located in the center of the shown interface. The same scale is applied to the x and z axes in order to preserve the correct aspect ratio of the interface. **(a)** The system with wavelength $W = 5$ mm result in a slip pulses in the weaker strips propagating ahead of the main front. **(b)** The configuration with wavelength $W = 8$ mm, however, presents a slip front propagating over the entire width. At approximately $t = 130 \mu s$, a “stick” front initiates at $x = 120$ mm and follows the slip front in positive x -direction.

7.4. Heterogeneous Interface: Dynamic Simulation Results

system with $W = 5$ mm, whereas ruptures at interfaces with $W \geq 7$ mm correspond to the behavior of the slip front in a set-up with $W = 8$ mm.

As shown by the snapshots in Figure 7.5, the front is flat and propagates at the same speed at both interfaces before it reaches the heterogeneous area (see at $t = 60 \mu\text{s}$). This is the result of the infinite width, modeled by periodic boundary conditions in z -direction, and the homogeneous establishing zone, as presented in Figure 7.2. As the slip front approaches the heterogeneous area starting at $x = 75$ mm ($t = 70 \mu\text{s}$), a secondary rupture initiates in both systems in the strips¹ of lower fracture energy, which corresponds to the behavior observed for the second reference case presented in Figure 7.4. While the front of the secondary rupture starts propagating instantaneously at inter-sonic speed, the main rupture continues advancing and eventually merges ($t \approx 80 - 90 \mu\text{s}$) with the trailing end of the secondary rupture forming one single slip event.

Up to this point in time, the slip fronts in the two interface configurations resemble each other. However, beyond this moment, the effect of the strip size becomes noticeable. In the system with thinner strips, the secondary rupture, which just became part of the main rupture, detaches again and distances itself slowly from the main slip front while propagating only in the strips of lower fracture energy. In the set-up with wider strips, the secondary rupture does not directly detach from the main rupture but pulls the front in the stronger strips in order to catch up with the front in the weaker strips. Nevertheless, at a later point in time, *i.e.*, $t = 130 \mu\text{s}$, a stick front initiates at $x \approx 120$ mm which creates again a main and secondary rupture. However, the secondary slip front propagates over the entire width of the interface and not only in the weaker strips as observed for the configuration with $W = 5$ mm. Another striking difference is that there is much more slip occurring in the front rupture of the wider system compared to the slip pulse of the thinner set-up.

The different behaviors of the slip fronts in these two heterogeneous configurations is also recognizable at the propagation speed shown in Figure 7.6. Differences in rupture speeds can also be observed in Figure 7.5 by looking at the position of the fronts at various moments. Beyond the starting point of the heterogeneous area, the main slip front in the system with $W = 5$ mm is first pulled by the secondary rupture and accelerates temporarily above the shear-wave speed. It decelerates, however, shortly after and continues propagation at sub-Rayleigh wave speeds (see dark green curve). The secondary rupture, which propagates only in the strips of lower fracture energy, initiates directly at inter-sonic speeds and propagates without ever entering steady state at various speeds around the Rayleigh- and shear-wave speeds (see dark purple curve). At approximately $x = 155$ mm, the slip pulse propagates over 10 mm continuously at the so-called forbidden speed, which is between the Rayleigh- and the shear-wave speed.

In the set-up with wider strips, the slip front propagates in the heterogeneous area over the

¹The plural form of strip is used because, even though only one weaker strip and two stronger half-strips are shown in the figures, there is an infinite number of strips due to the periodic boundary conditions.

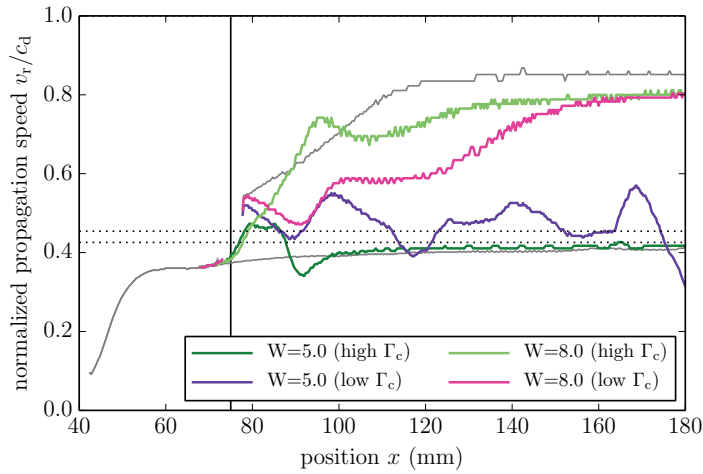


Figure 7.6: Propagation speed of slip fronts shown in Figure 7.5. The rupture speed is reported for the first slip front at the center line of each strip. The slip pulses in the weaker strips of the configuration with $W = 5$ mm, shown in dark purple, propagate with varying speed around the Rayleigh- and shear-wave speed. The main slip front in this system, shown in dark green, propagates at sub-Rayleigh speed with a short inter-sonic period at the beginning of the heterogeneous area. The slip front propagating at the interface with strip wavelength $W = 8$ mm is inter-sonic over the entire width. The rupture speed in the strips of higher and lower fracture energy is depicted by bright green and bright purple line, respectively. The thin gray lines show the rupture speed of the homogeneous reference cases presented in Figures 7.3 and 7.4. The vertical black line indicates the position at which the heterogeneous area starts.

entire length and width of the interface at inter-sonic speeds (see bright green and purple curves). Along $x = 85 - 155$ mm, the slip front propagates faster in the strips of higher fracture energy than in the weaker strips because the (originally) main front is catching up with the front that nucleated as secondary rupture ahead of it. However, beyond $x = 160$ mm, the front presents the same constant propagation speed over the entire interface width. The rear slip front initiating at $x = 120$ mm at $t = 130 \mu\text{s}$ due to the stick area appearing ahead of it, see Figure 7.5(b), propagates at high sub-Rayleigh speed (curve not shown in Figure 7.6).

It is interesting to note that these two distinct propagation mechanisms occur in systems with the same residual friction tractions and, more importantly, with the same average fracture energy. Macroscopically, these systems seem to be the same but result in different slip fronts.

7.4.2 Length Scale Interactions

The presence of two distinct mechanisms at interfaces with the same heterogeneous pattern and friction properties but with different strip wavelengths suggests that an interaction between two length scales is at play. This is particularly important during the transition from the homogeneous to the heterogeneous area of the interface. Zoomed snapshots on the relevant area during this transition, shown in Figure 7.7(a), illustrate that the size of the process zone,

7.4. Heterogeneous Interface: Dynamic Simulation Results

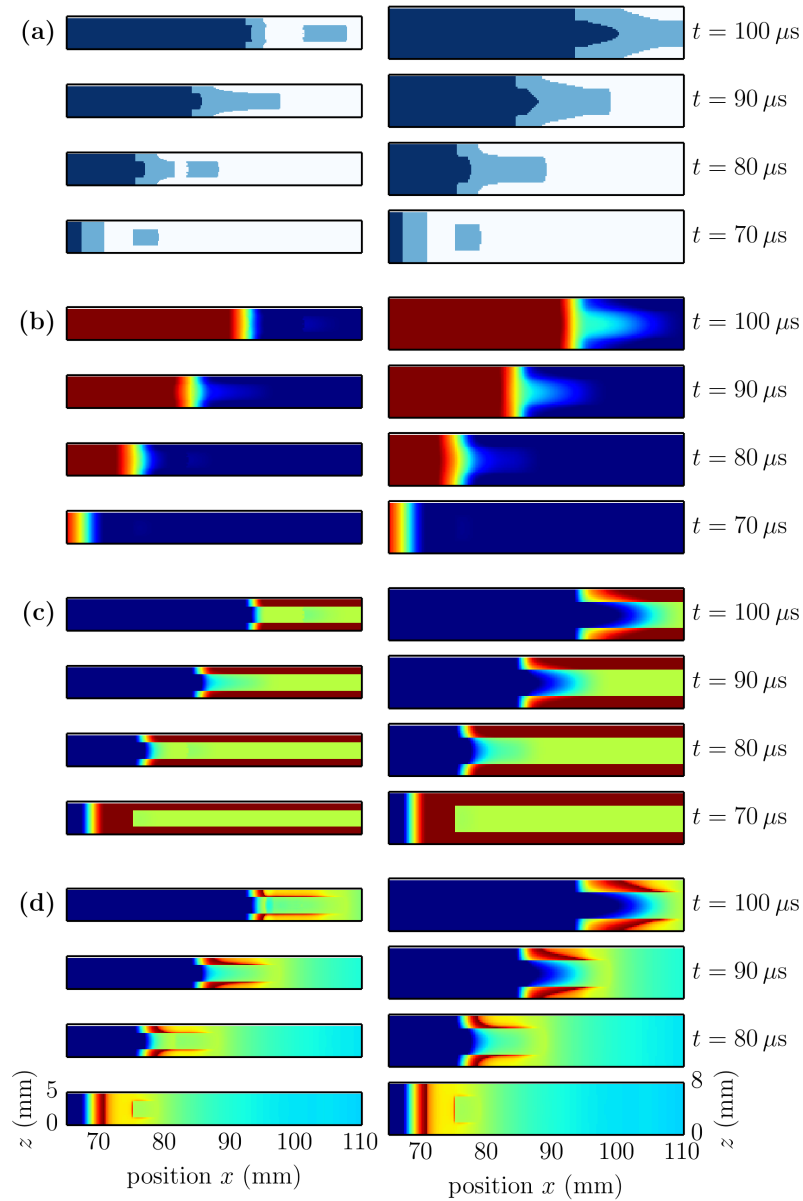


Figure 7.7: Interface snapshots for various fields shown for points in time when the slip front enters the heterogeneous area. The configuration with strip wavelength $W = 5$ mm and $W = 8$ mm, as presented in Figure 7.5, are illustrated in the left and right column, respectively. The same scale is applied to the x and z axes in order to preserve the correct aspect ratio of the interface. The snapshots show the **(a)** slip area in blue with the process zone in brighter color, **(b)** slip (distance) with scale: blue = 0 mm and red = 0.03 mm, **(c)** frictional strength with scale: blue = $\mu_k \cdot \bar{p}$ and red = $\mu_s \cdot \bar{p}$ (μ_s of high fracture energy), and **(d)** friction traction with the same scale as the frictional strength.

Chapter 7. Heterogeneous Interface

shown in brighter blue, is of the same order than the width of the strips. The interaction between the two length scales can be expressed as

$$\zeta = \frac{W}{w_{\text{pz}}}, \quad (7.1)$$

where w_{pz} is the characteristic size of the process zone in the weaker strips, and W is the wavelength of the strip configuration.

The determination of w_{pz} in the weaker strips during the transition of the slip front from the homogeneous to the heterogeneous area is challenging because the rupture is inter-sonic and transient. At inter-sonic steady state, the process zone length can be computed, following Broberg (1989), by

$$w_{\text{pz}} = \frac{\Gamma_c G}{\bar{p}^2 (\mu_s - \mu_k)^2} T(v_r, c_s, c_d), \quad (7.2)$$

where Γ_c is the fracture energy of the interface, μ_s and μ_k are the static and kinetic friction coefficients, \bar{p} is the normal pressure, G is the bulk's shear modulus, and T is a function depending on the propagation speed v_r and the dilatational c_d and shear c_s wave speeds.

Considering that the secondary slip front in the weaker strips presents in all configurations of different width the same speed during the transition, we can write

$$w_{\text{pz}} \sim \frac{\Gamma_c G}{\bar{p}^2 (\mu_s - \mu_k)^2}. \quad (7.3)$$

Substituting the fracture energy with $\Gamma_c = (\mu_s - \mu_k) \bar{p} d_c / 2$ and by defining the slope of the friction weakening process as $\phi = (\mu_s - \mu_k) \bar{p} / d_c$, Equation (7.3) is reduced to two basic parameters:

$$w_{\text{pz}} \sim \frac{G}{\phi}. \quad (7.4)$$

Reconsidering Equation (7.1), we can now write

$$\zeta \sim \frac{W\phi}{G} \equiv \zeta_a, \quad (7.5)$$

which provides a fundamental understanding, in first approximation, of the parameters affecting the preferred propagation mechanism. From the simulations presented in Section 7.4.1, we know that lower values of ζ lead to sub-Rayleigh ruptures with slip pulses propagating in the weaker strips ahead, whereas higher values of ζ result in an inter-sonic slip front propagating over the entire width of the interface.

Before considering the values of ζ_a of the various systems studied so far, let us first understand how the friction weakening rate, the shear modulus and the strip width influences the process

7.4. Heterogeneous Interface: Dynamic Simulation Results

of nucleating either of the two propagation mechanisms. When the slip front approaches the beginning of the heterogeneous area ($x = 75$ mm), a secondary rupture initiates ahead in the weaker strips (see snapshots at $t = 70$ μ s). Once the main front merged with the secondary rupture, the front continues propagation over the entire width of the interface (see snapshots at $t = 80 - 90$ μ s). The front is considerably ahead in the weaker strips than in the stronger ones due to the earlier initiation through the secondary rupture. During this period, there is a zone in which, at a given position x , the interface slips in the weaker strips but sticks in the stronger strips. As a consequence, the maximal slip occurs on the center line of the weaker strips. Its value depends on the shear modulus of the bulk material and the width of the weak strips. A higher shear modulus causes higher shear stresses in the xz -component between the border and the center line of the weaker strips, and results in less slip. A wider strip, however, presents for the same shear modulus more slip at the center because of the larger distance from the no-slip condition at the border. This can be observed by comparing slip in the systems with $W = 5$ mm and $W = 8$ mm at $t = 90$ μ s at the center line at $x \approx 90$ mm in Figure 7.7(b). Therefore, the maximal slip occurring at the center of weaker strips surrounded by sticking stronger strips behaves as

$$\max \delta \sim \frac{W}{G}. \quad (7.6)$$

The resulting frictional strength at the center of the weaker strips depends on the friction law as well as on the quantity of slip. In the case of a linear slip-weakening friction law, the strength decreases for increasing slip δ and weakening rate ϕ . Therefore, the minimal strength at the center of the weaker strips is given, if the adjoining stronger strips are sticking, by

$$\min \tau^s \sim \frac{1}{\phi \max \delta} \sim \frac{G}{W\phi}. \quad (7.7)$$

Note that these are not linear relations because slip and frictional strength are inter-dependent. On one hand, more slip at the center line of the weaker strips leads to lower strength, but on the other hand, lower strength resists less against the external load, which results in more slip.

Lower frictional strength and hence a lower friction traction at the interface has two consequences on the transition from the homogeneous to the heterogeneous area. First, a lower friction traction decelerates less the slip rate which increases the duration of slip and prevents the detachment of the slip pulse in the strip configuration. Second, a lower friction traction enables more slip over the same period which results in higher shear stresses in the bulk material. The later are responsible for pulling the slip front in the stronger strips into an inter-sonic propagation regime. The result of these pulling tractions is observable as red areas in Figure 7.7(d). All in all, lower frictional strength at the center of the weaker strips favors the propagation mechanism of an inter-sonic front over the entire interface width, whereas systems with a higher strength tend to cause a sub-Rayleigh rupture with a slip pulse propagating ahead in the weaker strips. This is consistent with Equation (7.5) as can be seen

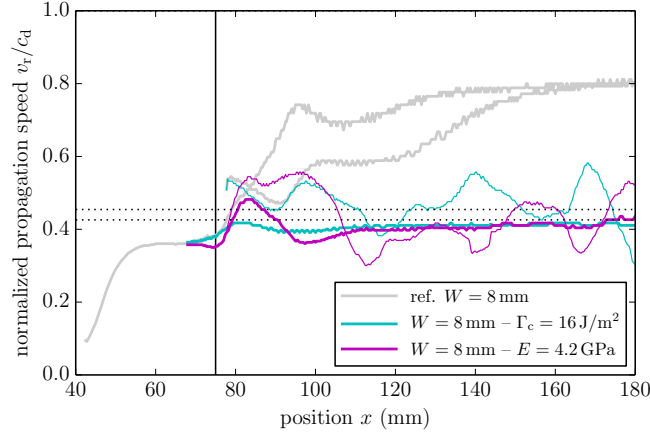


Figure 7.8: Propagation speed for slip fronts at different interfaces with heterogeneous strip configuration of wavelength $W = 8$ mm. The inter-sonic rupture shown in Figure 7.6 is reported in gray as reference. The propagation speed of two additional slip fronts is shown in color. The rupture illustrated by cyan curves has a modified friction weakening rate by setting $d_c = 16 \mu\text{m}$ (instead of $10 \mu\text{m}$), which leads to a fracture energy of $\Gamma_c = 16 \text{J/m}^2$. The magenta curves present the propagation of a rupture in a system of modified shear modulus by setting Young's modulus $E = 4.2 \text{GPa}$ (compared to 2.6GPa). Both slip fronts present at an interface of strip wavelength $W = 8$ mm the sub-Rayleigh propagation mechanism with a slip pulse ahead. The thicker lines represent the speed of the main front, whereas the thinner lines indicate the slip pulse speed.

by writing

$$\zeta \sim \frac{1}{\min \tau^s} \sim \frac{W\phi}{G}. \quad (7.8)$$

The value of ζ_a limiting the two distinct propagation behavior is deduced from the simulations presented in Section 7.4.1. The simulation with the largest strip wavelength leading to the sub-Rayleigh with slip pulse mechanism has $W = 6$ mm and $\zeta_a = 1.26$. The next larger wavelength simulated ($W = 7$ mm) presented the super-shear slip front and is characterized by $\zeta_a = 1.48$.

Up to this point, the two distinct propagation mechanisms have been shown to exist in systems which differ solely by modified wavelengths of the strip configuration. Equation (7.5), however, indicates that two additional parameters, the shear modulus of the bulk material and the friction weakening rate, affect the propagation mechanism occurring in a given system as well. Two additional simulations are performed in order to confirm the validity of Equation (7.5). The set-up with $W = 8$ mm and $\zeta_a = 1.68$ resulting in an inter-sonic slip front, as presented in Section 7.4.1, is used as reference. The shear modulus of the bulk and the friction weakening rate in the weaker strips are then independently modified such that $\zeta_a = 1.05$, which leads, as shown in Figure 7.8, to the propagation mechanism of a sub-Rayleigh rupture with a slip pulse.

The observation of a sub-Rayleigh rupture in a system with $W = 8$ mm but with $\zeta_a = 1.05$ confirms that the non-dimensional parameter provides an indication of the propagation mechanism occurring in a given set-up. It is also important to note that ζ_a is only an approximation to ζ because the T term is neglected in Equation (7.3). For instance, if the frictional properties are modified such that the propagation speed of the secondary rupture is changed considerably during the transition into the heterogeneous area, the estimation of the process zone size could be different and the value of ζ_a could indicate the wrong propagation mechanism. Nevertheless, ζ_a provides fundamental insights by indicating the material and interface properties that affect the type of propagation mechanism occurring.

The interaction between the length scale of the slip front and the interface heterogeneity, observed here in a strip configuration, is generally valid and is expected to appear also in different systems with heterogeneous areas of the order of the process zone size of the slip front. At interfaces organized with different shapes of heterogeneities, the value of ζ_a limiting different propagation behaviors is potentially different from values reported here for the strips configuration. Nevertheless, Equation (7.5) is applicable and provides information on what determines the mechanism of slip front propagation.

7.4.3 Energy Dissipation

The occurrence of one or another propagation mechanism in a given system influences the energy dissipation through frictional processes. At an interface governed by a slip-weakening friction law, the total dissipated energy can be considered as the sum of two distinct quantities. First, there is the so-called fracture energy which originates from the weakening process of friction. It is equivalent to the cohesive energy of a fracture mechanism and corresponds to the triangular area below the linear slip-weakening friction law for slip smaller than the characteristic length. If the kinetic friction is equal to zero ($\mu_k = 0$), the fracture energy is the only dissipated energy at the interface. Second, there is the friction energy which is caused solely by the kinetic friction force acting during slip.

The energy dissipation at the frictional interface for homogeneous reference set-ups and for the two representative heterogeneous systems is shown in Figure 7.9(a). Given that the interface is infinitely wide, all energies are reported per unit width. The homogeneous interface with the highest fracture energy ($\Gamma_c = 31.5\text{J/m}^2$) dissipates, compared to all the other systems, most energy during the propagation of the slip front. The difference to the homogeneous interface with lower fracture energy ($\Gamma_c = 10.0\text{J/m}^2$), however, is only indirectly caused by the fracture energy. Even though the difference of dissipated energy between the two homogeneous cases is 18.06J/m when the slip fronts reaches $x = 180$ mm, the difference in fracture energy accounts only for 2.26J/m . The remaining part is the direct result of different propagation speeds. The slip front propagating along the weaker interface is inter-sonic, which does not give the interface much times to slide and dissipate energy. The sub-Rayleigh rupture at the stronger interface, however, takes considerably more time to reach $x = 180$ mm, during

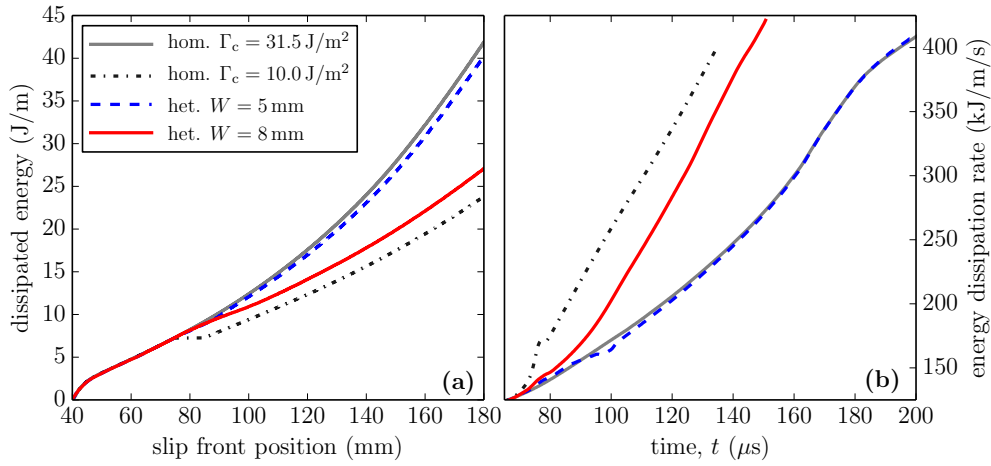


Figure 7.9: Energy dissipation of frictional slip fronts at homogeneous and heterogeneous interfaces. The dissipated energy includes the frictional energy due to the residual friction tractions as well as the fracture energy due to the weakening process of the frictional strength. **(a)** The dissipated energy per unit width is shown with respect to the position of the rupture tip for the two homogeneous reference cases and for the heterogeneous configurations of wavelength $W = 5 \text{ mm}$ and 8 mm . The rupture tip position is defined as the rearmost point of the first slip front propagating over the entire width. The reference cases enclose the energy dissipated by the heterogeneous interfaces. The set-up with $W = 8 \text{ mm}$ results in less energy dissipation than in the thinner configuration. **(b)** The temporal energy dissipation rate is reported for the same set-ups showing that the wider configuration dissipates faster energy than the thinner interface.

which the interface behind the front continues dissipating energy.

Considering the average fracture energy as well as the speed of slip front propagation, the heterogeneous configurations stand between the two homogeneous reference cases. As a natural consequence, the dissipated energy at the heterogeneous interfaces is bounded by the homogeneous references. However, the slip front propagating through the striped interface of smaller wavelength dissipates 48% more energy than the rupture in the system with wider strips despite having the same average fracture energy, $\Gamma_c = 20.75 \text{ J/m}^2$. The reason for this large difference is the same as for the comparison between the two homogeneous reference cases. The fracture energy accounts only for a small part of the total dissipated energy: 8–14% for the slip fronts presented in Figure 7.9(a). The main cause is the large difference in the propagation speed of the slip fronts. The set-up with $W = 5 \text{ mm}$ results in a sub-Rayleigh slip front and a hardly noticeable slip pulse ahead (propagating slightly faster and only in the weaker strips). The pulse causes only small slip and hence dissipates only little energy. The sub-Rayleigh rupture, however, is almost identical with the slip front of the stronger homogeneous reference case but with lower average fracture energy. Therefore, the total dissipated energy is slightly smaller. Similarly, the slip front at the heterogeneous interface with $W = 8 \text{ mm}$ resembles the rupture in the weaker homogeneous set-up. Both propagate at inter-sonic speed but the slip front at the heterogeneous interface is slower, which provides

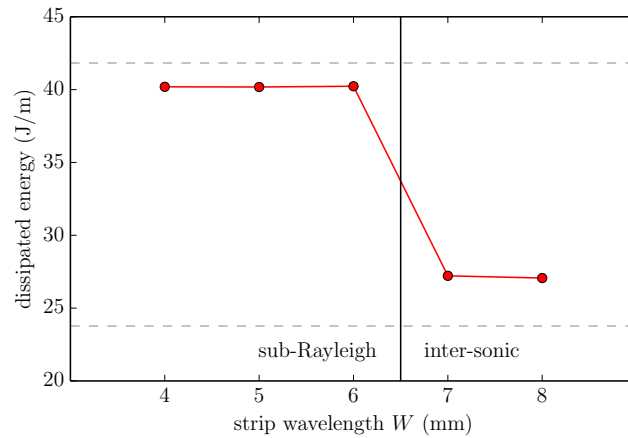


Figure 7.10: Frictional energy dissipation for slip fronts at heterogeneous interfaces as a function of the wavelength W of the strip configuration. The dissipated energy is reported per unit width at the point in time when the main slip front reaches $x = 180$ mm. The dashed gray lines illustrate the dissipated energy of the homogeneous reference cases. The vertical black line separates the wavelengths resulting in sub-Rayleigh or inter-sonic propagation. The dissipated energy is not affected by W except when the propagation mechanism changes.

the interface more time to dissipate energy.

The energy dissipation rate, shown in Figure 7.9(b), confirms these observations. The weakest (homogeneous) interface presents the highest rate because the slip area grows faster, which results in more dissipation in a shorter time. In the same way, the slip front propagating at (slightly) slower inter-sonic speed at the heterogeneous interface with wider strips presents a slower dissipation rate. It is, however, higher than the energy dissipation rate resulting from sub-Rayleigh ruptures.

It is also interesting to note that the dissipated energy does not present any dependence on the strips wavelength itself but only on whether it is above or below the critical wavelength limiting the sub-Rayleigh from the inter-sonic propagation mechanism. As shown in Figure 7.10, the energy dissipated before the slip front reaches $x = 180$ mm presents an important jump from $W = 6$ mm to $W = 7$ mm, but remains approximately constant below as well as above the critical wavelength. This suggests that if higher energy dissipation is sought by introducing interface heterogeneity, it is sufficient to design the heterogeneity pattern such that ζ_a is below the critical value to cause sub-Rayleigh slip fronts. Any heterogeneity configuration with smaller characteristic length W will not increase the frictional energy dissipation.

7.5 Conclusion

In this chapter, we presented finite-element simulations showing the propagation of slip fronts along flat two-dimensional heterogeneous interfaces between three-dimensional solids of the same linear elastic material. The set-up consisted of interfaces that are infinitely wide and

Chapter 7. Heterogeneous Interface

subjected to a static uniform shear and normal loading. Slip fronts were nucleated by inserting at one edge a notch of zero fracture energy acting as a seed crack. The slip front propagated first through a homogeneous part of the interface allowing the rupture to establish its process zone and to approach a state that evolves slowly (which resembles a steady state). Beyond this establishing zone, the interface is heterogeneous with areas of two different friction properties arranged in a strip configuration.

As reference cases, we first presented the propagation of slip fronts at homogeneous interfaces with the two friction properties of the heterogeneous set-up. These simulations showed that, over the length of the considered system, the stronger interface properties result in a sub-Rayleigh rupture, whereas the weaker interface gives rise to an inter-sonic slip front. The propagation behavior of an interface rupture becomes, however, more complex in a set-up with a striped heterogeneous area.

In systems with different wavelengths of the strip configuration, we showed that thinner strips result in the propagation of a sub-Rayleigh slip front preceded by a slip pulse in the strips of lower fracture energy. This slip pulse produces negligible quantities of slip and propagates in an “unstable” manner at speeds varying around the Rayleigh- and shear-wave speed including longer periods of propagation at a so-called forbidden speed. At interfaces with wider strips, the slip front transitions, after entering the heterogeneous area, to inter-sonic speeds over the entire width of the interface. At a later point in time, a zone of sticking occurs far behind the slip front and creates a front and rear rupture. The front rupture continues propagation at high inter-sonic speeds whereas the rear rupture propagates at a high sub-Rayleigh speed.

The occurrence of two distinct propagation mechanisms at the same interface with the only difference being the heterogeneous strip wavelength was shown to be caused by the interaction of two length scale: the process zone size of the slip front and the wavelength of the strip configuration. The ratio between these two lengths was proposed as a non-dimensional parameter capable of indicating the type of slip front propagation occurring in a given system.

The existence of two distinct propagation mechanisms was shown to have important implications on the energy dissipation through frictional processes at the interface. Even though the various configurations present the same average fracture energy, the dissipated energy increases substantially when the propagation mechanism switches from inter-sonic to sub-Rayleigh speeds due to an increased wavelength of the heterogeneous strip configuration. In the examples presented in this chapter, the energy dissipation was reported to increase by 48%. Similar observations are expected to occur also at other configurations of heterogeneous interfaces when the process zone size of the slip front and the heterogeneous length scale are of the same order.

8 Concluding Remarks

This thesis focused on the propagation of slip fronts at frictional interfaces. Using numerical as well as theoretical models, various aspects of frictional shear ruptures were analyzed in order to improve our understanding of the mechanics of slip front propagation. The main findings are summarized in this concluding chapter and an outlook for potential future work is provided.

It is interesting to note that structural mechanics has long been considered to be a classical engineering discipline, which resulted in scientific attention being mostly oriented to micro- and nano-scale physics. Friction is a typical example of this approach. A large amount of research efforts is focused on the small scale frictional properties of interfaces and many (recent) experiments consist of nano-scratching and friction force microscopy. One could therefore say that tribology, the science of friction, is often considered to be a materials science phenomenon. This thesis, however, has demonstrated that the meso- and macro-scales of the friction problem play an (equally) important role. The applicability of fracture mechanics theory showed that the singular near-tip field and hence the macro-scale geometry are a key factor to the frictional response of the studied system. One might therefore conclude that this thesis contributes to the “revival of structural mechanics”.

8.1 Summary

Friction regularization is applied in many numerical simulations of interface slip either to solve the ill-posedness of Coulomb's friction law in certain bi-material systems or to eliminate numerical noise often present due to the non-continuous character of interfaces. One example of such a regularization, which originates from experimental observations, was analyzed in a set-up with an artificially nucleated slip pulse. By varying the characteristic length of the regularization, we showed that there is, for a given slip event, a critical length below which no regularizing effects are observed. The slip pulse propagates as if no regularization was applied and the interface was solely governed by Coulomb's friction law. This observation was confirmed by a study of the regularization's effect on the frequency domain of the slip front

Chapter 8. Concluding Remarks

showing that it behaves as a low-pass filter. Decreasing the length scale of the regularization results in a shift of the cutoff frequency to the domain of higher energy. This suggests that a slip pulse needs to contain sufficient energy in the temporal power spectrum density above the cutoff frequency in order to be measurably regularized. If one wishes to determine the physical length scale of a real interface, this knowledge provides a means to find the necessary “sharpness” of the slip event needed to make the measurement possible.

The stress state at the interface of friction experiments is usually, for various reasons, non-uniform, which affects the dynamics of propagating slip fronts. We presented the results of dynamic finite-element simulations mimicking an exact experimental set-up and confirmed the observations of Ben-David et al. (2010) that the rupture speed is closely related to the shear to normal traction ratio at the interface. However, we also showed that this relation is not perfectly unique and depends on the direction of propagation. Considering the dynamic (instead of the static) stress ratio close to the rupture tip improved the relation but could not close entirely the directionality gap. A change of the approach to a dynamic criterion based on energy considerations, however, was demonstrated to eliminate the directionality effect and to provide a unique rupture speed description.

In a similar set-up, but with a highly concentrated shear load, slip fronts tend to stop before reaching the edge of the interface. Slip arrest occurs because the concentrated external load leads to a concentrated energy accumulation which facilitates the nucleation of an interface rupture. While it propagates easily within the area of high strain energy, it soon penetrates zones of lower pre-stress and runs out of the necessary energy to continue its propagation. In the experiments of Rubinstein et al. (2007), this led to a sequence of slip precursors occurring before global sliding with propagation distances that scale non-linearly with the external shear force. The dynamic finite-element simulations presented in this thesis reproduced well the precursor load-length relation. In addition, with the objective of providing access to the fundamental mechanics of slip fronts, we presented a theoretical model based on linear elastic fracture mechanics which relies on the similarity of slip fronts and interface cracks. The theoretical prediction of the precursor load-length relation was shown to agree quantitatively well with experimental observations. Moreover, the theoretical model enabled additional insights on the observed phenomena and indicated that shear tractions due to a frustrated Poisson's expansion as well as the discrete nature of these slip events are the main sources of the non-linearity in the load-length relation.

In realistic systems, slip fronts propagate along interfaces that are characterized by various types of heterogeneities. We presented the results of dynamic three-dimensional finite-element simulations showing the propagation of slip fronts at interfaces with a structured heterogeneous area. The configuration of the heterogeneous area consisted of strips of higher and lower fracture energy leading in homogeneous systems to sub-Rayleigh and inter-sonic propagation, respectively. Two different propagation mechanisms were shown to occur depending on the wavelength of the heterogeneous configuration. The cause for this behavior was demonstrated to lie in the interaction between the length scales of the slip front and the

heterogeneous pattern. Estimations of the process zone size of the rupture indicated that the shear modulus and the slip-weakening rate are key parameters to the propagation regime occurring in a given system.

8.2 Outlook

The propagation of slip fronts has been studied in this thesis with modern finite-element simulations as well as theoretical models based on fracture mechanics theory. While the available tools have been successfully applied to improve our understanding of the mechanics of slip fronts, simplifications of the models or the set-up were sometimes necessary to gain insight on the studied phenomenon. These simplifications, however, open now new possibilities to improve the existing models and tools, and to deepen our current knowledge of frictional sliding.¹ Other opportunities for further work consist of applying these models on new (possibly more complex) problems that promise new advances in the understanding of slip front propagation. Some tracks for future developments and problems of interest are provided in this outlook.

The focus for the choice of the meso-scale friction laws applied in this thesis was on simplicity. The reason for this approach was the desire to explain the observed slip front behavior with fracture mechanics theory through the fracture energy of the interface, which is well defined for linear slip-weakening friction. This strategy was shown to be successful for instance for the prediction of the slip front arrest position. For other interface phenomena, such as frictional healing or slow fronts, simple friction laws might not be sufficient and more complex approaches could be required. Examples for friction laws which could be incorporated into finite-element simulations include velocity-weakening-strengthening laws (Bouchbinder et al., 2011), and rate- and state-dependent friction (Ruina, 1983).

The arrest of slip fronts in a system with a highly concentrated shear load was shown to be well predicted by a theoretical model based on linear elastic fracture mechanics. The proposed model, which applied uniform interface properties, was sufficient to compare with experimental data because this particular interface does not seem to be very heterogeneous, or at least is not much affected by the heterogeneity. Other systems, however, might well present a relevant heterogeneity which results in a less systematic response than the always increasing precursor length observed in the experiments by Rubinstein et al. (2007). Foreshocks of earthquakes, for instance, do not generally increase in a systematic way, which is possibly related to the heterogeneity of the fault. With the objective of studying the link between the variations of interface properties and the statistics of foreshock occurrence, the linear elastic fracture mechanics model could be enriched with a statistical distribution of fracture energy, fracture toughness, or both.

In the work presented in this thesis, the similarity between fracture mechanics and slip front

¹Conducting research is not a linear process.

Chapter 8. Concluding Remarks

propagation was used to develop a theoretical model to determine the arrest position of slip fronts. The good quantitative agreement with experimental data confirms the validity of this approach and suggests to apply it to other aspects of slip front propagation. For instance, the rupture speed was analyzed in Chapter 5 with stress-based as well as energy-based criteria but no description using fracture mechanics considerations was presented. It would be interesting to incorporate the dynamic contributions, as presented by Freund (1990), into the fracture mechanics model in order to study the propagation speed of slip fronts at an interface of non-uniform stress state. A fracture mechanics argument was already used to explain the existence of a quasi-static slow rupture occurring prior to dynamic ruptures (Kaneko and Ampuero, 2011). Extending this approach in combination with the fracture mechanics model for slip arrest could provide a different aspect to our understanding of rupture speed and add a new piece to the “fracture-friction similarity puzzle”.

Three-dimensional simulations of a system with a two-dimensional interface are, as mentioned in Chapter 7, challenging from a computational point of view if edge effects, disturbances due to reflected waves, and (too) large process zones are undesired. Systems which minimize these side effects limit considerably the possibilities of studying the influence of interface heterogeneity. The finite-element method, which was applied in this work, is computationally demanding because the entire solids, which have to be sufficient large to avoid effects due to reflected waves, are discretized and computed at every time step. Other methods, such as the spectral boundary integral method (Perrin et al., 1995; Geubelle and Rice, 1995), which limit discretization to the interface, are advantageous if interest is focused on the basic mechanism of slip fronts in a system with heterogeneous interface properties but homogeneous elastic bulk material. Recently, we used a modern two-dimensional implementation of the spectral boundary integral method to study frictional contact during the dynamic fracture of bi-material interfaces (Barras et al., 2014). A three-dimensional version is currently under development. With these numerical tools, the heterogeneous interface studied in Chapter 7 could be “complexified” and the propagation of slip fronts analyzed at interfaces with better performing or more realistic heterogeneity patterns. Possible examples include sinusoidal functions such as $\sin x \cdot \sin y$ to mimic an interface with regular asperities, specific shapes of stronger areas designed through engineering in order to improve frictional properties with minimal stronger areas (similar to the approach of Xia et al. (2012) for decohesion), and interfaces with random friction properties representing the statistical character of real systems.

In other cases, methods limited to the simulation of infinite two-dimensional interfaces between two semi-infinite elastic half-spaces are not sufficient to capture the essential mechanisms of slip front propagation. Interfaces between inelastic materials, for instance, require constitutive modeling of the bulk material. One example is off-fault plasticity, which has been studied in different two-dimensional set-ups (Templeton and Rice, 2008; DeDontney et al., 2012; Xu et al., 2012a,b) but has not been looked at in three-dimensional problems so far. Other cases in which the bulk plays an important role are materials with micro-structures such as grains or voids. Spatial variation of bulk material causes wave reflection at internal inter-

faces and could potentially “trap” kinetic energy close to the slip plane resulting in important modifications of the slip front dynamics. If computational resources prove to be insufficient for systems large enough to avoid wave reflections from the set-up boundaries, applying a layer of absorbing boundary conditions, such as developed by Komatitsch and Tromp (2003), could provide means to reduce the simulated model to a feasible size.

In view of more long-term goals, it is desirable to look at the propagation of slip fronts at a smaller scale than studied in the present thesis. Slip fronts propagate through interfaces that are in reality a set of micro-contacts created by the natural surface roughness of the solids. At this scale, the propagation of a slip front corresponds to a sequence of micro-contacts that transition from sticking to sliding. Simulations representing explicitly the surface roughness could provide new insights on the mechanics of slip fronts at the meso-scale. Ideally the roughness is modeled by asperities satisfying the statistical property of real surfaces. However, if such simulations are computationally out of reach, one could consider organized regular surface roughness as an intermediate step to gain a better understanding of meso-scale slip.

In conclusion, this thesis improved our knowledge of the mechanics of slip front propagation at frictional interfaces using numerical as well as theoretical models. In particular, the propagation speed, the position of arrest and heterogeneity effects at two-dimensional interfaces were studied in detail. Based on the gained understanding, the main path for future work concentrates on applying fracture mechanics concepts for the description of other aspects of slip front propagation and on complex heterogeneous systems approaching more realistic representation of real interfaces.

A Details to the Study of Regularized Friction

A.1 Description of the Nucleation Procedure

This section provides the details of the nucleation procedure applied in the simulations of which the results are presented in Chapter 4. This appendix was published as part of Kammer et al. (2014) and follows directly the description given in Appendix B of Cochard and Rice (2000). The procedure consists of an artificial change of the normal contact pressure in a spatial-temporal nucleation region of elliptic shape in the $x - t$ plane. The description is based on following coordinates:

$$\xi = (x - v_{\text{ell}} t) / a_{\text{ell}} \quad (\text{A.1})$$

$$\eta = (x + v_{\text{ell}} t) / b_{\text{ell}} - \eta_0 \quad (\text{A.2})$$

with $\eta_0 = \sqrt{a_{\text{ell}}^2 + b_{\text{ell}}^2} / b_{\text{ell}}$. The equation of the ellipse

$$1 - \xi^2 - \eta^2 = 0 \quad (\text{A.3})$$

defines the boundary of the nucleation zone, in which the change of the contact pressure is created by adding an artificial pressure \bar{p}_a (of opposite sign of \bar{p}) to the initial contact pressure \bar{p} . The artificial pressure is defined by

$$\bar{p}_a = -\alpha \bar{p} (1 - \xi^2 - \eta^2)^2 \quad (\text{A.4})$$

where $0 < \alpha < 1$ is the maximal contact pressure change with respect to \bar{p} . Outside as well as at the boundary, the contact pressure is equal to the remote, uniform, compressive normal load \bar{p} . Thus, the contact pressure decreases smoothly from \bar{p} at the boundary down to $(1 - \alpha) \bar{p}$ at the centre of the ellipse. Here, we choose $\alpha = 0.8$ in order to avoid interface opening, which is not desirable to be consistent with previous studies. The normalized artificial pressure \bar{p}_a / \bar{p} in the nucleation domain is shown in Figure A.1.

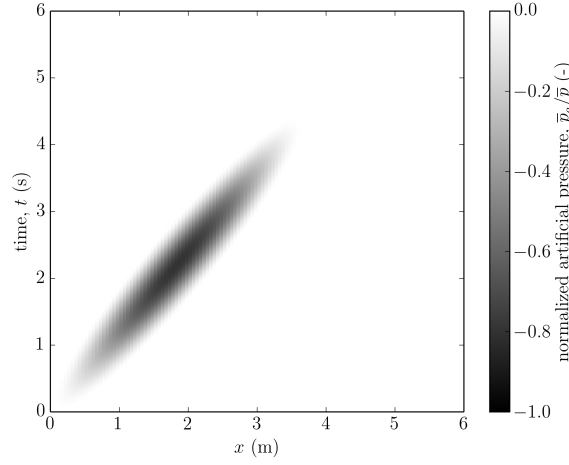


Figure A.1: The normalised artificial pressure \bar{p}_a/\bar{p} imposed at the interface is shown for the simulation presented in Figure 4.2. The spatial-temporal region of nucleation is of elliptic shape in the $x - t$ plane.

A.2 Regularization: Derivation of the Analytical Solution

In order to improve readability of the derivation, we substitute the physical denotations by the following symbols: Coulomb friction $x = \tau^s$, regularized frictional strength $y = \tau^{es}$, Prakash-Clifton parameters $C = -(v_{pc} + \delta)/d_{pc}$, and use the angular frequency $\omega = 2\pi f$. The simplified Prakash and Clifton (1993b) law as given by (4.1) becomes

$$\dot{y}(t) = C(y(t) - x(t)) . \quad (\text{A.5})$$

Taking a Laplace transform in time, we can rewrite (A.5) as

$$\hat{y}(s) = \frac{-C}{s - C} \hat{x}(s) \quad (\text{A.6})$$

with initial condition $y(0) = 0$. Performing an inverse Laplace transform back to the time domain for $t > 0$, we find

$$y(t) = \int_0^t -C \exp(C\tau) \cdot x(t - \tau) d\tau . \quad (\text{A.7})$$

Considering a sinusoidal input signal, we define

$$x(t) = x_0 + A^s \text{Im}(\exp i\omega t) . \quad (\text{A.8})$$

We then substitute (A.8) into (A.7) and simplify to

$$y(t) = -x_0 [\exp Ct - 1] + \text{Im} \left[\frac{-C \exp i\omega t}{C - i\omega} A^s [\exp(C - i\omega)t - 1] \right] . \quad (\text{A.9})$$

A.2. Regularization: Derivation of the Analytical Solution

Knowing that $C < 0$, we compute the steady-state solution of $y(t)$ for $t \rightarrow \infty$

$$y_{\infty}(t) = x_0 + \frac{A^s}{\sqrt{1 + \left(\frac{\omega}{C}\right)^2}} \sin\left(\omega t + \arctan\frac{\omega}{C}\right). \quad (\text{A.10})$$

The steady-state output signal is therefore also a sinusoidal signal around the same average value x_0 and with the same (angular) frequency ω . The phase offset is $\phi = \arctan\omega/C$ and the amplitude is

$$A^{\text{es}} = \frac{A^s}{\sqrt{1 + \left(\frac{\omega}{C}\right)^2}}. \quad (\text{A.11})$$

Bibliography

Abraham, F. F. and H. Gao

2000. How fast can cracks propagate? *Physical Review Letters*, 84(14):3113–3116.

Achenbach, J. D.

1973. *Wave Propagation in Elastic Solids*, volume 16 of *Applied Mathematics and Mechanics*. Amsterdam: North Holland.

Adams, G. G.

1995. Self-excited oscillations of two elastic half-spaces sliding with a constant coefficient of friction. *Journal of Applied Mechanics*, 62(4):867–872.

Adda-Bedia, M. and M. Ben Amar

2003. Self-sustained slip pulses of finite size between dissimilar materials. *Journal of the Mechanics and Physics of Solids*, 51(10):1849.

Amontons, G.

1699. De la résistance causée dans les machines. *Memoires de l'Academie Royale A*, Pp. 275–282.

Ampuero, J.-P.

2002. *Etude physique et numérique de la nucléation des séismes*. PhD thesis, Université Paris 7 - Denis Diderot - UFR des Sciences Physiques de la Terre, Paris.

Ampuero, J. P., J. Ripperger, and P. M. Mai

2006. Properties of dynamic earthquake ruptures with heterogeneous stress drop. In *Earthquakes: Radiated Energy and the Physics of Faulting*, R. Abercrombie, A. McGarr, G. DiToro, and H. Kanamori, eds., volume 170 of *Geophysical Monograph Series*, Pp. 255–261, Washington DC. AMER Geophysical Union. Conference on Radiated Energy and the Physics of Earthquake Faulting, Portland, ME, JUN, 2005.

Amundsen, D. S., J. Scheibert, K. Thøgersen, J. Trømborg, and A. Malthe-Sørensen

2012. 1d model of precursors to frictional stick-slip motion allowing for robust comparison with experiments. *Tribology Letters*, 45(2):357.

Bibliography

- Anderson, T. L.
2005. *Fracture Mechanics: Fundamentals and Applications*, third edition edition. Boca Raton: CRC Press, Taylor & Francis Group.
- Andrews, D.
1976a. Rupture propagation with finite stress in antiplane strain. *Journal of Geophysical Research*, 81(20):3575–3582.
- Andrews, D. J.
1973. A numerical study of tectonic stress release by underground explosions. *Bulletin of the Seismological Society of America*, 63(4):1375–1391.
- Andrews, D. J.
1976b. Rupture velocity of plane strain shear cracks. *Journal of Geophysical Research*, 81(32):5679–5687.
- Andrews, D. J.
1999. Test of two methods for faulting in finite-difference calculations. *Bulletin of the Seismological Society of America*, 89(4):931–937.
- Andrews, D. J.
2005. Rupture dynamics with energy loss outside the slip zone. *Journal of Geophysical Research*, 110:B01307.
- Andrews, D. J. and Y. Ben-Zion
1997. Wrinkle-like slip pulse on a fault between different materials. *Journal of Geophysical Research*, 102(B1):553–571.
- Anooshehpour, A. and J. N. Brune
1999. Wrinkle-like weertman pulse at the interface between two blocks of foam rubber with different velocities. *Geophysical Research Letters*, 26(13):2025–2028.
- Ariyoshi, K., T. Hori, J.-P. Ampuero, Y. Kaneda, T. Matsuzawa, R. Hino, and A. Hasegawa
2009. Influence of interaction between small asperities on various types of slow earthquakes in a 3-d simulation for a subduction plate boundary. *Gondwana Research*, 16(3–4):534–544.
- Ariyoshi, K., T. Matsuzawa, J.-P. Ampuero, R. Nakata, T. Hori, Y. Kaneda, R. Hino, and A. Hasegawa
2012. Migration process of very low-frequency events based on a chain-reaction model and its application to the detection of preseismic slip for megathrust earthquakes. *Earth Planets and Space*, 64(8):693–702.
- Bar Sinai, Y., E. A. Brener, and E. Bouchbinder
2012. Slow rupture of frictional interfaces. *Geophysical Research Letters*, 39(3):L03308.
- Bar-Sinai, Y., R. Spatschek, E. A. Brener, and E. Bouchbinder
2014. On the velocity-strengthening behavior of dry friction. *Journal of Geophysical Research: Solid Earth*, 119(3):1738–1748.

- Barenblatt, G. I.
1959. The formation of equilibrium cracks during brittle fracture. general ideas and hypotheses. axially-symmetric cracks. *Journal of Applied Mathematics and Mechanics*, 23(3):622–636.
- Barras, F., D. S. Kammer, P. H. Geubelle, and J.-F. Molinari
2014. A study of frictional contact in dynamic fracture along bimaterial interfaces. *International Journal of Fracture*, (in press).
- Baumberger, T., C. Caroli, and O. Ronsin
2002. Self-healing slip pulses along a gel/glass interface. *Physical Review Letters*, 88(7):075509.
- Baumberger, T., C. Caroli, and O. Ronsin
2003. Self-healing slip pulses and the friction of gelatin gels. *European Physical Journal E*, 11(1):85–93.
- Baumberger, T., F. Heslot, and B. Perrin
1994. Crossover from creep to inertial motion in friction dynamics. *Nature*, 367(6463):544.
- Belytschko, T., W. K. Liu, and B. Moran
2000. *Nonlinear Finite Elements for Continua and Structures*. Chichester: John Wiley & Sons.
- Ben-David, O., G. Cohen, and J. Fineberg
2010. The dynamics of the onset of frictional slip. *Science*, 330(6001):211.
- Ben-David, O. and J. Fineberg
2011. Static friction coefficient is not a material constant. *Physical Review Letters*, 106(25):254301.
- Ben-Zion, Y. and Y. Huang
2002. Dynamic rupture on an interface between a compliant fault zone layer and a stiffer surrounding solid. *Journal of Geophysical Research*, 107(B2).
- Ben-Zion, Y. and J. R. Rice
1997. Dynamic simulations of slip on a smooth fault in an elastic solid. *Journal of Geophysical Research - Solid Earth*, 102(B8):17771–17784.
- Blau, P. J.
2009. *Friction Science and Technology*, 2nd edition. Boca Raton: CRC Press.
- Bouchaud, E., J. P. Bouchaud, D. S. Fisher, S. Ramanathan, and J. R. Rice
2002. Can crack front waves explain the roughness of cracks? *Journal of the Mechanics and Physics of Solids*, 50(8):1703–1725.
- Bouchbinder, E., E. A. Brener, I. Barel, and M. Urbakh
2011. Slow cracklike dynamics at the onset of frictional sliding. *Physical Review Letters*, 107(23):235501.

Bibliography

- Bowden, F and D. Tabor
1942a. Mechanism of metallic friction. *Nature*, 150:197–199.
- Bowden, F. P. and D. Tabor
1942b. The theory of metallic friction and the role of shearing and ploughing. In *Bulletin 145*. Comm. of Australia, Council Sci. and Ind. Research.
- Bower, A. F.
2009. *Applied Mechanics of Solids*. Boca Raton: CRC Press, Taylor & Francis Group.
- Braun, O., I. Barel, and M. Urbakh
2009. Dynamics of transition from static to kinetic friction. *Physical Review Letters*, 103(19):194301.
- Brietzke, G. B., A. Cochard, and H. Igel
2007. Dynamic rupture along bimaterial interfaces in 3d. *Geophysical Research Letters*, 34(11):L11305.
- Brietzke, G. B., A. Cochard, and H. Igel
2009. Importance of bimaterial interfaces for earthquake dynamics and strong ground motion. *Geophysical Journal International*, 178(2):921.
- Broberg, K. B.
1989. The near-tip field at high crack velocities. *International Journal of Fracture*, 39(1-3):1–13.
- Brörmann, K., I. Barel, M. Urbakh, and R. Bennewitz
2013. Friction on a microstructured elastomer surface. *Tribology Letters*, 50(1):3–15.
- Burridge, R.
1973. Admissible speeds for plane-strain self-similar shear cracks with friction but lacking cohesion. *Geophysical Journal International*, 35(4):439–455.
- Burridge, R., G. Conn, and L. B. Freund
1979. The stability of a rapid mode II shear crack with finite cohesive traction. *Journal of Geophysical Research: Solid Earth*, 84(B5):2210–2222.
- Burridge, R. and L. Knopoff
1967. Model and theoretical seismicity. *Bulletin of the Seismological Society of America*, 57(3):341–371.
- Burwell, J. T. and E. Rabinowicz
1953. The nature of the coefficient of friction. *Journal of Applied Physics*, 24(2):136.
- Carlson, J. M. and J. S. Langer
1989. Properties of earthquakes generated by fault dynamics. *Physical Review Letters*, 62(22):2632–2635.

- Carpenter, N. J., R. L. Taylor, and M. G. Katona
1991. Lagrange constraints for transient finite element surface contact. *International Journal for Numerical Methods in Engineering*, 32(1):103.
- Caughey, T. K.
1960. Classical normal modes in damped linear dynamic systems. *Journal of Applied Mechanics*, 27(2):269–271.
- Chopin, J., A. Prevost, A. Boudaoud, and M. Adda-Bedia
2011. Crack front dynamics across a single heterogeneity. *Physical Review Letters*, 107(14):144301.
- Ciccotti, M. and F. Mulargia
2004. Differences between static and dynamic elastic moduli of a typical seismogenic rock. *Geophysical Journal International*, 157(1):474.
- Cochard, A. and J. R. Rice
2000. Fault rupture between dissimilar materials: Ill-posedness, regularization, and slip-pulse response. *Journal of Geophysical Research*, 105(B11):25891.
- Coker, D., G. Lykotrafitis, A. Needleman, and A. J. Rosakis
2005. Frictional sliding modes along an interface between identical elastic plates subject to shear impact loading. *Journal of the Mechanics and Physics of Solids*, 53(4):884–922.
- Coker, D., A. J. Rosakis, and A. Needleman
2003. Dynamic crack growth along a polymer composite-homalite interface. *Journal of the Mechanics and Physics of Solids*, 51(3):425–460.
- Coulomb, C. A.
1785. Théorie des machines simples, en ayant regard au frottement de leurs parties, et à la roideur des cordages. *Memoires de Mathematique et de Physique de l'Academie Royale*, Pp. 161–342.
- Curnier, A.
2000. *Méthodes numériques en mécanique des solides*, 2nd edition. Lausanne, Switzerland: Presses polytechniques et universitaires romandes.
- Curnier, A.
2007. Contact mechanics and nonsmooth tribology. Ecole Polytechnique Fédérale de Lausanne (EPFL).
- Dalmas, D., E. Barthel, and D. Vandembroucq
2009. Crack front pinning by design in planar heterogeneous interfaces. *Journal of the Mechanics and Physics of Solids*, 57(3):446–457.
- Das, S. and K. Aki
1977. Fault plane with barriers: A versatile earthquake model. *Journal of Geophysical Research*, 82(36):5658–5670.

Bibliography

- Day, S. M.
1982a. Three-dimensional finite difference simulation of fault dynamics: Rectangular faults with fixed rupture velocity. *Bulletin of the Seismological Society of America*, 72(3):705–727.
- Day, S. M.
1982b. Three-dimensional simulation of spontaneous rupture: The effect of nonuniform prestress. *Bulletin of the Seismological Society of America*, 72(6A):1881–1902.
- Day, S. M., L. A. Dalgner, N. Lapusta, and Y. Liu
2005. Comparison of finite difference and boundary integral solutions to three-dimensional spontaneous rupture. *Journal of Geophysical Research*, 110(B12):B12307.
- DeDontney, N., J. R. Rice, and R. Dmowska
2011. Influence of material contrast on fault branching behavior. *Geophysical Research Letters*, 38(14):L14305.
- DeDontney, N., J. R. Rice, and R. Dmowska
2012. Finite element modeling of branched ruptures including off-fault plasticity. *Bulletin of the Seismological Society of America*, 102(2):541.
- Di Bartolomeo, M., F. Massi, L. Baillet, A. Culla, A. Fregolent, and Y. Berthier
2012. Wave and rupture propagation at frictional bimaterial sliding interfaces: From local to global dynamics, from stick-slip to continuous sliding. *Tribology International*, 52(0):117–131.
- Di Bartolomeo, M., A. Meziane, F. Massi, L. Baillet, and A. Fregolent
2010. Dynamic rupture at a frictional interface between dissimilar materials with asperities. *Tribology International*, 43(9):1620.
- Di Toro, G., D. L. Goldsby, and T. E. Tullis
2004. Friction falls towards zero in quartz rock as slip velocity approaches seismic rates. *Nature*, 427(6973):436–9.
- Dieterich, J. H.
1972. Time-dependent friction in rocks. *Journal of Geophysical Research*, 77(20):3690.
- Dieterich, J. H.
1978. Time-dependent friction and the mechanics of stick-slip. *Pure and Applied Geophysics*, 116(4-5):790.
- Dieterich, J. H.
1979. Modeling of rock friction 1. experimental results and constitutive equations. *Journal of Geophysical Research*, 84:2161–2168.
- Dieterich, J. H. and B. D. Kilgore
1994. Direct observation of frictional contacts: New insights for state-dependent properties. *Pure and Applied Geophysics*, 143(1):283–302. 10.1007/BF00874332.

- Dunham, E. M., P. Favreau, and J. M. Carlson
2003. A supershear transition mechanism for cracks. *Science*, 299(5612):1557–9.
- Freund, L.
1990. *Dynamic Fracture Mechanics*. New York: Cambridge University Press.
- Freund, L. B.
1979. The mechanics of dynamic shear crack propagation. *Journal of Geophysical Research: Solid Earth*, 84(B5):2199–2209.
- Fukuyama, E. and K. B. Olsen
2002. A condition for super-shear rupture propagation in a heterogeneous stress field. *pure and applied geophysics*, 159(9):2047–2056.
- Garagash, D. I. and L. N. Germanovich
2012. Nucleation and arrest of dynamic slip on a pressurized fault. *Journal of Geophysical Research*, 117(B10):B10310.
- Geubelle, P. H. and D. V. Kubair
2001. Intersonic crack propagation in homogeneous media under shear-dominated loading: numerical analysis. *Journal of the Mechanics and Physics of Solids*, 49(3):571–587.
- Geubelle, P. H. and J. R. Rice
1995. A spectral method for three-dimensional elastodynamic fracture problems. *Journal of the Mechanics and Physics of Solids*, 43(11):1791–1824.
- Goldsby, D. L. and T. E. Tullis
2011. Flash heating leads to low frictional strength of crustal rocks at earthquake slip rates. *Science*, 334(6053):216–8.
- Griebel, M., S. Knapek, and G. Zumbusch
2007. *Numerical Simulation in Molecular Dynamics: Numerics, Algorithms, Parallelization, Applications (Texts in Computational Science and Engineering)*. Springer.
- Griffith, A. A.
1920. The phenomena of rupture and flow in solids. *Philosophical Transactions of the Royal Society of London, Series A: Mathematical, Physical and Engineering Sciences*, 221:163–198.
- Harris, R. A. and S. M. Day
1997. Effects of a low-velocity zone on a dynamic rupture. *Bulletin of the Seismological Society of America*, 87(5):1267–1280.
- Heaton, T. H.
1990. Evidence for and implications of self-healing pulses of slip in earthquake rupture. *Physics of the Earth and Planetary Interiors*, 64(1):1–20.

Bibliography

- Heslot, F., T. Baumberger, B. Perrin, B. Caroli, and C. Caroli
1994. Creep, stick-slip, and dry-friction dynamics: Experiments and a heuristic model. *Physical Review E*, 49(6):4973–4988.
- Holm, R.
1938. The friction force over the real area of contact (in german). *Wissenschaftliche Veröffentlichungen aus den Siemens-Werken*, 17(4):38–42.
- Holzappel, G. A.
2000. *Nonlinear solid mechanics: a continuum approach for engineering*. Baffins Lane, Chichester, West Sussex, England: John Wiley & Sons Ltd.
- Ida, Y.
1972. Cohesive force across the tip of a longitudinal-shear crack and griffith's specific surface energy. *Journal of Geophysical Research*, 77(20):3796–3805.
- Irwin, G. R.
1956. Onset of fast crack propagation in high strength steel and aluminium alloys. In *Sagamore Research Conference Proceedings*, Pp. 289–305.
- Irwin, G. R.
1957. Analysis of stresses and strains near the end of a crack traversing a plate. *Journal of Applied Mechanics*, 24:361–364.
- Jost, P.
1966. Lubrication (tribology): A report on the present position and industry's needs. Technical report, Department of Education and Science, London.
- Kammer, D. S., V. A. Yastrebov, G. Anciaux, and J. F. Molinari
2014. The existence of a critical length scale in regularised friction. *Journal of the Mechanics and Physics of Solids*, 63(0):40–50.
- Kammer, D. S., V. A. Yastrebov, P. Spijker, and J.-F. Molinari
2012. On the propagation of slip fronts at frictional interfaces. *Tribology Letters*, 48(1):27–32.
- Kaneko, Y. and J.-P. Ampuero
2011. A mechanism for preseismic steady rupture fronts observed in laboratory experiments. *Geophysical Research Letters*, 38(21):L21307.
- Kaneko, Y., N. Lapusta, and J.-P. Ampuero
2008. Spectral element modeling of spontaneous earthquake rupture on rate and state faults: Effect of velocity-strengthening friction at shallow depths. *Journal of Geophysical Research*, 113(B9):B09317.
- Kato, N.
2012. Fracture energies at the rupture nucleation points of large interplate earthquakes. *Earth and Planetary Science Letters*, 353–354(0):190–197.

- Kikuchi, N. and J. Oden
1988. *Contact Problems in Elasticity: A Study of Variational Inequalities and Finite Element Methods*. Philadelphia: SIAM.
- Kilgore, B., J. Lozos, N. Beeler, and D. Oglesby
2012. Laboratory observations of fault strength in response to changes in normal stress. *Journal of Applied Mechanics*, 79:031007–1.
- Komatitsch, D. and J. Tromp
2003. A perfectly matched layer absorbing boundary condition for the second-order seismic wave equation. *Geophysical Journal International*, 154(1):146–153.
- Kragelskii, I.
1965. *Friction and Wear*. Washington, D.C.: Butterworths.
- Lachenbruch, A. H. and J. H. Sass
1980. Heat flow and energetics of the san andreas fault zone. *Journal of Geophysical Research*, 85(B11):6185.
- Lambros, J. and A. J. Rosakis
1995. Shear dominated transonic interfacial crack growth in a bimaterial-i. experimental observations. *Journal of the Mechanics and Physics of Solids*, 43(2):169–188.
- Lapusta, N., J. R. Rice, Y. Ben-Zion, and G. T. Zheng
2000. Elastodynamic analysis for slow tectonic loading with spontaneous rupture episodes on faults with rate- and state-dependent friction. *Journal of Geophysical Research*, 105(B10):23765–23789.
- Latour, S., C. Voisin, F. Renard, E. Larose, S. Catheline, and M. Campillo
2013. Effect of fault heterogeneity on rupture dynamics: An experimental approach using ultrafast ultrasonic imaging. *Journal of Geophysical Research: Solid Earth*, 118(11):5888–5902.
- Laursen, T. A.
2003. *Computational Contact and Impact Mechanics: Fundamentals of Modeling Interfacial Phenomena in Nonlinear Finite Element Analysis*, 2nd edition. Berlin, Heidelberg, Germany: Springer-Verlag.
- Liu, C., Y. Huang, and A. J. Rosakis
1995. Shear dominated transonic interfacial crack growth in a bimaterial i-ii. asymptotic fields and favorable velocity regimes. *Journal of the Mechanics and Physics of Solids*, 43(2):189–206.
- Liu, Y. and N. Lapusta
2008. Transition of mode ii cracks from sub-rayleigh to intersonic speeds in the presence of favorable heterogeneity. *Journal of the Mechanics and Physics of Solids*, 56(1):25.

Bibliography

LSMS-EPFL

2014. Akantu. <http://lsms.epfl.ch/akantu>. Accessed: 2014-09-16.

Lu, X., N. Lapusta, and A. Rosakis

2010. Pulse-like and crack-like dynamic shear ruptures on frictional interfaces: experimental evidence, numerical modeling, and implications. *International Journal of Fracture*, 163(1):27–39.

Lu, X., N. Lapusta, and A. J. Rosakis

2007. Pulse-like and crack-like ruptures in experiments mimicking crustal earthquakes. *Proceedings of the National Academy of Sciences of the United States of America*, 104(48):18931–6.

Lu, X., N. Lapusta, and A. J. Rosakis

2009. Analysis of supershear transition regimes in rupture experiments: the effect of nucleation conditions and friction parameters. *Geophysical Journal International*, 177(2):717.

Lykotrafitis, G., A. J. Rosakis, and G. Ravichandran

2006. Self-healing pulse-like shear ruptures in the laboratory. *Science*, 313(5794):1765–8.

Madariaga, R. and K. B. Olsen

2000. Criticality of rupture dynamics in 3-d. *pure and applied geophysics*, 157(11-12):1981–2001.

Maegawa, S., A. Suzuki, and K. Nakano

2010. Precursors of global slip in a longitudinal line contact under non-uniform normal loading. *Tribology Letters*, 38(3):313.

Måløy, K., S. Santucci, J. Schmittbuhl, and R. Toussaint

2006. Local waiting time fluctuations along a randomly pinned crack front. *Physical Review Letters*, 96(4):045501.

Martins, J. and F. Simões

1995. On some sources of instability/ill-posedness in elasticity problems with coulomb's friction. In *Contact Mechanics*, M. Raous, M. Jean, and J. Moreau, eds., Pp. 95–106, New York. Plenum.

Martins, J. A. C., J. Guimara*es, and L. O. Faria

1995. Dynamic surface solutions in linear elasticity and viscoelasticity with frictional boundary conditions. *Journal of Vibration and Acoustics*, 117(4):445.

Mower, T. M. and A. S. Argon

1995. Experimental investigations of crack trapping in brittle heterogeneous solids. *Mechanics of Materials*, 19(4):343–364.

Needleman, A.

1999. An analysis of intersonic crack growth under shear loading. *Journal of Applied Mechanics*, 66(4):847–857.

- Newmark, N. M.
1959. A method for computation of structural dynamics. *Proceedings of the American Society of Civil Engineers*, 85(3):67–94.
- Nielsen, S., J. Taddeucci, and S. Vinciguerra
2010. Experimental observation of stick-slip instability fronts. *Geophysical Journal International*, 180(2):697.
- Otsuki, M. and H. Matsukawa
2013. Systematic breakdown of amontons' law of friction for an elastic object locally obeying amontons' law. *Scientific Reports*, 3:1586.
- Page, M. T., E. M. Dunham, and J. M. Carlson
2005. Distinguishing barriers and asperities in near-source ground motion. *Journal of Geophysical Research: Solid Earth*, 110(B11).
- Palmer, A. C. and J. R. Rice
1973. The growth of slip surfaces in the progressive failure of over-consolidated clay. *Proceedings of the Royal Society of London. Series A. Mathematical and Physical Sciences*, 332(1591):527–548.
- Patera, A. T.
1984. A spectral element method for fluid dynamics: Laminar flow in a channel expansion. *Journal of Computational Physics*, 54(3):468–488.
- Perrin, G., J. R. Rice, and G. Zheng
1995. Self-healing slip pulse on a frictional surface. *Journal of the Mechanics and Physics of Solids*, 43(9):1461–1495.
- Persson, B. N. J.
1994. Theory of friction: The role of elasticity in boundary lubrication. *Physical Review B*, 50(7):4771–4786.
- Ponson, L.
2009. Depinning transition in the failure of inhomogeneous brittle materials. *Phys. Rev. Lett.*, 103(5):055501.
- Prakash, V.
1998. Frictional response of sliding interfaces subjected to time varying normal pressures. *Journal of Tribology*, 120(1):97–102.
- Prakash, V. and R. J. Clifton
1993a. Pressure-shear plate impact measurement of dynamic friction for high speed machining applications. In *Proceedings of the Seventh International Congress on Experimental Mechanics*, Pp. 556–564.

Bibliography

Prakash, V. and R. J. Clifton

1993b. Time resolved dynamic friction measurements in pressure-shear. In *Experimental Techniques in the Dynamics of Deformable Solids, AMD-vol. 165*, K. Ramesh, ed., Pp. 33–48, New York. ASME.

Rabinowicz, E.

1956. Autocorrelation analysis of the sliding process. *Journal of Applied Physics*, 27(2):131–135.

Rabinowicz, E.

1965. *Friction and Wear of Materials*. Wiley, New York.

Rabinowicz, E.

1992. Friction coefficients of noble metals over a range of loads. *Wear*, 159(1):89–94.

Radiguet, M., D. S. Kammer, P. Gillet, and J.-F. Molinari

2013. Survival of heterogeneous stress distributions created by precursory slip at frictional interfaces. *Physical Review Letters*, 111(16):164302.

Radiguet, M., D. S. Kammer, and J.-F. Molinari

2014. The role of viscoelasticity on heterogeneous stress fields at frictional interfaces. in press at *Mechanics of Materials*.

Ramanathan, S., D. Ertas, and D. S. Fisher

1997. Quasistatic crack propagation in heterogeneous media. *Physical Review Letters*, 79(5):873–876.

Ramanathan, S. and D. S. Fisher

1997. Dynamics and instabilities of planar tensile cracks in heterogeneous media. *Physical Review Letters*, 79(5):877–880.

Ramanathan, S. and D. S. Fisher

1998. Onset of propagation of planar cracks in heterogeneous media. *Physical Review B*, 58(10):6026–6046.

Ranjith, K. and J. R. Rice

2001. Slip dynamics at an interface between dissimilar materials. *Journal of the Mechanics and Physics of Solids*, 49(2):341–361.

Rayleigh, J. W. S.

1945. *The Theory of Sound*, volume one, second edition. New York: Dover Publications.

Read, B. E. and J. C. Duncan

1981. Measurement of dynamic properties of polymeric glasses for different modes of deformation. *Polymer Testing*, 2(2):135–150.

- Reches, Z. and D. A. Lockner
2010. Fault weakening and earthquake instability by powder lubrication. *Nature*, 467(7314):452–5.
- Renardy, M.
1992. Ill-posedness at the boundary for elastic solids sliding under coulomb friction. *Journal of Elasticity*, 27(3):281.
- Rice, J. R.
1979. The mechanics of quasi-static crack growth. In *Proceedings of the Eighth U.S. National Congress of Applied Mechanics*, R. Kelly, ed., Pp. 191–216, North Hollywood, California. Western Periodicals Co.
- Rice, J. R.
1980. The mechanics of earthquake rupture. In *Physics of the Earth's Interior*, A. Dziewonski and E. Boschi, eds., Pp. 555–649.
- Rice, J. R.
1993. Spatio-temporal complexity of slip on a fault. *Journal of Geophysical Research*, 98(B6):9885.
- Rice, J. R. and A. L. Ruina
1983. Stability of steady frictional slipping. *Journal of Applied Mechanics*, 50(2):343.
- Richart, N. and J. Molinari
2014. Implementation of a parallel finite-element library: test case on a non-local continuum damage model. submitted.
- Romero, V., E. Wandersman, G. Debrégeas, and A. Prevost
2014. Probing locally the onset of slippage at a model multicontact interface. *Phys. Rev. Lett.*, 112(9):094301.
- Rosakis, A. J., O. Samudrala, and D. Coker
1999. Cracks faster than the shear wave speed. *Science*, 284(5418):1337–1340.
- Rubin, A. M. and J.-P. Ampuero
2007. Aftershock asymmetry on a bimaterial interface. *Journal of Geophysical Research*, 112(B5):B05307.
- Rubinstein, S., G. Cohen, and J. Fineberg
2007. Dynamics of precursors to frictional sliding. *Physical Review Letters*, 98(22):226103.
- Rubinstein, S. M., G. Cohen, and J. Fineberg
2004. Detachment fronts and the onset of dynamic friction. *Nature*, 430(7003):1005–9.
- Rubinstein, S. M., G. Cohen, and J. Fineberg
2008. Cracklike processes within frictional motion: Is slow frictional sliding really a slow process? *MRS Bulletin*, 33(12):1181.

Bibliography

- Ruina, A. L.
1983. Slip instability and state variable friction laws. *Journal of Geophysical Research*, 88(B12):10359.
- Samudrala, O., Y. Huang, and A. J. Rosakis
2002. Subsonic and intersonic shear rupture of weak planes with a velocity weakening cohesive zone. *Journal of Geophysical Research: Solid Earth*, 107(B8):-7.
- Schallamach, A.
1971. How does rubber slide? *Wear*, 17(4):301–312.
- Scheibert, J. and D. K. Dysthe
2010. Role of friction-induced torque in stick-slip motion. *Europhysics Letters*, 92(5):54001.
- Scholz, C. H.
2002. *The Mechanics of Earthquakes and Faulting*, 2nd edition. Cambridge: Cambridge University Press.
- Shi, Z. and Y. Ben-Zion
2006. Dynamic rupture on a bimaterial interface governed by slip-weakening friction. *Geophysical Journal International*, 165(2):469.
- Simo, J. and T. Hughes
1998. *Computational Inelasticity*, volume 7 of *Interdisciplinary Applied Mathematics*. New York: Springer-Verlag.
- Spijker, P., G. Anciaux, and J.-F. Molinari
2011. Dry sliding contact between rough surfaces at the atomistic scale. *Tribology Letters*, 44(2):279–285.
- Svetlizky, I. and J. Fineberg
2014. Classical shear cracks drive the onset of dry frictional motion. *Nature*, 509:205–208.
- Tada, H., P. C. Paris, and G. R. Irwin
2000. *The Stress Analysis of Cracks Handbook*, third edition. New York: ASME.
- Templeton, E. L. and J. R. Rice
2008. Off-fault plasticity and earthquake rupture dynamics: 1. dry materials or neglect of fluid pressure changes. *Journal of Geophysical Research*, 113(B9):B09306.
- Thomas, J.
1995. *Numerical Partial Differential Equations: Finite Difference Methods*, Texts in Applied Mathematics, 1st edition. Springer.
- Trømborg, J., J. Scheibert, D. Amundsen, K. Thøgersen, and A. Malthé-Sørensen
2011. Transition from static to kinetic friction: Insights from a 2d model. *Physical Review Letters*, 107(7):074301.

- Trømborg, J. K., H. A. Sveinsson, J. Scheibert, K. Thøgersen, D. S. Amundsen, and A. Malthe-Sørenssen
2014. Slow slip and the transition from fast to slow fronts in the rupture of frictional interfaces. *Proceedings of the National Academy of Sciences of the United States of America*, 111(24):8764–8769.
- Uenishi, K. and J. R. Rice
2003. Universal nucleation length for slip-weakening rupture instability under nonuniform fault loading. *Journal of Geophysical Research*, 108(B1):B12042.
- Voisin, C., I. Ionescu, and M. Campillo
2002. Crack growth resistance and dynamic rupture arrest under slip dependent friction. *Physics of the Earth and Planetary Interiors*, 131(3–4):279–294.
- Weertman, J.
1980. Unstable slippage across a fault that separates elastic media of different elastic constants. *Journal of Geophysical Research*, 85(B3):1455.
- Wriggers, P.
2006. *Computational Contact Mechanics*, 2nd edition. Berlin, Heidelberg, Germany: Springer-Verlag.
- Xia, K., A. J. Rosakis, and H. Kanamori
2004. Laboratory earthquakes: the sub-rayleigh-to-supershear rupture transition. *Science*, 303(5665):1859–61.
- Xia, K., A. J. Rosakis, H. Kanamori, and J. R. Rice
2005. Laboratory earthquakes along inhomogeneous faults: directionality and supershear. *Science*, 308(5722):681–4.
- Xia, S., L. Ponson, G. Ravichandran, and K. Bhattacharya
2012. Toughening and asymmetry in peeling of heterogeneous adhesives. *Physical Review Letters*, 108(19):196101.
- Xu, S., Y. Ben-Zion, and J.-P. Ampuero
2012a. Properties of inelastic yielding zones generated by in-plane dynamic ruptures—i. model description and basic results. *Geophysical Journal International*, 191(3):1325–1342.
- Xu, S., Y. Ben-Zion, and J.-P. Ampuero
2012b. Properties of inelastic yielding zones generated by in-plane dynamic ruptures—ii. detailed parameter-space study. *Geophysical Journal International*, 191(3):1343–1360.
- Xu, X. P. and A. Needleman
1995. Numerical simulations of dynamic crack growth along an interface. *International Journal of Fracture*, 74(4):289–324.

Bibliography

- Yamaguchi, T., M. Morishita, M. Doi, T. Hori, H. Sakaguchi, and J.-P. Ampuero
2011. Gutenberg-richter's law in sliding friction of gels. *Journal of Geophysical Research: Solid Earth*, 116(B12).
- Yastrebov, V. A.
2013. *Numerical Methods in Contact Mechanics*. London UK / Hoboken USA: ISTE - John Wiley & Sons, Inc.
- Zienkiewicz, O. and R. Taylor
2000. *The Finite Element Method: Solid Mechanics*, volume 2, fifth edition. Woburn MA, USA: Butterworth-Heinemann.

David S. Kammer

Computational Solid Mechanics Laboratory
School of Architecture, Civil and Environmental Engineering
Ecole Polytechnique Fédérale de Lausanne
CH - 1015 Lausanne, Switzerland

Education

Ecole Polytechnique Fédérale de Lausanne – EPFL

exp. 2014	Doctor of Philosophy	in Mechanics
2010	Master of Science	in Civil Engineering
2008	Bachelor of Science	in Civil Engineering

Carnegie Mellon University – CMU

2007 – 2008	Student Exchange	in Civil and Environmental Engineering
-------------	------------------	--

Research Experience

Ecole Polytechnique Fédérale de Lausanne – EPFL

2010 – present	Doctoral Research Assistant with Prof. Jean-François Molinari Studied the dynamic propagation of slip fronts at frictional interfaces using numerical simulations and revealed the importance of meso- and macro-scale aspects for the global response of frictional systems. Demonstrated the applicability of fracture mechanics concepts to describe and understand frictional slip front propagation.
2009 – 2010	Master Student Researcher with Prof. Jean-François Molinari Analysis of numerical aspects of rate-and-state friction laws.
2008	Master Student Researcher with Prof. Alain Nussbaumer Experimental study of a welded assembly of a petrol reservoir under cyclic loading.

California Institute of Technology

10 – 11/2012	Visiting Student Researcher with Prof. Jean-Paul Ampuero Development of a Linear Elastic Fracture Mechanics (LEFM) approach to analyze the propagation of precursory slip at frictional interfaces.
--------------	---

Research Interests

Mechanics of Materials:

- mechanics of dynamic and transient phenomena such as the initiation of frictional sliding
- damage of materials through fracture
- complex systems characterized by heterogeneity and non-linear materials

Scientific Computing:

- modeling the mechanics of materials using high-performance computing (HPC)
- developing modeling techniques needed for accurate numerical results
- developing open-source code for numerical modeling

Publications

Work in preparation for submission:

- 8 Pino Muñoz, D., Kammer, D.S., Radiguet, M., and Molinari, J.F., “Near-tip strain field similarity of simulated slip fronts and linear elastic fracture mechanics”, 2014.
- 7 Kammer, D.S., Pino Muñoz, D., and Molinari, J.F., “Length scale interaction of slip fronts and interface heterogeneity”, 2014.

Work submitted for publication:

- 6 Kammer, D.S., Radiguet, M., Ampuero, J.P., and Molinari, J.F., “Linear elastic fracture mechanics predicts slip precursor length”, *Tribology Letters*, 2014.

Refereed Journals:

- 5 Barras, F., Kammer, D.S., Geubelle, Ph.H., and Molinari, J.F., “A study of frictional contact in dynamic fracture along bimaterial interfaces”, *International Journal of Fracture*, published online, DOI:10.1007/s10704-014-9967-z, 2014.
- 4 Radiguet, M., Kammer, D.S., and Molinari, J.F., “The role of viscoelasticity on heterogeneous stress fields at frictional interfaces”, *Mechanics of Materials*, in press, 2014.
- 3 Kammer, D.S., Yastrebov, V.A., Anciaux, G., and Molinari, J.F., “The existence of a critical length scale in regularised friction”, *Journal of the Mechanics and Physics of Solids*, **63**, 40-50, 2014.
- 2 Radiguet, M., Kammer, D.S., Gillet, Ph., and Molinari, J.F., “Survival of heterogeneous stress distributions created by precursory slip at frictional interfaces”, *Physical Review Letters*, **111**, 164302, 2013.
- 1 Kammer, D.S., Yastrebov, V.A., Spijker, P., and Molinari, J.F., “On the propagation of slip fronts at frictional interfaces”, *Tribology Letters*, **48**, 27-32, 2012.

Professional Society Journals:

- 1 Chaubert, S., Kammer, D.S., Luyet, L.-B., and Thiébaud, R., “Perception du risque dans les tunnels routiers”, *Strasse und Verkehr - Route et trafic*, , 18-23, Dec 2009.

Presentations

Invited Seminars:

- 2014 | Laboratoire de Tribologie et Dynamique des Systèmes, École Centrale de Lyon, France.
- 2012 | Centre des Matériaux, Mines ParisTech, Paris, France.

Conferences & Workshops: (presenter underlined)

- 2014 | Kammer, D.S., Radiguët, M., Ampuero, J.P., and Molinari, J.F., “Predicting the length of slip precursors”, 11th World Congress on Computational Mechanics, 5th European Conference on Computational Mechanics, Barcelona, Spain, July 20-25, 2014.
- 2014 | Barras, F., Kammer, D.S., Geubelle, Ph.H., and Molinari, J.F., “A study of friction in dynamic fracture along bimaterial interfaces”, 11th World Congress on Computational Mechanics, 5th European Conference on Computational Mechanics, Barcelona, Spain, July 20-25, 2014.
- 2014 | Yastrebov, V.A., Kammer, D.S., Radiguët, M., and Molinari, J.F., “Dynamic fracture of adhesive vs frictional interfaces”, 20th European Conference on Fracture, Norway, June 30 – July 4, 2014.
- 2014 | Radiguët, M., Kammer, D.S., and Molinari, J.F., “Role of viscoelastic rheologies on heterogeneous stress fields in dynamic ruptures models”, EGU General Assembly, Vienna, Austria, April 27 – May 2, 2014.
- 2013 | Radiguët, M., Kammer, D.S., and Molinari, J.F., “Role of visco-elastic rheologies in the persistence of heterogeneous stress distributions in dynamic rupture models”, AGU fall meeting 2013, San Francisco, USA, December 9-13, 2013.
- 2013 | Radiguët, M., Kammer, D.S., and Molinari, J.F., “Evolution of heterogeneous stress distributions created by slip precursors in numerical simulations of frictional interfaces” (Poster), 40th Workshop of the International School of Geophysics, Erice, Sicily, Italy, May 18-24, 2013.
- 2012 | Radiguët, M., Kammer, D.S., and Molinari, J.F., “Dynamics of slip fronts at frictional interfaces: Analysis of slip precursors” (Poster), AGU fall meeting 2012, San Francisco, USA, December 3-7, 2012.
- 2012 | Radiguët, M., Kammer, D.S., Yastrebov, V.A., and Molinari, J.F., “Dynamics of slip fronts at frictional interfaces: analysis of slip precursors and rupture velocity” (Poster), ECGS Workshop 2012: Earthquake Source Physics on Various Scales, Luxembourg, October 3-5, 2012.
- 2012 | Kammer, D.S., Yastrebov, V.A., Anciaux, G., and Molinari, J.F., “Slip dynamics at frictional interfaces: Influence of viscoelasticity and energetic analysis”, 8th European Solid Mechanics Conference, Graz, Austria, July 9-13, 2012.
- 2012 | Kammer, D.S., Yastrebov, V.A., and Molinari, J.F., “Simulation et analyse de la dynamique de glissement entre deux corps viscoélastiques en contact”, 24ème Journées Internationales Francophones de Tribologie, Aix en Provence, France, May 9-11, 2012.
- 2012 | Kammer, D.S., Yastrebov, V.A., and Molinari, J.F., “Interfaces: How the rupture speed of slip fronts is related to the deformation energy” (Poster), Materials Deformation: Fluctuations, Scaling, Predictability, Les Houches, France, January 22-27, 2012.
- 2011 | Kammer, D.S., Yastrebov, V.A., Spijker, P., and Molinari, J.F., “On the initiation of dynamic sliding”, 2nd International Conference on Computational Contact Mechanics, Hannover, Germany, June 15-17, 2011.

Honors & Popular Media

- 2012 | Featured news article on EPFL’s front webpage (including a video): [“Earthquakes – the science of the stick-slip”](#)

2008	Carnegie Institute of Technology Dean's List
2007	Carnegie Institute of Technology Dean's List

Project Supervision

Master Theses (co-supervised with Prof. Jean-François Molinari):

2012 – 2013	Fabian Barras, Civil Engineering, EPFL (in collaboration with Prof. Philippe Geubelle from UIUC)
Spring 2013	Dana Christen, Computational Science and Engineering, EPFL

Semester Projects (co-supervised with Prof. Jean-François Molinari):

Spring 2014	Jérôme Brouchoud, Materials Science and Engineering, EPFL
Fall 2011	Alexandre Pachoud, Civil Engineering, EPFL (in collaboration with Dr. Thomas Menouillard from Stucky Ltd)
Fall 2011	Eloïse Marteau, Civil Engineering, EPFL (in collaboration with Dr. Thomas Menouillard from Stucky Ltd)
Spring 2010	Alodie Schneuwly, Civil Engineering, EPFL
Spring 2010	Alessandro D'amario, Civil Engineering, EPFL

Teaching Experience

Ecole Polytechnique Fédérale de Lausanne – EPFL

Fall 2013	Introduction to continuum mechanics (Undergraduate) – Teaching Assistant <i>TA sessions of 2h for 14 weeks: ~40 students</i>
Fall 2012	Selected topics in mechanics of solids and structures: Wave propagation and fracture mechanics (Master) – Teaching Assistant <i>TA sessions of 1h for 14 weeks: ~20 students</i>
Fall 2012	Introduction to continuum mechanics (Undergraduate) – Teaching Assistant <i>TA sessions of 2h for 14 weeks: ~30 students</i>
Spring 2011	Introduction to continuum mechanics (Undergraduate) – Teaching Assistant <i>TA sessions of 2h for 14 weeks: ~25 students</i>
Fall 2010	Selected topics in mechanics of solids and structures: Wave propagation and fracture mechanics (Master) – Teaching Assistant <i>TA sessions of 1h for 14 weeks: ~20 students</i>
Spring 2010	Introduction to continuum mechanics (Undergraduate) – Teaching Assistant <i>TA sessions of 2h for 14 weeks: ~20 students</i>

Didac High School Montreux

04 – 05/2009	Mathematics and Geometry – Lecturer <i>10h for 4 weeks: 3 × 20 students</i>
--------------	--

University Service

2011 – 2014	PhD student representative, Doctoral School Commission (EDOC), EPFL <i>Represented interests of the PhD students during the meetings of the Dean of the Doctoral School and the Directors of all Doctoral Programs (1 meeting per month)</i>
2012	PhD student representative, Internal Juridical Commission, EPFL <i>Participated in evaluating the severity of a PhD student's misdemeanor and in proposing possible sanctions (meetings when needed)</i>
2012	Member, EDOC Working Group on Plagiarism, Doctoral School, EPFL
2010 – 2012	Safety Delegate, Computational Solid Mechanics Laboratory, EPFL